Magnetic Force Microscopy with a Nanowire Cantilever:

From Theory to Application

Inauguraldissertation
zur
Erlangung der Würde eines Doktors der Philosophie
vorgelegt der
Philosophisch-Naturwissenschaftlichen Fakultät
der Universität Basel

von

Lukas Schneider

2026

Genehmigt von der Philosophisch-Naturwissenschaftlichen Fakultät
auf Antrag von

Erstbetreuer: Prof. Dr. Martino Poggio
Zweitbetreuer: Prof. Dr. Ernst Meyer
Externer Experte: Prof. Dr. Arnaud Gloppe

Basel, den 14. September 2025

Prof. Dr. Heiko Schuldt
Dekan

Abstract

Magnetic Force Microscopy with a Nanowire Cantilever (NW-MFM) establishes nanowires with magnetic tips as scanning force probes to enhance the sensitivity of conventional MFM. With exceptional force sensitivities on the order of only a few aNHz$^{-1/2}$, NW-MFM enables the detection of weak magnetic contrast with a spatial resolution below 100 nm. NW-MFM works in large applied fields of several tesla and from cryogenic to room temperature. This allows to probe surface magnetism in a wide parameter range. Similar to conventional MFM, frequency shifts and oscillation amplitudes are detected in NW-MFM. Focusing solely on magnetic interactions, the former corresponds to static stray field distributions, the later to energy dissipation.

NW-MFM and conventional MFM work similarly: the main difference is their operational geometry. MFM cantilevers oscillate vertically to a substrate probing out-of-plane stray field derivatives. In contrast, nanowires oscillate in a plane above the substrate and are thus sensitive to in-plane stray field derivatives. We show that the retrieved signal from NW-MFM can be converted to conventional MFM contrast allowing a straightforward interpretation and comparison between the two techniques.

NW-MFM and MFM rely on magnetic tips for imaging. The nanowires discussed in this manuscript carry elongated hard-magnetic tips to convert magnetic stray distributions into detectable force gradients. Due to the magnetic tips, NW-MFM is inherently an invasive magnetic imaging technique. Magnetic surface textures of samples can be altered or perturbed by the tip's stray field. We frame this invasiveness via a dynamic magnetic spring constant whose real and imaginary parts link the sample's magnetic susceptibility to the frequency shifts and oscillation amplitudes of the nanowire modes.

To establish NW-MFM in research, we apply NW-MFM to a variety of magnetic systems. In the helimagnet $Cu_2O_2SeO_3$ we resolve helical modulations and a distinct surface state. In the van der Waals magnets $Cr_2Ge_2Te_6$ and $EuGe_2$ we exploit the perturbative invasiveness of NW-MFM near the transition temperatures of the two materials. These examples highlight the particular strength of NW-MFM for weakly magnetic materials and demonstrate its potential as a powerful and versatile technique for nanoscale studies of both static and dynamic magnetism.

Acknowledgements

I am deeply grateful to Martino Poggio and Hinrich Mattiat for their invaluable guidance and support throughout this work. Martino, your lecture on nanomechanics at the beginning of my Master's studies was when this field first resonated with me. I am profoundly thankful for your mentorship, your calm and steady approach, and your constant availability to provide expert advice. Hinrich, you introduced me so wonderfully to the system during my Master's and supported me through many challenges along the way. Your calm and composed presence was always a great source of reassurance, especially when we were dealing with issues like temperature noise or unreliable actuation. I also deeply cherish our coffee breaks across the street, which made even the difficult moments feel lighter. I also thank Estefani Marchiori for her collaboration on the same samples, as well as for our many helpful discussions and moments of laughter. Further, my gratitude extends to Raffi Budakian and Marcus Wyss. Raffi, I am thankful to you and your students for providing the silicon nanowires that were central to this work and broadened the scope of this manuscript. Marcus, I greatly appreciated your expert assistance with the Helios FIB at the Nano Imaging Lab of the Swiss Nanoscience Institute. Your skill made the cobalt deposition on the nanowires certainly more efficient and definitely very enjoyable.

I acknowledge the University of Basel with the Department of Physics for their excellent mechanical workshop, where most components of the scanning probe system were manufactured, and I am very grateful to Dominik Sifrig for the supply of liquid helium that enabled my experiments. For the financial support, I am sincerely grateful to the Swiss Nanoscience Institute, whose continued backing made possible by the contributions of taxpayers, was essential to carrying out this research. For the editorial support, I also acknowledge the use of ChatGPT, which was used to polish my language and formate the equations presented in this manuscript.

Personally, I thank my partner Anouk and my parents, Sandra and René for always being there for me. Anouk, ich dank dir vo ganzem Härze für dini Unterstützig während mim Doktorat: S Guet-Zuerede, s wiederholte Dureläse vo dem Manuskript, s Hälfe bi Transfers, s Ans-Physik-Fahre am zwei am Morge an Neujohr, wel öbbis mit mim Experiment nit stimmt. Egal was, uf dich isch Verlass, und wenn ich gstress oder nervös bin, kanni bi dir Glasse-, Geborgeheit und Zueversicht finde. Mami und Papi, au euch dank ich vo ganzem Härze. Ihr händ mich bi mim ganze Bildigswäg immer tatkräftig und finanziell unterstützt, mich nie unter Druck gsetzt und nie zu öbbis drängt. Ihr händ für mich gsorgt im schöne Chästeli, woni mit euch und em Stefan immer sehr gärn mini Zit verbring.

Contents

List of Figures

Introduction

Magnetic materials are studied as tiny crystals, atomically thin flakes, or patterned nanostructures. Fabrication encourages this scale, and consumer expectations for compact, low-power devices demand it. At this small scale, a material's surface can govern its magnetic behavior. With surface parameters often differing from those of the bulk, it is useful to treat the surface as a distinct material. In practice, even bulk samples comprise two coupled regions: a volumetric interior and a surface or interface layer. Interfacial interactions shape the energy landscape even when the interior volume remains substantial. In many applications, surfaces and interfaces serve as the functional input-output channels (e.g. magnetic memory is written and read at interfaces), making surface-sensitive characterization essential. Equally, from a curiosity-driven perspective, their reduced dimensionality and broken symmetries render them intrinsically interesting systems.

Key techniques for probing magnetic surfaces include magnetic force microscopy (MFM), scanning nitrogen-vacancy (NV) center magnetometry, scanning superconducting quantum interference devices (SQUIDs), magneto-optical Kerr effect (MOKE) microscopy, and Lorentz transmission electron microscopy (LTEM), each trading off resolution, sensitivity, invasiveness, and device compatibility. A comparison of the first three techniques can be found in Ref. [1]. Conventional MFM detects a magnetic signal with a magnetized tip. The resulting image contrast is a convolution of the sample's stray field with the tip's magnetization distribution. Depending on the tip model (monopole-like vs. dipole-like) and detection scheme, the leading sensitivity may be to the field itself or to its first or second spatial derivatives. Accordingly, sensitivities are most rigorously quoted as minimum detectable force or force gradient, and only then converted to magnetic field or current using a calibrated tip model. Spatial resolution is typically tens of nanometres but can approach 10 nm with optimized tips [2]. As an order-of-magnitude reference, in resonant amplitude operation conventional cantilever MFM achieves current sensitivities of a few hundred $\mathrm{nAHz}^{-1/2}$ at lift heights of 50 to 100 nm [1]. Equivalently (via a Biot-Savart conversion for a straight current-carrying wire), this corresponds to hundreds of $\mathrm{nTHz}^{-1/2}$. Owing to the magnetic tip, care is required to minimize tip-induced effects on the magnetic texture. Magnetic tips should be carefully selected to balance signal and perturbation. Hard-magnetic tips are standard for robust contrast. Soft tips, whose magnetization can be perturbed by the sample field, have been deliberately exploited for write-head characterization [3, 4]. NV magnetometry provides quantitative magnetic-field maps from ambient to cryogenic temperatures. Spatial resolution is set primarily by the NV-sample spacing. Sensitivities below 60 $\mathrm{nTHz}^{-1/2}$ have been

reported together with 25 nm stand-off [5], albeit with potentially long acquisition times. Scanning SQUID microscopy measures magnetic flux and offers exceptional stray field sensitivity, down to 5 $\mathrm{nTHz}^{-1/2}$ with 160 nm loop diameters [6]. This corresponds to current sensitivities of a few $\mathrm{nAHz}^{-1/2}$ at 100 nm stand-off. SQUIDs require operation below the superconducting transition; operation in higher magnetic fields is challenging but feasible [7]. SQUID microscopy is inherently quantitative once the pickup-loop geometry is known. MOKE microscopy is fast, non-contact, and scalable in field of view. It probes the top few nanometres and is well suited to dynamics and hysteresis mapping, provided there is optical access and sufficient reflectivity. Buried or opaque caps reduce contrast. Spatial resolution is diffraction-limited unless near-field variants are used [8, 9, 10]. LTEM images magnetic textures via the Lorentz force with sub-10-nm resolution [11], but samples must be electron-transparent and TEM-compatible.

We entirely focus on MFM as it allows a wide measurement parameter range, it is operable in large fields and at temperatures from cryogenic to room temperature. Instead of conventional micro-cantilevers, we employ a nanowire as the mechanical transducer. This defines MFM with a nanowire (NW-MFM). Owing to their low mass, nanowires are sensitive to smaller forces than common cantilevers [12, 13, 14], providing NW-MFM the potential to be far more sensitive to magnetic force derivatives. Because a nanowire is laterally very compliant, the probe must be oriented nearly normal to the sample surface so that its compliant axes lie in plane. A horizontal orientation would align a compliant mode with the surface normal and cause the magnetic tip to snap into contact owing to the nanowire's low stiffness. This *pendulum* configuration is also used for highly compliant micro-cantilevers [15, 16]. Nanowires sense forces in the plane spanned by their oscillation. We describe their dynamics using a two degree of freedom structural dynamics model grounded in Euler-Bernoulli beam theory [17], with the formulation for nanowire probes developed by L. Mercier de Lépinay et al. and N. Rossi et al. [18, 12, 19]. For completeness, we re-derive their formalism. We then specialize this general force-sensing framework to magnetic forces, following and building on the derivations of H. Mattiat [20].

As a first experiment, NW-MFM has been demonstrated on permalloy discs, and its sensitivity was determined using a current-carrying wire as a field standard, yielding 5 $\mathrm{nTHz}^{-1/2}$ with cobalt (Co) nanowires (approximately 110 nm diameter, 10 μm length) [21]. We present measurements using silicon (Si) nanowires with Co-functionalized tips, investigating the helimagnetic skyrmion host Cu_2OSeO_3. We also discuss current caveats of NW-MFM and address tip-induced perturbations, which we exploit to obtain susceptibility-related imaging contrast of the two dimensional magnets, $Cr_2Ge_2Te_6$ and $EuGe_2$.

Mechanics and Magnetism

NW-MFM combines the magnetic interactions at a sample surface with the mechanical response of a nanowire probe. To interpret the signals detected in this method, it is necessary to lay out the theory that connects the relevant magnetic quantities, the mechanical behavior of the nanowire, and the way the two interact.

The first chapters of this manuscript review magnetic quantities such as magnetization, susceptibility, and stray fields, which determine how magnetic textures generate forces detectable by a nanowire tip. We then turn to the mechanical description of the nanowire, beginning with the damped harmonic oscillator and extending to Euler-Bernoulli beam theory with viscoelastic damping, which captures the dynamics and sensitivity of nanowire resonators. Building on these foundations, we describe nanowire force sensing in terms of projected susceptibilities and thermal noise, and finally connect these concepts to magnetic imaging. Together, these chapters provide the theory needed to analyze NW-MFM measurements and to relate observed frequency shifts and dissipation signals to the underlying magnetic properties of any sample.

1. Magnetic Quantities

NW-MFM ultimately senses force gradients that act between the magnetic stray field of a sample and the nanowire tip. To interpret these signals, it is important to recall the basic quantities of magnetism: magnetization, susceptibility, and the fields they produce. In this chapter we introduce these concepts starting from Maxwell's equations, describe how magnetic moments respond to external fields, and discuss how magnetization distributions give rise to the stray field above a surface. Particular attention is given to the magnetic susceptibility, which depends on temperature and determines how the sample itself can respond to the magnetic tip and thereby modify the measured signal. A further central tool is the formulation of the scalar magnetic potential in lateral Fourier space (**k**-space), which provides a convenient and widely used way to compute the stray field in MFM. These considerations form the magnetic side of the theory that underlies NW-MFM imaging.

1.1 Magnetic Field *Sources*

Magnetic fields in materials originate from the magnetic moments of localized (bound) charges, such as electrons in atoms. These include contributions from both orbital motion and intrinsic spin, and are modeled macroscopically by the magnetization field $\mathbf{M}$. The spatial variation of $\mathbf{M}$ gives rise to bound currents within the material. A further contribution to bound current arises from time-dependent polarization, described by the polarization field $\mathbf{P}$, whose time derivative can be interpreted as a polarization current density. Magnetic fields can also be generated by externally controllable sources, including free currents associated with current density $\mathbf{J}_{\text{free}}$, arising from the motion of unbound charges, and the vacuum displacement current density associated with time-varying electric fields $\mathbf{E}(t)$ (time denoted by t). All of these contributions appear in the macroscopic form of Ampère-Maxwell's law [22],

$$\nabla \times \mathbf{B} = \mu_0 \left(\mathbf{J}_{\text{free}} + \nabla \times \mathbf{M} + \frac{\partial \mathbf{P}}{\partial t} \right) + \mu_0 \epsilon_0 \frac{\partial \mathbf{E}}{\partial t}. \tag{1.1}$$

The terms $\mathbf{J}_{\text{free}}$ and $\partial \mathbf{E}/\partial t$ represent externally controllable sources such as conduction currents and applied electric fields that vary in time. In contrast, $\nabla \times \mathbf{M}$ and $\frac{\partial \mathbf{P}}{\partial t}$ correspond to bound currents associated with the internal response of the material.[1] To separate the magnetic contribution of the material, it is convenient to define the magnetic field strength

$$\mathbf{H} = \frac{1}{\mu_0}\mathbf{B} - \mathbf{M}. \tag{1.2}$$

This auxiliary field removes the explicit contribution of magnetization from the total magnetic field and is particularly useful in the static case, where $\partial \mathbf{E}/\partial t = \partial \mathbf{P}/\partial t = 0$. In magnetostatics, $\mathbf{H}$ provides a practical tool for describing magnetic phenomena in materials, especially when working with linear or piecewise uniform media.

1.2 Static Magnetic Susceptibility and the Curie-Weiss Model

To characterize the response of a material's magnetization to a static, magnetic field, we treat $\mathbf{M}$ as a function of $\mathbf{H}$. For small, reversible perturbations about a reference field $\mathbf{H}_0$, the response can be approximated by the first-order Taylor expansion

$$\mathbf{M}(H) \approx \mathbf{M}(H_0) + \chi_m(\mathbf{H}_0) \cdot (\mathbf{H} - \mathbf{H}_0), \quad \text{with} \quad \chi_m(\mathbf{H}_0) = \left. \frac{d\mathbf{M}}{d\mathbf{H}} \right|_{\mathbf{H}_0}. \tag{1.3}$$

The quantity $\chi_m(\mathbf{H}_0)$ is the (static) magnetic susceptibility evaluated at $\mathbf{H}_0$. When considering a paramagnet, which is what we do now, no spontaneous magnetization is present, so $\mathbf{M}(0) = 0$.

[1] Whether external or internal, currents and field variations ultimately originate from dynamic changes in electric potentials. In this sense, magnetic fields carry the imprint of a system's electrical history.

We therefore evaluate Eq. (1.3) at $\mathbf{H}_0 = 0$, so $\mathbf{M}(\mathbf{H}_0) = \mathbf{M}(0) = 0$. The zero field linear response is

$$\mathbf{M}(\mathbf{H}) \approx \chi_m(T) \cdot \mathbf{H}, \quad \chi_m(T) = \left.\frac{d\mathbf{M}}{d\mathbf{H}}\right|_{H\to 0}. \tag{1.4}$$

From a microscopic perspective with a field-dependent Hamiltonian $\mathcal{H}$, the magnetization is the thermal expectation value $M = -\langle \partial\mathcal{H}/\partial\mathbf{H}\rangle$ [22]. Hence both $\mathbf{M}$ and the (static) zero field susceptibility $\chi_m(T)$ inherit a temperature dependence from the thermal population of magnetic energy levels.

To describe the temperature dependence explicitly, we consider the response of an isotropic system of non-interacting localized magnetic moments to a uniform external magnetic field. We define $\mathbf{H} = H\hat{\mathbf{z}}$. In this case, the magnetization is obtained as the thermal average of the projection of the magnetic moment along the field direction. Following the standard derivation of the Curie law, we loosely adopt the treatment presented in *The Quantum Theory of Magnetism* by N. Majlis [23]. The resulting expression for the magnetization is

$$\mathbf{M}(H,T) = M\,\hat{\mathbf{z}} \quad \text{with} \quad M = ng\mu_B J B_J(\zeta), \tag{1.5}$$

with total angular momentum J, number of atoms per unit volume n, Landé g-factor g, and the Brillouin function

$$B_J(\zeta) = \frac{2J+1}{2J}\coth\left(\frac{(2J+1)\,\zeta}{2J}\right) - \frac{1}{2J}\coth\left(\frac{\zeta}{2J}\right), \tag{1.6}$$

which describes the thermal population of magnetic energy levels. Its argument, ζ, defined as $\zeta(H) = g\mu_B\beta JH$, denotes the ratio of the Zeeman energy $g\mu_B JH$ to the thermal energy $\beta^{-1} = k_BT$. In the weak-field limit, where the applied magnetic field $\mu_B H$ is much smaller than the thermal energy k_BT, $|\zeta| << 1$ [2], the Brillouin function can be approximated by its third-order expansion

$$B_J(\zeta) \approx \left.\frac{dB_J}{d\zeta}\right|_{\zeta=0}\zeta + \frac{1}{3!}\left.\frac{d^3B_J}{d\zeta^3}\right|_{\zeta=0}\zeta^3 = \frac{J+1}{3J}\,\zeta - \frac{(J+1)(2J^2+2J+1)}{15J^3}\,\zeta^3. \tag{1.7}$$

Substitution into Eq. (1.5) and differentiating with respect to H according to Eq. (1.3), we identify (considering a paramagnet has $M = 0$) the susceptibility

$$\chi_m(T) = \frac{C}{T} \quad \text{with} \quad C = \frac{n(g\mu_B)^2 J(J+1)}{3k_B}. \tag{1.8}$$

The inverse temperature dependence in Eq. (1.8) is referred to as the Curie law [22], where C denotes the Curie constant.

[2] Physically, this corresponds to a regime where the external field perturbs the system only slightly and does not significantly polarize the magnetic moments.

The Curie law describes the temperature- and field-dependent response of an isotropic system of non-interacting localized magnetic moments. In real materials, however, interactions between moments are often present. These interactions tend to align neighboring moments and can give rise to spontaneous magnetization, even in the absence of an external magnetic field. To capture this collective behavior, Weiss introduced the concept of an effective internal field that each moment experiences due to the average magnetization of its surroundings [23]. In a mean field approximation, this internal field is modeled as $\mathbf{H}_\mathrm{e} = \mathbf{H} + \lambda\mathbf{M}$, where λ is a constant representing the interaction strength. Shifting the argument of the Brillouin function from $\zeta(H)$ to $\zeta(H_\mathrm{e})$, the magnetization becomes

$$M = ng\mu_B J B_J\left(g\mu_B\beta J\left(H + \lambda M\right)\right). \tag{1.9}$$

Spontaneous order is characterized by $M \neq 0$ at $H = 0$. Accordingly, we set $H = 0$ in Eq. (1.9) and test for solutions. To simplify the notation, we define

$$\zeta_e = g\mu_B\beta J\lambda M, \quad \lambda_2(T) = \frac{ng^2\mu_B^2 J^2\lambda}{k_B T} \quad \text{and} \quad B_J'(0) = \left.\frac{dB_J}{d\zeta_e}\right|_{\zeta_e=0} \tag{1.10}$$

so Eq. (1.9) becomes

$$\zeta_e = \lambda_2 B_J\left(\zeta_e\right). \tag{1.11}$$

Graphically, solutions to Eq. (1.11) are the intersections of the functions $f_1(\zeta_e) = \zeta_e$ and $f_2(\zeta_e) = \lambda_2 B_J\left(\zeta_e\right)$, as illustrated in fig. 1.1. The number of intersections is set by the relative slopes of the two curves: with the fixed slope of f_1, $df_1/d\zeta_e = 1$, and since $dB_J/d\zeta_e \leq B_J'(0)$ for all ζ_e, the slope of f_2 is maximal at $\zeta_e = 0$. Hence intersections besides $\zeta_e = 0$ exist only if

$$1 < \lambda_2 B_J'(0). \tag{1.12}$$

With material parameters (n, g, J, λ) in Eq. (1.12) fixed, the only variable in Eq. (1.12) is the temperature T in $\lambda_2(T)$. Thus temperature alone sets the slope of f_2 and thereby controls the number of intersections (solutions). The critical temperature, known as the Curie temperature T_C, is the threshold between a single solution and multiple solutions. It is defined by

$$1 = \lambda_2(T_C)B_J'(0) = \frac{ng^2\mu_B^2 J^2\lambda}{k_B T_C}\frac{J+1}{3J} \quad \Rightarrow \quad T_C = \frac{ng^2\mu_B^2\lambda}{3k_B}J(J+1). \tag{1.13}$$

Equivalently, for any T,

$$T_C = T\lambda_2(T)B_J'(0). \tag{1.14}$$

For $T > T_C$ the only intersection is $\zeta_e = 0$. For $T < T_C$ there are three solutions: $\zeta_e = 0$ and $\pm\zeta_e(T) \neq 0$, indicating spontaneous magnetization. Substituting the definitions from Eq. (1.10) into Eq. (1.11) and in particular evaluating λ_2 at T_C with Eq. (1.10), $\lambda_2(T_C)$, we find, under consideration of the expansion in Eq. (1.7), the spontaneous magnetization

$$M = \pm\, ng\mu_B J\frac{J+1}{3}\left(\frac{5}{2J^2+2J+1}\right)^{1/2}\left(\frac{T_C - T}{T_C}\right)^{1/2}. \tag{1.15}$$

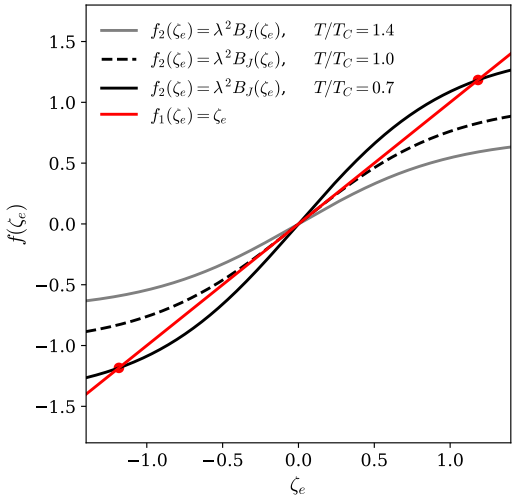

Fig. 1.1. Spontaneous magnetization below T_C ($T/T_C < 1$) in the Curie-Weiss model ($H = 0$) is revealed by the intersections of $f_1(\zeta_e) = \zeta_e$ and $f_2(\zeta_e) = \lambda_2 B_J(\zeta_e)$. We set $J = 1/2$, so $B_J(\zeta_e) = \tanh(\zeta_e)$.

The susceptibility above $T > T_C$ can also be retrieved from Eq. (1.9). According to Eqs. (1.4) and (1.3), we take the derivative of Eq. (1.9) to obtain

$$\frac{dM}{dH} = ng^2\mu_B^2 J^2 \beta \frac{dB_J}{d\zeta_e}(1 + \lambda \frac{dM}{dH}). \tag{1.16}$$

Evaluation at $H = 0$ and use of $M \to 0$ so $\zeta_e \to 0$ and $dB_J/d\zeta_e \to B_J'(0)$ with Eq. (1.14) yields

$$\chi_m = ng^2\mu_B^2 J^2 \beta \frac{T_C}{T\lambda_2(T)}(1 + \lambda\chi_m). \tag{1.17}$$

Rearrangement and simplification yields

$$\chi_m(T) = \frac{C}{T - T_C} \quad \text{with} \quad C = \frac{n(g\mu_B)^2 J(J+1)}{3k_B}. \tag{1.18}$$

In the Curie-Weiss model, the temperature dependences of the zero field magnetization and the zero field susceptibility together signal a continuous (second order) phase transition at T_C. From Eq. (1.15) $M(T)$ vanishes as T approaches T_C from below, while from Eq. (1.18) the susceptibility diverges as T approaches T_C from above. Thus, for $T > T_C$ the system is paramagnetic with $M = 0$. For $T < T_C$ it is ferromagnetic with $M = \pm M(T) \neq 0$. The zero field magnetization is therefore a natural order parameter: zero in the disordered phase, finite in the ordered phase.
The critical behavior in the Curie-Weiss model is characterized by the reduced temperature $T_r = (T - T_C)/T_C$: close to T_C, $M(T, H = 0) \propto |T_r|^{1/2}$ for $T_r \to 0^-$ and $\chi_m(T) \propto T_r^{-1}$ for $T_r \to 0+$. The associated mean field critical exponents are $\beta = 1/2$ for the magnetization and $\gamma = 1$ for the susceptibility. Because mean field theory neglects thermal fluctuations and spatial correlations, experimentally observed exponents differ and singularities are rounded in finite systems.

1.3 Dynamic Magnetic Susceptiblity and Relaxation

A magnet is a dynamic system. It is subject to thermal fluctuations and supports eigenmodes with characteristic resonance frequencies. In the Curie-Weiss treatment (c.f. Sec. 1.2) we neglected dynamics and obtained a static response function χ_m. When dynamical effects are included, the susceptibility becomes a time-dependent response function that relates the induced magnetization $\mathbf{M}(t)$ to a weak, time-dependent field $\mathbf{H}(t)$. Within linear-response theory, and assuming time-translation invariance and spatial homogeneity [22], it is convenient to Fourier transform the magnetization and field. In this representation the space-time convolution reduces to the simple product

$$\delta\mathbf{M}(\mathbf{k},\omega) = \boldsymbol{\chi}_m(\mathbf{k},\omega)\,\mathbf{H}(\mathbf{k},\omega). \tag{1.19}$$

$\boldsymbol{\chi}_m$ is a 3×3 complex susceptibility matrix with real and imaginary parts $\mathrm{Re}(\boldsymbol{\chi}_m)$ and $\mathrm{Im}(\boldsymbol{\chi}_m)$, respectively, while $\delta\mathbf{M}$ and $\mathbf{H}$ are vectors. The susceptibility depends on temperature, static bias field, anisotropy, and damping. We suppress these arguments in the notation. Consequently the response $\delta\mathbf{M}$ inherits this parameter dependence through $\boldsymbol{\chi}_m$. $\mathbf{H}$ is externally specified. When spatial homogeneity is broken, for instance in patterned films or near strong edges, the response becomes nonlocal and mixing of different wavevectors occurs.

In the dynamical regime, it is useful to distinguish between different physical channels of susceptibility. Depending on the orientation of the applied field, the system may respond through longitudinal fluctuations of the magnetization, transverse precession, or collective domain-wall motion. In the following we focus on these three cases. The order-parameter, or longitudinal, response describes the case where field and readout are collinear with the equilibrium magnetization. In this channel the dynamics are purely relaxational and the susceptibility follows a Debye form,

$$\chi_{m\parallel}(\omega) = \frac{\chi_{m\parallel}(0)}{1 - i\,\omega\,\tau}, \qquad \tau = \omega_c^{-1}, \tag{1.20}$$

with the relaxation time $\tau(T)$, characteristic frequency ω_c, and the static longitudinal susceptibility $\chi_{m\parallel}(0)$, which in mean field theory reduces to the Curie–Weiss form χ_m. From this simple form one immediately obtains the characteristic features of the longitudinal response. In the static limit ($\omega \to 0$, equivalently $\omega\tau \ll 1$), the real part reduces to the Curie-Weiss susceptibility and diverges at T_C, while the imaginary part vanishes. At finite frequency, however, $\mathrm{Im}(\boldsymbol{\chi}_m)$ develops a peak at the temperature T' where $\omega\tau(T') = 1$. Experiments by Dunlavy and Venus (ac-MOKE at 400 Hz on Fe/W(110)) revealed such a peak very near T_C [24], since the relaxation time must be large to satisfy $\omega\tau(T') = 1$. At higher probe frequencies, such as in MHz bulk measurements, the same condition shifts the peak to larger $|T - T_C|$, where the relaxation time is shorter. A second dynamical channel is the transverse precessional response, or ferromagnetic resonance. A drive field perpendicular to the equilibrium magnetization excites precession at the resonance frequency $\omega_0 = \gamma\mu_0 H_e$ typically in the GHz range. This precessional resonance does

not exhibit the critical divergence of the longitudinal susceptibility. It can soften when restoring fields vanish, and its linewidth often broadens near T_C. In multidomain states, modest fields act on domain walls, whose motion is governed by pinning and damping. The corresponding susceptibility spectra typically lie in the kHz range [25, 26], but they can extend into the MHz regime when pinning is weak or during depinning [27, 28]. Overdamped wall motion follows a Debye-like response, while inertia may give rise to weak resonances.

The relaxation times and characteristic frequency ranges of the magnetic response generally depend on the static bias field H, which sets the equilibrium state. To illustrate this dependence explicitly, we use a Landau free-energy description, which not only reproduces the Curie-Weiss susceptibility above T_C but also provides a framework for extending the discussion to dynamics [29],

$$F(M) = \frac{1}{2}\, a\, (T - T_C)\, M^2 + \frac{1}{4}\, b\, M^4 - H\, M, \tag{1.21}$$

where a and b are positive phenomenological constants that depend on microscopic details such as the exchange interaction [30, 29]. The equilibrium magnetization M_0 satisfies

$$\left.\frac{\partial F}{\partial M}\right|_{M_0} = 0 \quad \Rightarrow \quad a\, (T - T_C)\, M_0 + b\, M_0^3 = H. \tag{1.22}$$

The curvature at the equilibrium point,

$$\kappa = \left.\frac{\partial^2 F}{\partial M^2}\right|_{M_0} = a\, (T - T_C) + 3b\, M_0^2, \tag{1.23}$$

controls both statics and dynamics. Within relaxational time-dependent Ginzburg-Landau (TDGL) dynamics, a small deviation of the order parameter, $\delta M(t)$, relaxes back to equilibrium at a rate proportional to the curvature κ.[3] Consequently, the longitudinal response reduces to the Debye form from Eq. (1.20) with

$$\chi_{m\parallel}(0) = (\mu_0\, \kappa)^{-1}, \quad \text{and} \quad \tau \propto \kappa^{-1}. \tag{1.24}$$

The static bias H shifts the operating point to $M_0 \neq 0$. This increases the curvature κ through the $3bM_0^2$ term in Eq. (1.23). Consequently, the relaxation time shortens, the characteristic frequency ω_c rises.

[3] The relaxation is described by the linearized TDGL equation, $\tau_s \delta\dot{M} = -\kappa\, \delta M/\mu_0 + \delta H(t)$, given in eq. 36 of [31], with τ_s a microscopic time constant and δH a small external field perturbation.

1.4 Stray Field, Magnetic Potential and Charge Densities

If free, polarization, and vacuum displacement current densities cancel, i.e. $\mathbf{J}_{\text{free}} + \partial\mathbf{P}/\partial t + \epsilon_0\partial\mathbf{E}/\partial t = 0$, the Ampère-Maxwell's law of Eq. (1.1) simplifies. Together with the empirical absence of magnetic monopoles, the magnetic field satisfies

$$\nabla \times \mathbf{B} = \mu_0 \nabla \times \mathbf{M}, \tag{1.25}$$

$$\nabla \cdot \mathbf{B} = 0. \tag{1.26}$$

Eq. (1.2) leads to

$$\nabla \times \mathbf{H} = 0, \tag{1.27}$$

$$\nabla \cdot \mathbf{H} = -\nabla \cdot \mathbf{M}. \tag{1.28}$$

Because of Eq. (1.27), $\mathbf{H}$ is conservative and a scalar magnetic potential ϕ exists such that

$$\mathbf{H} = -\nabla\phi. \tag{1.29}$$

Substituting (1.29) into (1.28) yields the Poisson equation

$$\nabla^2\phi = \nabla \cdot \mathbf{M}. \tag{1.30}$$

The Poisson equation governs the potential inside magnetic materials, where $\nabla\cdot\mathbf{M} \neq 0$. It shows that the divergence of the magnetization acts as an effective source term, analogous to the role of electric charge in electrostatics.

The scalar potential ϕ encodes the field generated by a given magnetization. Solving Eq. (1.30) for ϕ provides a convenient route to compute the stray field via Eq. (1.29) in regions where $\mathbf{M} = 0$. To evaluate ϕ for a given magnetized body and thereby obtain $\mathbf{H}(\mathbf{R})$, we integrate the source term $\nabla \cdot \mathbf{M}(\mathbf{R}')$ over the magnetic volume V. The vector $\mathbf{R}$ denotes an observation point of the field, and $\mathbf{R}'$ denotes a source point inside the magnetized body. Assuming $\mathbf{M}$ is smooth inside the material, it may be discontinuous only at the surface[4], we apply the divergence theorem to a vanishingly thin shell ΔV enclosing the surface boundary. This yields

$$\begin{aligned}
\int_V \nabla \cdot \mathbf{M}\, d^3\mathbf{R}' &= \int_{V-\Delta V\to V} \nabla \cdot \mathbf{M}\, d^3\mathbf{R}' + \int_{\Delta V\to 0} \nabla \cdot \mathbf{M}\, d^3\mathbf{R}' \\
&= \int_V \nabla \cdot \mathbf{M}\, d^3\mathbf{R}' + \oint_S \mathbf{M} \cdot d\mathbf{S}' \\
&= -\int_V \rho_m\, d^3\mathbf{R}' + \oint_S \sigma_m\, dS'.
\end{aligned} \tag{1.31}$$

[4]Discontinuities in $\mathbf{M}$ may also occur at internal interfaces (e.g. domain walls). These can be accounted for by including additional surface integrals over the corresponding internal boundaries.

Eq. (1.31) defines volume and surface magnetic charge densities

$$\rho_m = -\nabla \cdot \mathbf{M} \quad \text{and} \quad \sigma_m = \hat{\mathbf{n}} \cdot \mathbf{M}, \tag{1.32}$$

where $\hat{\mathbf{n}}$ is the outward normal surface vector of the magnetized body. In terms of these densities, the scalar potential can be written as

$$\phi(\mathbf{R}) = \frac{1}{4\pi} \left(\int_V \frac{\rho_m(\mathbf{R}')}{|\mathbf{R} - \mathbf{R}'|} \, d^3\mathbf{R}' + \oint_S \frac{\sigma_m(\mathbf{R}')}{|\mathbf{R} - \mathbf{R}'|} \, dS' \right). \tag{1.33}$$

Taking the gradient of Eq. (1.33) according to Eq. (1.29) yields the field in terms of ρ_m and σ_m.

$$\mathbf{H}(\mathbf{R}) = \frac{1}{4\pi} \left(\int_V \rho_m(\mathbf{R}') \frac{\mathbf{R} - \mathbf{R}'}{|\mathbf{R} - \mathbf{R}'|} \, d^3\mathbf{R}' + \oint_S \sigma_m(\mathbf{R}') \frac{\mathbf{R} - \mathbf{R}'}{|\mathbf{R} - \mathbf{R}'|} \, dS' \right). \tag{1.34}$$

This formulation makes the analogy to electrostatics explicit and provides a direct route to compute the stray field from a given magnetization distribution.

1.5 Stray Field above a Magnetic Surface

In MFM, we probe the lateral (x, y) variation of the stray field at constant height $z > 0$ above the surface of a magnetized body. To formulate the stray field $\mathbf{H}$ in this region, we solve Poisson's equation (1.30) for the potential ϕ, from which $\mathbf{H}$ is recovered via Eq. (1.29). This approach is convenient, because in the (free space) region above the sample, the magnetization vanishes, $\mathbf{M} = 0$. Thus Poisson's equation simplifies to $\nabla^2\phi = 0$. We solve for $\phi(\mathbf{r}, z)$ by applying a two-dimensional (2D) Fourier transform in the lateral coordinates $\mathbf{r} = (x, y)$, moving into the corresponding $\mathbf{k}$-space, where $\mathbf{k} = (k_x, k_y)$. The transform is

$$\phi(\mathbf{k}, z) = \int \phi(\mathbf{r}, z) \, e^{-i\mathbf{k}\cdot\mathbf{r}} \, d^2\mathbf{r}, \quad \text{where } d^2\mathbf{r} = dx\, dy, \quad \mathbf{k} = (k_x \, , \, k_y). \tag{1.35}$$

To move the simplified Poisson equation to $\mathbf{k}$-space, we integrate by parts, assuming vanishing boundary terms at infinity:

$$\int \nabla^2\phi e^{-i\mathbf{k}\cdot\mathbf{r}} d^2\mathbf{r} = \left(-k^2 + \frac{\partial^2}{\partial z^2} \right) \phi(\mathbf{k}) = 0. \tag{1.36}$$

This is an ordinary differential equation in z. Assuming that $\phi \to 0$ as $z \to \infty$, the physical solution is

$$\phi(\mathbf{k}, z + z') = \phi(\mathbf{k}, z) e^{-kz'}, \quad k = |\mathbf{k}|. \tag{1.37}$$

This form reflects vertical propagation. If ϕ is known at some base height z, it decays exponentially for displacements z' above. To compute the magnetic field from this potential, we apply a gradient operator in $\mathbf{k}$-space. Since the transform was applied in x and y, we obtain the 2D gradient $\nabla_k = (ik_x, ik_y)$. The magnetic field in $\mathbf{k}$-space is then [32]

$$\mathbf{H}(\mathbf{k}, z + z') = -(ik_x, ik_y, \frac{\partial}{\partial z})\phi(\mathbf{k}, z) e^{-kz'} = \mathbf{H}(\mathbf{k}, z) e^{-kz'}, \tag{1.38}$$

where $\mathbf{H}(\mathbf{k}, z) = -(ik_x, ik_y, -k)\phi(\mathbf{k}, z)$ such that we can define the three-dimensional gradient in $\mathbf{k}$-space:

$$\nabla_{(\mathbf{k},k)} = (ik_x, ik_y, \frac{\partial}{\partial z}) = (ik_x, ik_y, -k). \tag{1.39}$$

Using this definition of the gradient and Eq. (1.28) which simplifies to $\nabla \cdot \mathbf{H} = 0$ above the surface, we obtain through $\nabla_{(\mathbf{k},k)} \cdot \mathbf{H}(\mathbf{k}) = 0$, the constraint [33]

$$k\mathbf{H}_z(\mathbf{k}) = ik_x\mathbf{H}_x(\mathbf{k}) + ik_y\mathbf{H}_y(\mathbf{k}). \tag{1.40}$$

In the interpretation of MFM signals, Eq. (1.40) is important as it links the out-of-plane field component to the in-plane field structure in $\mathbf{k}$-space.

1.6 Magnetic Potential of a Uniformly Magnetized Cylinder

Our MFM tip is elongated and axially magnetized. To estimate its invasiveness, we derive the scalar potential it produces at the sample surface, which directly sets the stray field (local bias) applied by the tip. For the calculation, we consider a uniformly magnetized cylinder of magnetic material oriented along $\hat{\mathbf{z}}$ with length L, radius R, and magnetization pointing in $\mathbf{z}$, i.e. $\mathbf{M} = -M_z\hat{\mathbf{z}}$. The bottom base of the cylinder is located at $z = a > 0$ and the top base at $z = a + L$. We identify magnetic surface charge densities $\sigma_{z=a} = M_z$, and $\sigma_{a+L} = -M_z$. We aim to find the potentials at $z = 0$ and $z = a$ in $\mathbf{k}$-space. The magnetic potential at $z = a$ is

$$\begin{aligned}
\phi(\mathbf{k}, a) &= \int \phi(\mathbf{r}, a)e^{-i\mathbf{k}\cdot\mathbf{r}}d^2r \\
&= \frac{1}{4\pi}\int_S \sigma_a \int \frac{e^{-i\mathbf{k}\cdot\mathbf{r}}}{|\mathbf{r}-\mathbf{r}'|}d^2\mathbf{r}dS' + \frac{1}{4\pi}\int_S \sigma_{a+L}\int \frac{e^{-i\mathbf{k}\cdot\mathbf{r}}}{\sqrt{|\mathbf{r}-\mathbf{r}'|^2+L^2}}d^2\mathbf{r}dS' \\
&= \frac{1}{4\pi}M_z\int_S e^{-i\mathbf{k}\cdot\mathbf{r}'}dS'\left(\int \frac{e^{-i\mathbf{k}\cdot\tilde{\mathbf{r}}}}{|\tilde{\mathbf{r}}|}d^2\tilde{\mathbf{r}} - \int \frac{e^{-i\mathbf{k}\cdot\tilde{\mathbf{r}}}}{\sqrt{|\tilde{\mathbf{r}}|^2+L^2}}d^2\tilde{\mathbf{r}}\right) \\
&= \frac{1}{4\pi}M_z\int_S e^{-i\mathbf{k}\cdot\mathbf{r}'}dS'\left(\frac{2\pi}{k} - \frac{2\pi}{k}e^{-kL}\right) \\
&= \frac{1}{2k}M_z\frac{2\pi R}{k}J_1(kR)(1-e^{-kL}).
\end{aligned} \tag{1.41}$$

J_1 denotes the first-order Bessel function of the first kind. With Eq. (1.37), we find the potential at $z = 0$:

$$\phi(\mathbf{k}, 0) = \frac{1}{2k}M_z\frac{2\pi R}{k}J_1(kR)(1-e^{-kL})e^{-ka}. \tag{1.42}$$

2. Damped Harmonic Oscillator Model

The nanowire in NW-MFM acts as a mechanical resonator that transduces forces into measurable displacements. The simplest model for such a resonator is the damped harmonic oscillator. In this chapter we review its equation of motion, define the mechanical susceptibility as a response function, and connect dissipation to the imaginary part of this susceptibility. This model introduces the concepts of resonance, damping, and thermal noise, which are central for quantifying the force sensitivity of a nanowire.

2.1 Equation of Motion and Mechanical Susceptibility

The damped harmonic oscillator is a theoretical concept that describes a system obeying the equation of motion

$$m\delta\ddot{x}(t) + \Gamma\delta\dot{x} + k\delta x(t) = \delta F(t). \tag{2.1}$$

Here, m is the mass of the oscillator, Γ is a damping constant, k is the spring constant, $\delta F(t)$ is a small excitation force acting on the oscillator, and $\delta x(t)$ denotes a small displacement of the oscillator from an equilibrium position. The steady state solution to the equation of motion is found by a transformation to frequency space, rearrangement and back-transformation. We remain in frequency space:

$$\delta x(\omega) = \chi(\omega) \cdot \delta F(\omega), \quad \text{with} \quad \chi(\omega) = [-m\omega^2 - i\omega\Gamma + k]^{-1} = [m\left(\omega_0^2 - \omega^2\right) - i\omega\Gamma]^{-1}. \tag{2.2}$$

The angular frequency ω is introduced by the Fourier transformation. The angular resonance frequency of the oscillator ω_0 is the eigenvalue of Eq. (2.1) for $\delta F = \Gamma = 0$ and is defined by the spring constant $k = m\omega_0^2$. The mechanical susceptibility χ is the response function that determines how well the system reacts to the force $\delta F(\omega)$. Note that while here χ, Γ and k (and later also the power spectral density S) are treated as scalars, we use † notation, denoting the conjugate transpose, where appropriate, so expressions remain valid if later promoted to matrices.

The mechanical susceptibility can be separated into real and imaginary parts

$$\mathrm{Re}(\chi(\omega)) = \frac{m(\omega_0^2 - \omega^2)}{m^2\left[(\omega_0^2 - \omega^2)^2 + \omega^2\Gamma^2\right]}, \tag{2.3}$$

$$\mathrm{Im}(\chi(\omega)) = \frac{\omega\,\Gamma}{m^2\left[(\omega_0^2 - \omega^2)^2 + \omega^2\Gamma^2\right]} \tag{2.4}$$

$$= \frac{\chi - \chi^\dagger}{2i} = \chi\,\frac{\chi^{-1} - (\chi^{-1})^\dagger}{2i}\,\chi^\dagger = \chi\,\mathrm{Im}(\chi^{-1})\,\chi^\dagger = \omega\,\chi\,\Gamma\,\chi^\dagger. \tag{2.5}$$

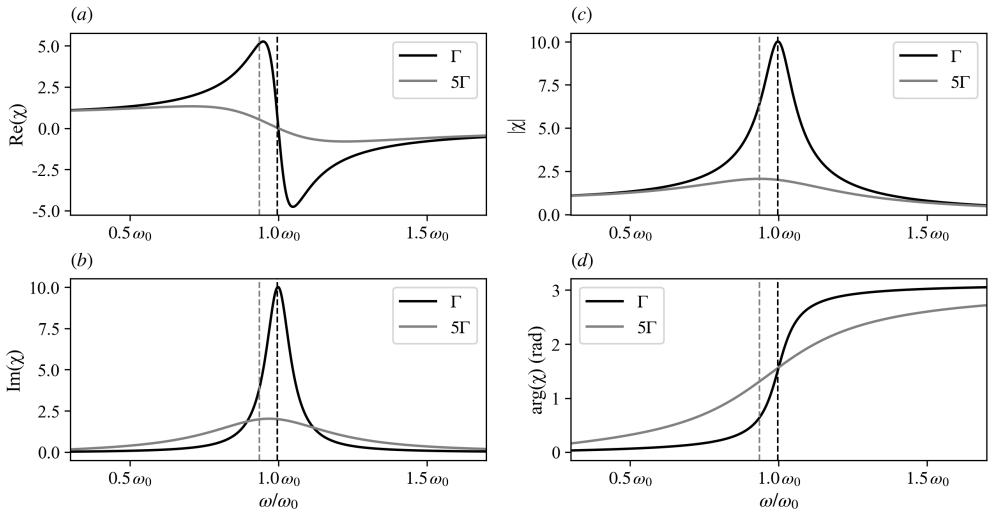

Fig. 2.1. Susceptibility curves for two damping constants Γ. (a) Real part of the complex susceptibilty χ, (b) imaginary part closely related to dissipation, (c) magnitude, and (d) phase. All broaden when Γ increases. An increase in Γ shifts the curves down in frequency.

The imaginary part is intricately connected to dissipation. This becomes evident when using the average complex power

$$P = \frac{1}{T}\int_0^T f(t)\dot{g}^*(t)dt. \tag{2.6}$$

P quantifies the energy exchanged per cycle between a harmonic excitation and the resonator. For a single frequency excitation force $\delta f(t) = \delta F(t) = F_0(\omega)e^{-i\omega t}$ the displacement is $g(t) = \delta x(t) = x_0(\omega)e^{-i\omega t}$ with the phasor relation $x_0(\omega) = \chi(\omega)F_0(\omega)$. Substituting into Eq. (2.6) yields

$$P = i\omega|F_0(\omega)|^2\chi^* = i\omega|F_0(\omega)|^2\big(\mathrm{Re}(\chi) - i\,\mathrm{Im}(\chi)\big). \tag{2.7}$$

The real and imaginary parts of P separate into dissipative and reactive contributions

$$P_{\mathrm{diss}} = \mathrm{Re}(P) = \omega|F_0(\omega)|^2\mathrm{Im}(\chi(\omega)), \tag{2.8}$$

$$P_{\mathrm{react}} = \mathrm{Im}(P) = \omega|F_0(\omega)|^2\mathrm{Re}(\chi(\omega)). \tag{2.9}$$

The dissipated power P_{diss} is directly related to the imaginary part of the susceptibility, while the real part governs stored elastic energy.

2.2 Power Spectral Densities and Force Sensitivity Limit

The imaginary part of the mechanical susceptibility plays a crucial role in quantifying the force sensitivity of the damped harmonic oscillator. It governs the response to external excitement and the magnitude of thermal fluctuations. In thermal equilibrium, the oscillator is continuously subject to random thermal forces $\delta F = F_{\mathrm{th}}(t)$ (Langevin force) originating from its coupling to a thermal bath. The fluctuation–dissipation theorem (FDT) provides the direct link between a system's response function and the statistical properties of its thermal fluctuations.
In the classical limit, where $k_B T \gg \hbar\omega$, the FTD from Eq. (A.31) applies. Specializing this result to the displacement observable δx, and using the explicit form of the susceptibility in Eq. (2.5) with the identities in Eq. (2.5), the FDT yields the displacement-noise power spectral density (PSD),

$$S_x(\omega) = \frac{2k_B T}{\omega}\mathrm{Im}(\chi) = 4k_B T \chi \Gamma \chi^\dagger. \tag{2.10}$$

Applying the same reasoning, but now considering the thermal driving force $F_{\mathrm{th}}(t)$ as the observable, requires rewriting the response relation. Rearranging $\delta x(\omega) = \chi \delta F(\omega) \Leftrightarrow \delta F(\omega) = \chi^{-1}\delta x(\omega)$[1] shows that the inverse susceptibility specifies the response of the force to displacement. Using this form in the FDT gives the thermal force-noise PSD

$$S_F(\omega) = \frac{4k_B T}{\omega}\mathrm{Im}(\chi^{-1}) = 4k_B T \Gamma. \tag{2.11}$$

Force- and displacement-noise PSDs are related through the susceptibility. By comparison of Eqs. (2.10) and (2.11)

$$S_x(\omega) = \chi S_F(\omega) \chi^\dagger. \tag{2.12}$$

Eq. (2.12) shows that a measured displacement spectrum S_x can be used to infer the corresponding thermal force spectrum S_F. In this work we adopt the per-Hz convention for PSDs (see appendix A.2), so that S_x carries units of m^2/Hz and S_F carries units of N^2/Hz. By definition, S_x and S_F specify the mean-square displacement and force fluctuations contained in an infinitesimal frequency interval around ν. To obtain the mean-square fluctuation within a finite frequency interval (bandwidth) $\Delta\nu_{\mathrm{BW}}$, one integrates the PSD over that interval. Taking the square root gives the smallest measurable root-mean-square (rms) fluctuations,

$$\delta x_{\mathrm{rms}}(\Delta\nu_{\mathrm{BW}}) = \sqrt{\langle |\delta x(\nu)|^2 \rangle} = \sqrt{\int_{\Delta\nu_{\mathrm{BW}}} S_x(\nu)\, d\nu}, \tag{2.13}$$

$$\delta F_{\mathrm{rms}}(\Delta\nu_{\mathrm{BW}}) = \sqrt{\langle |F_{\mathrm{th}}(\nu)|^2 \rangle} = \sqrt{\int_{\Delta\nu_{\mathrm{BW}}} S_F\, d\nu} = \sqrt{S_F\, \Delta\nu_{\mathrm{BW}}} = \sqrt{4k_B T \Gamma\, \Delta\nu_{\mathrm{BW}}}. \tag{2.14}$$

The second integral simplifies because S_F is frequency-independent. To formulate a bandwidth-independent oscillator-intrinsic force sensitivity limit, we normalize $\delta F_{\mathrm{rms}}(\Delta\nu_{\mathrm{BW}})$:

$$F_{\mathrm{min}} = \frac{\delta F_{\mathrm{rms}}(\Delta\nu_{\mathrm{BW}})}{\sqrt{\Delta\nu_{\mathrm{BW}}}} = \sqrt{S_F} = \sqrt{4\, k_B\, T\, \Gamma}. \tag{2.15}$$

[1] Assume $\det(\chi^{-1}) \neq 0$.

$F_{\min}$ carries units of $\mathrm{N\,Hz^{-1/2}}$ and denotes the force sensitivity, i.e. the thermal force noise floor of a mechanical resonator. It improves when the temperature T and the damping constant Γ decrease. For a structural beam such as a micro-cantilever or a nanowire, $\Gamma = m\omega_0/Q$ (a result we will explicitly obtain by the end of the next chapter). This relation shows that Γ decreases if the mass m or the resonance frequency ω_0 are reduced, or if the quality factor Q is increased. We motivate the use of nanowires over conventional cantilevers for MFM by targeting the mass: the cross section of nanowires is orders of magnitude smaller than that of cantilevers. Although Q can degrade when structures are made very thin, the reduction in mass and resonance frequency typically outweighs this effect, resulting in an overall improvement in sensitivity. This scaling argument is not unique to nanowires; thinning down conventional cantilevers has been shown to substantially improve their force sensitivity [34]. Micro-cantilevers, when carefully optimized for high Q, can reach the few-attonewton regime, with $F_{\min} = 6\,\mathrm{aN\,Hz^{-1/2}}$ reported for single-crystal silicon devices [15]. Nanowires intrinsically push this limit further, since not only the thickness but also the width is reduced compared to conventional cantilevers. For example, Co nanowires reach $F_{\min} = 5\,\mathrm{aN\,Hz^{-1/2}}$ [21], while silicon carbide (SiC) nanowires benefit from both cryogenic operation and their exceptionally high intrinsic Q, achieving record values of $F_{\min} = 40\,\mathrm{zN\,Hz^{-1/2}}$ together with force gradient sensitivities in the $\mathrm{fN\,m^{-1}}$ range [14]. These results show that while thinning cantilevers and optimizing Q can push them into the few-attonewton regime, nanowires intrinsically operate there and, thanks to both geometry and material properties, can surpass this level by orders of magnitude, making their implementation in NW-MFM the natural path to push the sensitivity limits of the technique.

3. Viscoelastic Euler-Bernoulli Beam

While the harmonic oscillator captures the basic resonant behavior of the nanowire in NW-MFM, its parameters should not be introduced *ad hoc*. In this chapter we use a variational approach to obtain the dynamic Euler-Bernoulli beam equation together with the general boundary-condition equations. We then introduce viscoelastic damping, define an effective Young's modulus and the quality factor Q, and couple this damping model to the dynamic beam equation. From the resulting complex-stiffness formulation we derive the flexural eigenmodes and perform a modal reduction that yields, for each mode, the effective mass, stiffness, and damping (or Q). This construction shows in a controlled way how the damped harmonic oscillator description arises as the single-degree-of-freedom approximation of a beam, with parameters linked to material properties and geometry. The next chapter applies this modal picture to the NW in NW-MFM and treats its two flexural modes as a coupled, two-degree-of-freedom force sensor.

3.1 Viscoelastic Damping

Hooke's law, $\sigma = E\epsilon$, describes a linear and instantaneous relationship between stress $\sigma(t)$ and strain $\epsilon(t)$ with Young's modulus of elasticity E. However, real materials exhibit time-dependent behavior: stress relaxes, and strain develops over time. To capture this, Zener proposed [35]

$$\sigma + \tau_\sigma \dot{\sigma} = E_r \left(\epsilon + \tau_\epsilon \dot{\epsilon}\right), \tag{3.1}$$

which extends linear elasticity by introducing the stress relaxation time $\tau_\sigma > 0$, the strain retardation time $\tau_\epsilon > 0$, and the relaxed Young's modulus $E_r > 0$. The Fourier transform of Eq. (3.1) yields

$$\sigma(\omega) = E(\omega)\epsilon(\omega) \quad \text{with} \quad E(\omega) = E_r \left(\frac{1 - i\omega\tau_\epsilon}{1 - i\omega\tau_\sigma}\right). \tag{3.2}$$

Zener's model in frequency space reflects the linear but frequency-dependent nature of the model and applies to signals of arbitrary frequency content. By setting $\bar{\tau}^2 = \tau_\epsilon \tau_\sigma$ and $\bar{\tau}\Delta = \tau_\epsilon - \tau_\sigma$, we define an effective Young's modulus $E_\mathrm{e}(\omega)$[1], and the quality factor $Q > 0$ writing [35]

$$E_\mathrm{e}(\omega) = E_r \cdot \frac{1 + \omega^2\bar{\tau}^2}{1 + \omega^2\tau_\sigma^2} \quad , \quad \frac{1}{Q} = \frac{\omega\bar{\tau}\Delta}{1 + \omega^2\bar{\tau}^2}. \tag{3.3}$$

Using these definitions we separate the Young's modulus into real and imaginary parts as

$$\begin{aligned}
E(\omega) &= E_r \frac{1 - i\omega\,\tau_\epsilon}{1 - i\omega\,\tau_\sigma} \\
&= E_r \frac{(1 - i\omega\tau_\epsilon)(1 + i\omega\tau_\sigma)}{1 + \omega^2\tau_\sigma^2} \\
&= E_r \frac{1 + \omega^2\tau_\epsilon\tau_\sigma - i\omega(\tau_\epsilon - \tau_\sigma)}{1 + \omega^2\tau_\sigma^2} \\
&= E_r \frac{1 + \omega^2\bar{\tau}^2 - i\omega\,\bar{\tau}\,\Delta}{1 + \omega^2\tau_\sigma^2} \\
&= E_r \frac{1 + \omega^2\bar{\tau}^2}{1 + \omega^2\tau_\sigma^2} \;-\; i\,E_r \frac{\omega\,\bar{\tau}\,\Delta}{1 + \omega^2\tau_\sigma^2} \\
&= E_\mathrm{e}(\omega)\left(1 - \tfrac{i}{Q(\omega)}\right).
\end{aligned} \tag{3.4}$$

With real and imaginary parts explicitly given by

$$\mathrm{Re}(E(\omega)) = E_\mathrm{e}(\omega) \quad \text{and} \quad \mathrm{Im}(E(\omega)) = -\frac{E_\mathrm{e}(\omega)}{Q(\omega)} = -E_r \frac{\omega\bar{\tau}\Delta}{1 + \omega^2\tau_\sigma^2} \leq 0. \tag{3.5}$$

To interpret the real and imaginary parts of $E(\omega)$, we consider the complex power from Eq. (2.6) in a system of single frequency represented by $f(t) = \sigma(t) = \sigma_0(\omega)e^{-i\omega t}$, $g(t) = \epsilon(t) = \epsilon_0(\omega)e^{-i\omega t}$, with phasors $\sigma_0(\omega)$, $\epsilon_0(\omega)$, and with $\sigma_0(\omega) = E(\omega)\epsilon_0(\omega)$. Inserting in the definition of the average complex power gives

$$P = i\omega|\epsilon_0(\omega)|^2(\mathrm{Re}(E(\omega)) + i\mathrm{Im}(E(\omega))) = i\omega|\epsilon_0(\omega)|^2 E_\mathrm{e}(\omega)(1 - \frac{i}{Q(\omega)}). \tag{3.6}$$

[1] $E_\mathrm{r} > 0$ because $\tau_\sigma, \tau_\epsilon, E_r > 0$.

The dissipated power is given by the magnitude of the complex power's real part, $P_{\text{diss}} = |\text{Re}(P)|$, which corresponds to the imaginary part of the Young's modulus. The reactive power and stored elastic energy are given by the imaginary part of the complex power, $P_{\text{react}} = \text{Im}(P)$, related to the real part of the Young's modulus:

$$P_{\text{diss}} = -\omega|\epsilon_0(\omega)|^2\text{Im}(E(\omega)) = \omega|\epsilon_0(\omega)|^2 E_{\text{e}}(\omega)/Q \geq 0, \tag{3.7}$$

$$P_{\text{react}} = \omega|\epsilon_0(\omega)|^2\text{Re}(E(\omega)) = \omega|\epsilon_0(\omega)|^2 E_{\text{e}}(\omega). \tag{3.8}$$

The ratio of reactive and dissipative power reflects how efficiently a material stores energy relative to how much it dissipates.

$$\frac{P_{\text{react}}}{P_{\text{diss}}} = \frac{\text{Re}(E(\omega))}{-\text{Im}(E(\omega))} = Q(\omega) \geq 0 \tag{3.9}$$

We find the ratio to be equivalent to the defined Q. The quality factor Q denotes the ratio of energy stored in the resonator to the energy dissipated per cycle by damping processes.

3.2 Kinematics and Strain in the Euler-Bernoulli Beam

A straight beam of width b, height h, and length L, with $b < h \ll L$ is described in an orthonormal basis $\{\hat{\mathbf{x}}, \hat{\mathbf{y}}, \hat{\mathbf{z}}\}$ with $\hat{\mathbf{x}}$, $\hat{\mathbf{y}}$ spanning the transverse (cross sectional) plane, and $\hat{\mathbf{z}}$ along the beam's longitudinal axis. The undeformed beam extends in $\hat{\mathbf{x}}$ from $x = -b/2$ to $x = b/2$, in $\hat{\mathbf{y}}$ from $y = -h/2$ to $y = h/2$, and in $\hat{\mathbf{z}}$ from $z = -L/2$ to $z = L/2$.
A small distributed load $q(z,t)$ (SI: N/m) acts along the centroidal axis of the beam. It is applied along $\hat{\mathbf{x}}$, where bending (within the xz-plane) occurs most naturally because of $b < h$. The resulting small transverse deflection is denoted $a(z,t)\hat{\mathbf{x}}$. In Euler-Bernoulli beam theory, where

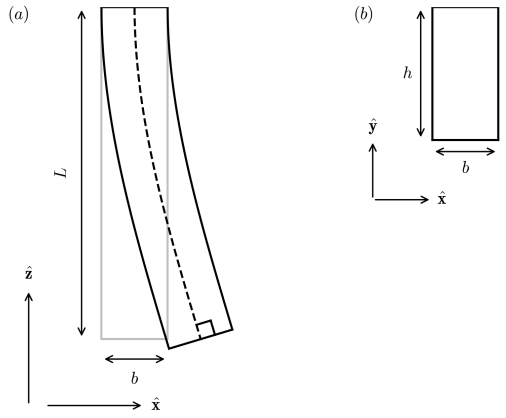

Fig. 3.1. Euler-Bernoulli beam. (a) Side view with undeflected (grey) and deflected beam (black). The width b of the bottom face is in both cases the same. The dashed line is the centroidal axis. All cross sectional slices stand orthogonal to the centroidal axis. (b) Cross sectional slice.

plane cross sections remain rigid, plane, and normal to the centroidal axis (no shear deformation), not only the segments of the centroidal axis but entire cross sectional slices translate along $\hat{\mathbf{x}}$ by $a(z,t)$, and rotate by $\Theta = da/dz$ about $\hat{\mathbf{y}}$. We now assume small slopes,

$$\left|\frac{da}{dz}\right| \ll 1, \tag{3.10}$$

so that $\cos(\Theta) \approx 1$ and $\sin(\Theta) \approx \Theta$. This is the standard small-deflection assumption of Euler-Bernoulli theory, ensuring geometric linearity. With a small angle of rotation Θ a sample point on a cross sectional slice of the beam (length dz) is displaced from an initial position $(x \;\; y \;\; z)$ to

$$\Big(x + a\cos\Theta \quad y \quad z - x\sin\Theta\Big) \approx \Big(x + a \quad y \quad z - x\Theta\Big) = \left(x + a \quad y \quad z - x\,\frac{da}{dz}\right). \tag{3.11}$$

The difference of the new position with respect to the initial one defines the displacement field

$$\mathbf{u}(x,z) = (a(z,t), 0, -x\frac{da(z,t)}{dz}). \tag{3.12}$$

The gradient of the displacement field delivers one non-zero strain component, the axial strain under bending,

$$\epsilon_{zz} = \frac{\partial u_z}{\partial z} = -x\frac{d^2a}{dz^2}. \tag{3.13}$$

3.3 Derivation of the Dynamic Euler-Bernoulli Beam Equation

To analyze the dynamics of a beam under transverse forcing, we take note of *Solid Mechanics: A Variational Approach* by Dym and Shames [36], and start by determining the beam's total energy. Specifically, we compute the kinetic energy T, the strain (elastic) energy U, and the work W done by the external force. These quantities enter the Lagrangian L through Hamilton's principle, which states that the action is stationary for the actual path taken by the system. This variational formulation provides a systematic way to derive the governing equation of motion. We define the Lagrangian as

$$\mathcal{L} = T - U - W. \tag{3.14}$$

First, we evaluate the kinetic energy T. Assuming a constant cross sectional area A, uniform material density ρ, we obtain

$$\begin{aligned} T &= \frac{1}{2}\int_V \rho\dot{\mathbf{u}}\cdot\dot{\mathbf{u}}\,dV \\ &= \frac{1}{2}\rho\int_0^L\int_A\left(\dot{a}^2 + x^2\left(\frac{\partial\dot{a}}{\partial z}\right)^2\right)dA\,dz \\ &= \frac{1}{2}\rho A\int_0^L \dot{a}^2\,dz + \frac{1}{2}\rho I_y\int_0^L\left(\frac{\partial\dot{a}}{\partial z}\right)^2 dz. \end{aligned} \tag{3.15}$$

The leading term in Eq. (3.15) corresponds to translational kinetic energy and the second to rotational motion due to bending. For slender beams and low frequencies, the rotational contribution is negligible. We approximate

$$T \approx \frac{1}{2}\rho A \int_0^L \dot{a}^2 \, dz. \tag{3.16}$$

Second, we evaluate the strain energy contribution U. A general formulation for the strain energy is given by

$$U = \frac{1}{2}\int_V \left(\tau_{zz}\varepsilon_{zz} + \tau_{yy}\varepsilon_{yy} + \tau_{xx}\varepsilon_{xx} + 2\tau_{yz}\varepsilon_{yz} + 2\tau_{xz}\varepsilon_{xz} + 2\tau_{xy}\varepsilon_{xy}\right) dV. \tag{3.17}$$

Under the Euler-Bernoulli assumptions, all transverse normal and shear strain components vanish. Only the axial term $\tau_{zz}\epsilon_{zz}$ remains. With ε_{zz} from Eq. (3.13) and Hooke's law $\tau_{zz} = E\varepsilon_{zz}$, the strain energy is

$$U = \frac{1}{2}\int_V \tau_{zz}\epsilon_{zz}\, dV = \frac{E}{2}\int_0^L \left(\frac{d^2a}{dz^2}\right)^2 \left(\int_A x^2\, dA\right) dz = \frac{EI_y}{2}\int_0^L \left(\frac{d^2a}{dz^2}\right)^2 dz. \tag{3.18}$$

In Eq. (3.18) and also (3.15), we used the uniform cross section of the beam to factor out the area moment of inertia about the neutral axis, $\hat{\mathbf{y}}$,

$$I_y = \int_A x^2\, dA = \int_{-b/2}^{b/2}\int_{-h/2}^{h/2} x^2\, dx\, dy = \frac{b^3 h}{12}. \tag{3.19}$$

The product EI_y in Eq. (3.18) defines the flexural rigidity of the beam with respect to bending in the xz-plane. E sets the material-specific contribution and I_y the geometric contribution. A decrease in either results in a more compliant beam.

Third, we evaluate the work contribution W. The work done by the distributed load $q\,\hat{\mathbf{x}}$ is

$$W = -\int_0^L q(z,t)\,\hat{\mathbf{x}}\cdot\mathbf{u}(z,t)dz = -\int_0^L q(z,t)\,a dz. \tag{3.20}$$

We have evaluated all three energy contributions. With T,U, and W as derived, the Lagrangian becomes

$$\mathcal{L} = \int_0^L \left(\frac{1}{2}\rho A\dot{a}^2 - \frac{1}{2}EI\left(\frac{d^2a}{dz^2}\right)^2 + qa\right) dz. \tag{3.21}$$

We define the integrand of the Lagrangian via $\mathcal{L} = \int \ell(z)dz$ as the Lagrangian density per unit length

$$\ell(a) = \frac{1}{2}\rho A\dot{a}^2 - \frac{1}{2}EI_y\left(\frac{\partial^2 a}{\partial z^2}\right)^2 + qa, \tag{3.22}$$

which allows the application of Hamilton's principle in variational form. To derive the equation of motion, we perturb a between two instances of time, t_1 and t_2, by a small amount $\epsilon\eta(z,t)$, from

$a(z,t)$ to $a(z,t)+\epsilon\eta(z,t)$, letting the virtual displacement function η satisfy $\eta(z,t_1)=\eta(z,t_2)=0$ $\forall z\in[0,L]$, $\ell(a)$ experiences a perturbation to

$$\begin{aligned}\ell(a+\epsilon\eta) &= \frac{1}{2}\rho A\left(\dot{a}^2+2\epsilon\dot{a}\dot{\eta}+\epsilon^2\dot{\eta}^2\right)-\frac{1}{2}EI_y\left(\left(\frac{\partial^2 a}{\partial z^2}\right)^2+2\epsilon\frac{\partial^2 a}{\partial z^2}\frac{\partial^2\eta}{\partial z^2}+\epsilon^2\left(\frac{\partial^2\eta}{\partial z^2}\right)^2\right)+qa+\epsilon q\eta \\ &= \ell(a)+\epsilon\left(\rho A\dot{a}\dot{\eta}-EI_y\frac{\partial^2 a}{\partial z^2}\frac{\partial^2\eta}{\partial z^2}+q\,\eta\right)+O(\epsilon^2). \end{aligned} \tag{3.23}$$

Due to the perturbation, a variation in $\ell(a)$ occurs described by the variational operator δ applied to ℓ,

$$\delta\ell=\lim_{\epsilon\to 0}\frac{l(a+\epsilon\eta)-l(a)}{\epsilon}=\rho A\dot{a}\dot{\eta}-EI_y\frac{\partial^2 a}{\partial z^2}\frac{\partial^2\eta}{\partial z^2}+q\eta. \tag{3.24}$$

By Hamilton's Principle, which is based on variational calculus, the variation of the Lagrangian must vanish over the time interval $\int_{t_1}^{t_2}\delta\mathcal{L}dt=0$, such that

$$\delta\int_{t_1}^{t_2}\mathcal{L}\,dt=\int_{t_1}^{t_2}\int_0^L\delta\ell\,dz\,dt=H_1+H_2+H_3=0 \tag{3.25}$$

with

$$\begin{aligned} H_1 &= \int_{t_1}^{t_2}\int_0^L\rho A\dot{a}\dot{\eta}\,dz\,dt=\left[\int_0^L\rho A\dot{a}\eta\,dz\right]_{t_1}^{t_2}-\int_{t_1}^{t_2}\int_0^L\rho A\ddot{a}\eta\,dz\,dt=-\int_{t_1}^{t_2}\int_0^L\rho A\ddot{a}\eta\,dz\,dt, \\ H_2 &= -\int_{t_1}^{t_2}\int_0^L EI_y\frac{\partial^2 a}{\partial z^2}\frac{\partial^2\eta}{\partial z^2}\,dz\,dt \\ &= -\int_{t_1}^{t_2}\left[EI_y\frac{\partial^2 a}{\partial z^2}\frac{\partial\eta}{\partial z}\right]_0^L dt+\int_{t_1}^{t_2}\left[EI_y\frac{\partial^3 a}{\partial z^3}\eta\right]_0^L dt-\int_{t_1}^{t_2}\int_0^L EI_y\frac{\partial^4 a}{\partial z^4}\eta\,dz\,dt, \\ H_3 &= \int_{t_1}^{t_2}\int_0^L q\eta dzdt. \end{aligned} \tag{3.26}$$

From integration by parts, we find

$$H_1+H_2+H_3=\int_{t_1}^{t_2}\int_0^L\eta\left(-\rho A\,\ddot{a}\;-\;EI_y\,\partial_z^4 a\;+\;q\right)dz\,dt \tag{3.27}$$

$$+\left[-\;EI_y\left(\partial_z^2 a\right)\left(\partial_z\eta\right)\;+\;EI_y\left(\partial_z^3 a\right)\eta\right]_{z=0}^{z=L}=0. \tag{3.28}$$

Considering arbitrary η, where $\eta(z,t_1)=\eta(z,t_2)=0\;\forall z\in[0,L]$, Eq. (3.28) can be split into the dynamic beam equation and an equation for the boundary conditions:

$$\rho A\,\ddot{a}+EI_y\frac{\partial^4 a}{\partial z^4}-q=0,\qquad 0<z<L. \tag{3.29}$$

$$\left[-\;EI_y\frac{\partial^2 a}{\partial z^2}\frac{\partial\eta}{\partial z}\;+\;EI_y\frac{\partial^3 a}{\partial z^3}\eta\right]_0^L=0. \tag{3.30}$$

3.4 Boundary Conditions for the Cantilevered Beam

A cantilevered beam is defined as a beam clamped at one end ($z = 0$) and free at the other ($z = L$). For such a beam, we assume two boundary conditions for the displacement a

$$a(z = 0, t) = 0 \tag{3.31}$$

$$\frac{\partial a}{\partial z}\Big|_{z=0,t} = 0. \tag{3.32}$$

Consequently, η must be constrained accordingly, $\eta(z = 0, t) = 0$ and $d\eta/dz = 0$ for $z = 0, \forall t$. Simplifying the boundary condition Eq. (3.30), we find

$$\left(\frac{\partial^3 a}{\partial z^3}\eta - \frac{\partial^2 a}{\partial z^2}\frac{d\eta}{dz}\right)\Big|_{z=L} = 0 \tag{3.33}$$

However, because $\eta(z = L, t)$ and $d\eta(t)/dz$ for $z = L$ can be chosen arbitrarily, the terms in Eq. (3.33) must vanish separately, providing two additional boundary conditions

$$\frac{\partial^3 a}{\partial z^3}\eta\Big|_{z=L} = 0 \quad \Rightarrow \quad \frac{\partial^3 a}{\partial z^3}\Big|_{z=L} = 0, \tag{3.34}$$

$$\frac{\partial^2 a}{\partial z^2}\frac{d\eta}{dz}\Big|_{z=L} = 0 \quad \Rightarrow \quad \frac{d^2 a}{dz^2}\Big|_{z=L} = 0. \tag{3.35}$$

The four boundary conditions for the cantilever beam are required to find the mode shape function of the beam in the next section.

3.5 Vibrations of a Cantilever Beam

To find the time-dependent equation of motion and the spatial equation of motion (mode shape function) for the specific case of a cantilever beam, we work with the dynamic Euler-Bernoulli beam equation in frequency space:

$$-\omega^2 \rho A a(z, \omega) + E(\omega) I_y \frac{\partial^4 a(z, \omega)}{\partial z^4} = q(z, \omega). \tag{3.36}$$

Seeking mode shapes and modal magnitudes, we introduce the separable ansatz

$$a(z, \omega) = W(z)\delta x(\omega). \tag{3.37}$$

We begin by solving the homogeneous equation setting $q = 0$, to identify the mode shapes that will serve as a modal basis. Substitution of Eq. (3.37) into Eq. (3.36) yields the spatial differential equation and a separation constant λ^2[2]:

$$\frac{\partial^4 W}{\partial z^4} = \lambda^4 W, \tag{3.38}$$

[2] no boundary conditions applied yet

$$\lambda^4 = \frac{\rho A \omega^2}{E(\omega) I}. \tag{3.39}$$

With an exponential trial, we obtain a general solution to Eq. (3.38):

$$W(z) = C_1 \cosh(\lambda z) + C_2 \sinh(\lambda z) + C_3 \cos(\lambda z) + C_4 \sin(\lambda z). \tag{3.40}$$

Using the four boundary conditions for the cantilever, we obtain a linear system

$$\mathbf{A}(\lambda)\,\mathbf{c} = \begin{pmatrix} 1 & 0 & 1 & 0 \\ 0 & 1 & 0 & 1 \\ \cosh(\lambda L) & \sinh(\lambda L) & -\cos(\lambda L) & -\sin(\lambda L) \\ \sinh(\lambda L) & \cosh(\lambda L) & \sin(\lambda L) & -\cos(\lambda L) \end{pmatrix} \begin{pmatrix} C_1 \\ C_2 \\ C_3 \\ C_4 \end{pmatrix} = \mathbf{0}. \tag{3.41}$$

Nontrivial solutions $\mathbf{c} \neq 0$ exist only if $det(\mathbf{A}) = 0$. For a cantilever this evaluates to our characteristic equation [37]

$$\cos(\lambda L)\cosh(\lambda L) + 1 = 0. \tag{3.42}$$

The characteristic equation has a discrete set of solutions $\{\lambda_n L\}_{n=1}^{\infty}$. Each solution labels a flexural eigenmode. For that mode, $\lambda = \lambda_n$ is the spatial eigenvalue. For each λ_n, the associated mode shape $W_n(z)$ (i.e. the eigenfunction of mode n of Eq. (3.38)) is defined by

$$\begin{aligned} W_n(z) &= C_n b_n, \\ b_n &= \cosh(\lambda_n z) - \cos(\lambda_n z) - \Theta_n\big(\sinh(\lambda_n z) - \sin(\lambda_n z)\big), \\ \Theta_n &= \frac{\cos(\lambda_n L) + \cosh(\lambda_n L)}{\sin(\lambda_n L) + \sinh(\lambda_n L)}. \end{aligned} \tag{3.43}$$

The overall constant C_n fixes the normalization. We adopt tip normalization by choosing $C_n = 1/b_n(L)$ so that $W_n(L) = 1$. For later reference, we also define the tip-normalized mode shape $U_n(z) = W_n(z)/W_n(L)$. The mode shapes and their tip-normalized counterparts form a complete orthogonal basis along the beam with respect to the mass inner product. Accordingly, for a uniform beam with constant ρA,

$$\int_0^L \rho A U_m(z) U_n(z) dz = m_{e,n}\delta_{mn} \quad \text{where} \quad m_{e,n} = \kappa_n m \quad \text{and} \quad m = \rho A L. \tag{3.44}$$

κ_n depends on the mode (e.g. $\kappa_1 \approx 0.236$, $\kappa_2 \approx 0.219$) and m denotes the true mass of the beam. The tip-referred effective modal mass is $m_{e,n} = \kappa_n m$, e.g. $m_{e,1} \approx m/4$ [37]. Considering the orthogonal modal basis, we replace the single-product separation by a modal superposition, updating the initial separable ansatz in Eq. (3.37) to [17]

$$a(z, \omega) = \sum_{n=1} W_n \delta x_n(\omega). \tag{3.45}$$

The homogeneous problem ($q = 0$) provides us with the modal eigenfrequency-eigenvalue relation. For mode n with $\lambda = \lambda_n$ and, according to Eq. (3.39), the relation is

$$\omega_n^2 = E(\omega_n)\,\frac{\lambda_n^4 I}{\rho A}. \tag{3.46}$$

Using the complex modulus from Eq. (3.4), $E(\omega) = E_e(\omega)\big(1 - \frac{i}{Q(\omega)}\big)$, and treating $E_e(\omega_n)$ and $Q(\omega_n)$ as approximately constant near the eigenfrequency ω_n, we define the lossless (elastic) modal eigenfrequency $\omega_{e,n} = \lambda_n^4 I E_e/(\rho A)$. With this definition Eq. (3.46) becomes

$$\omega_n^2 = \omega_{e,n}^2 \left(1 - \frac{i}{Q}\right). \tag{3.47}$$

This phrasing separates stiffness carried by $\omega_{e,n}$ from loss carried by $1 - i/Q$ and concludes preliminaries for the forced problem.

In the forced problem, $q \neq 0$. Inserting the modal superposition from Eq. (3.45) into the frequency-domain beam Eq. (3.36):

$$EI_y \sum_{n=1} \frac{\partial^4 W_n(z)}{\partial z^4} \delta x_n(\omega) - \omega^2 \rho A \sum_{n=1}^{\infty} W_n(z) \delta x_n(\omega) = q(z, \omega). \tag{3.48}$$

Solving Eq. (3.46) for λ_n^4 and using it in Eq. (3.38), we replace the fourth derivative of W_n by the right hand side of Eq. (3.38). This yields

$$EI_y \sum_{n=1} \frac{\rho A}{E(\omega_n) I_y} \omega_n^2 \delta x_n(\omega) - \omega^2 \rho A \sum_{n=1}^{\infty} W_n(z) \delta x_n(\omega) = q(z, \omega). \tag{3.49}$$

Substitution of Eq. (3.47) into Eq. (3.48) yields

$$\rho A \sum_{n=1} \omega_{\mathrm{e,n}} \left(1 - \frac{i}{Q}\right) W_n \, \delta x_n(\omega) - \omega^2 \rho A \sum_{n=1}^{\infty} W_n(z) \delta x_n(\omega) = q(z, \omega). \tag{3.50}$$

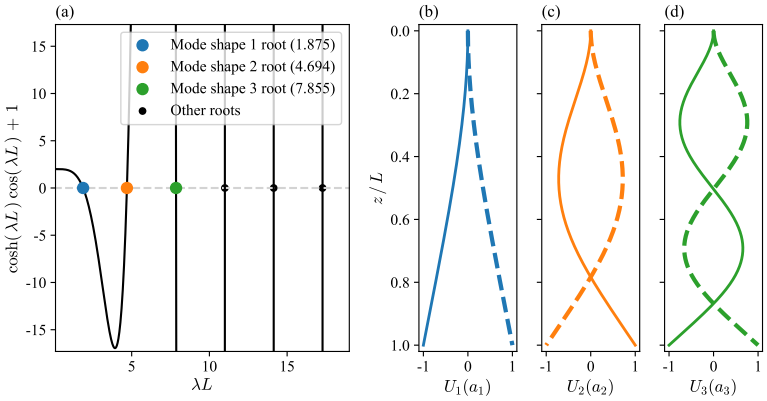

Fig. 3.2. Characteristic equation and mode shapes. (a) Determinant of the matrix A hosting the boundary conditons for the cantilever beam. Intersections with the abscissa (roots) denote solution points to the characteristic equation. (b, c, d) The three lowest order mode shapes for the cantilever beam.

Multiplication with any other mode shape $W_m(z)$ and integration over the beam length results in,

$$\rho A \int_0^L W_m(z) \sum_{n=1} [(1 - \frac{i}{Q})\omega_{\mathrm{e,n}}^2 - \omega^2] W_n(z) \delta x_n(\omega) dz = \int_0^L W_m(z) q(z,\omega) dz. \tag{3.51}$$

Using the orthogonality of W_n established in Eq. (3.44) and replacing the dummy subscript yields

$$\rho A \int_0^L W_n^2(z) dz \left[\omega_{\mathrm{e,n}}^2 - i\frac{\omega_{\mathrm{e,n}}^2}{Q} - \omega^2\right] \delta x_n(\omega) = \int_0^L W_n(z) q(z,\omega) dz. \tag{3.52}$$

With the tip-normalized mode shape U_n and using our tip-normalization $W_n(L) = 1$, we find

$$m_{\mathrm{e},n} \left[\omega_{\mathrm{e,n}}^2 - \omega^2 - i\frac{\omega_{\mathrm{e,n}}^2}{Q}\right] \delta x_n(\omega) = F_n(\omega) \tag{3.53}$$

with modal force

$$F_n(\omega) = \int_0^L U_n(z) q(z,\omega) dz. \tag{3.54}$$

We rearrange Eq. (3.53) to

$$\delta x_n(\omega) = \frac{F_n(\omega)}{m_{\mathrm{e},n}} \frac{1}{\omega_{\mathrm{e,n}}^2 - \omega^2 - i\frac{\omega_{\mathrm{e,n}}^2}{Q}}. \tag{3.55}$$

From here on we restrict attention to the fundamental flexural mode, $n = 1$. For notational simplicity, we drop the index and subscript 'e' keeping in mind that we work with effective quantities. We then define

$$k = \omega_0^2 m \quad \text{and} \quad \Gamma = \frac{m\omega_0}{Q} \tag{3.56}$$

and assuming that we are interested in a narrow band around resonance, $\omega \approx \omega_0$, the frequency-domain transfer from force $F(\omega)$ to modal response $\delta x(\omega)$ given by Eq. (3.55) may be approximated as

$$\delta x(\omega) = F(\omega) \frac{1}{k - m\omega^2 - i\omega_0\Gamma} \approx F(\omega) \frac{1}{k - m\omega^2 - i\omega\Gamma} \tag{3.57}$$

so that we identify the mechanical susceptibility

$$\chi(\omega) = \left[-m\omega^2 - i\omega\Gamma + k\right]^{-1} = \left[m\left(\omega_0^2 - \omega^2\right) - i\omega\Gamma\right]^{-1} \tag{3.58}$$

Back-transformation to the time domain exactly replicates the equation of motion of the damped harmonic oscillator in Eq. (2.1),

$$m\delta\ddot{x}(t) + \Gamma\delta\dot{x}(t) + k\delta x(t) = F(t). \tag{3.59}$$

We use this similarity as justification to describe the dynamics of a nanowire cantilever with the damped harmonic oscillator near resonance.

4. Force Sensing with a Nanowire Cantilever

Extending the single-degree-of-freedom oscillator to the two-degree-of-freedom nanowire in NW-MFM, we connect the damped harmonic oscillator picture to the dynamic Euler-Bernoulli beam description by projecting forces onto the nanowire's two orthogonal flexural modes and writing the coupled modal equations in terms of the nanowire's mechanical susceptibility and displacement-noise PSD. We show how force gradients enter as stiffness modifications of the modal spring constants and, crucially for MFM, how the frequency shift of each mode relates to the corresponding projected force gradient. This provides the working link between measured shifts, damping changes, and the underlying sample interactions.

4.1 Nanowire as Damped Harmonic Oscillator

Previously, we analyzed transverse beam vibrations assuming unidirectional bending, a simplification warranted by the beam's asymmetric cross sectional geometry. This asymmetry results in a smaller area moment of inertia I_y in one transverse direction, rendering the beam more flexible and thus more responsive to bending in that plane. Consequently, the displacement is treated as a scalar governed by the single bending rigidity EI_y. The motion then decomposes into a set of orthogonal bending modes, each described by a damped harmonic oscillator under thermal or external forcing.

Cantilevered nanowires, by contrast, typically possess nearly symmetric cross sections and exhibit high aspect ratios. The symmetry leads to comparable area moments of inertia in both transverse directions, allowing for significant deflection along either in-plane axis. This makes nanowires naturally suited for 2D modeling within the framework of the Euler-Bernoulli beam theory.

To describe the lateral deflection of a straight nanowire with longitudinal axis along $\hat{\mathbf{z}}$, we define an orthonormal basis $\{\hat{\mathbf{x}}, \hat{\mathbf{y}}\}$ spanning the transverse (cross sectional) plane. The position and displacement of the nanowire tip are

$$\mathbf{r}(t) = x(t)\hat{\mathbf{x}} + y(t)\hat{\mathbf{y}} \ , \quad \delta\mathbf{r}(t) = \delta x(t)\hat{\mathbf{x}} + \delta y(t)\hat{\mathbf{y}}. \tag{4.1}$$

Anticipating the likelihood of orthogonal nanowire oscillation directions we additionally define the secondary basis $\{\hat{\boldsymbol{a}}_1, \hat{\boldsymbol{a}}_2\}$. In this basis the displacement of the nanowire is denoted by

$$\delta\boldsymbol{a}(t) = A_1(t)\hat{\boldsymbol{a}}_1 + A_2(t)\hat{\boldsymbol{a}}_2. \tag{4.2}$$

In our analysis, let $\mathbf{f}(t)$ denote the force field projected onto the transverse plane. It captures the planar components of any potentially three-dimensional (3D) force to which the nanowire can dynamically respond. To describe the nanowire's dynamics, we model it as a 2D damped harmonic oscillator.

$$m\mathbf{I}\delta\ddot{\boldsymbol{r}}(t) + \boldsymbol{\Gamma}\delta\dot{\boldsymbol{r}}(t) + \boldsymbol{K}\delta\boldsymbol{r}(t) = \delta\mathbf{f}(t). \tag{4.3}$$

$\mathbf{I}$ is the 2×2 identity matrix, m is the *effective mass*, and $\boldsymbol{\Gamma}, \boldsymbol{K} \in \mathbb{R}^{2\times 2}$ are effective damping and stiffness matrices. We assume $\boldsymbol{\Gamma}$ to be symmetric and positive semi-definite. In the frequency domain, the nanowire's mechanical response is described by the susceptibility matrix

$$\boldsymbol{\chi}(\omega) = \left[-m\omega^2\boldsymbol{I} - i\omega\boldsymbol{\Gamma} + \boldsymbol{K}\right]^{-1} \tag{4.4}$$

which maps applied forces to resulting displacements via $\delta\boldsymbol{r}(\omega) = \boldsymbol{\chi}(\omega)\delta\mathbf{f}(\omega)$. The intrinsic modes of the system are obtained from the homogeneous problem $\boldsymbol{\chi}^{-1}(\omega)\delta\boldsymbol{r}(\omega) = 0$. The nontrivial solutions of the problem, where the nanowire responds most strongly to forcing, are the two complex eigenfrequencies $\Omega_{1,2} = \omega_{1,2} - i\Gamma_{1,2}/(2m)$. They are obtained by evaluating $\det(\boldsymbol{\chi}^{-1}(\omega)) = 0$ [17]. Equivalently, at each $\Omega_i (i = 1, 2)$ one eigenvalue of $\boldsymbol{\chi}^{-1}(\omega)$ vanishes. The real parts ω_i are the resonance frequencies. The imaginary parts set the modal linewidths (i.e. $-2\mathrm{Im}(\Omega_i)$). The associated eigenvectors of $\boldsymbol{\chi}^{-1}$ (equivalently, of $\boldsymbol{\chi}$ away from the poles) determine the displacement ellipses in the transverse plane. The normalized principal axes of these ellipses define two, in general non-orthogonal, mode directions $\hat{\boldsymbol{a}}_1'$, $\hat{\boldsymbol{a}}_2'$ [12, 18] visualized in Fig. 4.1.

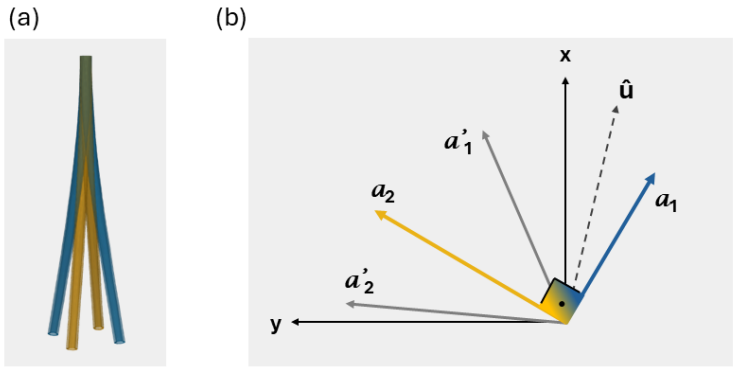

Fig. 4.1. Nanowire Oscillation directions. (a) Illustration of a nanowire oscillating along orthogonal mode directions $\hat{\boldsymbol{a}}_1, \hat{\boldsymbol{a}}_2$ (blue, orange). (b) Global xy coordinate system and coordinate system spanned by $\hat{\boldsymbol{a}}_1$ and $\hat{\boldsymbol{a}}_2$. General non-orthogonal mode directions are denoted by $\hat{\boldsymbol{a}}_1'$ and $\hat{\boldsymbol{a}}_2'$. $\hat{\mathbf{u}}$ denotes a measurement direction.

4.2 Conditions for Damping Separability

Still considering the homogeneous system $\chi^{-1}(\omega)\,\delta r(\omega) = 0$, the stiffness $\mathbf{K}$ and damping $\mathbf{\Gamma}$ generally contain off-diagonal elements that couple the two coordinates. When both $\mathbf{K}$ and $\mathbf{\Gamma}$ are symmetric, an orthogonal transformation exists that diagonalizes $\mathbf{K}$. Working in this $\mathbf{K}$-eigenbasis (primes omitted for readability) we set

$$K = \mathrm{diag}(k_1, k_2) = \begin{pmatrix} k_1 & 0 \\ 0 & k_2 \end{pmatrix} = \begin{pmatrix} m\,\omega_{11}^2 & 0 \\ 0 & m\,\omega_{22}^2 \end{pmatrix} \quad , \quad \Gamma = \begin{pmatrix} \Gamma_{11} & \Gamma_{12} \\ \Gamma_{12} & \Gamma_{22} \end{pmatrix}. \tag{4.5}$$

Further, we find eigenfrequencies

$$\Omega_1 = \omega_{11} + \frac{\omega_{11}\,\Gamma_{12}^2\,(\omega_{22}^2 - \omega_{11}^2)}{2\,s_1} + i\left(-\frac{\Gamma_{11}}{2m} + \frac{\omega_{11}^2\Gamma_{12}^2\Gamma_{22}}{2m\,s_1}\right), \tag{4.6}$$

$$\Omega_2 = \omega_{22} + \frac{\omega_{22}\,\Gamma_{12}^2\,(\omega_{11}^2 - \omega_{22}^2)}{2\,s_2} + i\left(-\frac{\Gamma_{22}}{2m} + \frac{\omega_{22}^2\Gamma_{12}^2\Gamma_{11}}{2m\,s_2}\right), \tag{4.7}$$

with $s_1 = \big(m(\omega_{22}^2 - \omega_{11}^2)\big)^2 + (\omega_{11}\Gamma_{22})^2$, $s_2 = \big(m(\omega_{11}^2 - \omega_{22}^2)\big)^2 + (\omega_{22}\Gamma_{11})^2$. The real parts of $\Omega_{1,2}$ give the resonance frequencies of the coupled system, while the imaginary parts set the damping rates. In each case, the term $-\Gamma_{ii}/(2m)$ is the diagonal (*separate*) damping of mode i, and the remaining fraction is the correction arising from the off-diagonal damping Γ_{12}. The latter is negligible, and each mode may be treated as independently damped, when

$$\frac{\omega_{11}^2\,\Gamma_{12}^2\,\Gamma_{22}}{[m(\omega_{22}^2 - \omega_{11}^2)]^2 + (\omega_{11}\Gamma_{22})^2} \ll \Gamma_{11} \quad \text{and} \quad \frac{\omega_{22}^2\,\Gamma_{12}^2\,\Gamma_{11}}{[m(\omega_{11}^2 - \omega_{22}^2)]^2 + (\omega_{22}\Gamma_{11})^2} \ll \Gamma_{22}. \tag{4.8}$$

In practice, these inequalities are satisfied whenever the off-diagonal damping is weak ($\Gamma_{12} \ll \min\{\Gamma_{11}, \Gamma_{22}\}$) or the modes are well separated in frequency ($|\omega_{22} - \omega_{11}|$ large so that $s_{1,2} \approx m^2(\omega_{22}^2 - \omega_{11}^2)^2$), in which case the off-diagonal contributions to the damping are negligible and each mode can be treated as independently damped.

4.3 Projected Susceptibility

The nanowire's displacement due to some sinusoidal forcing (actuation) is measured along a specific direction. We parameterize this measurement direction and similarly the forcing direction by angles α and β, respectively, via

$$\hat{\mathbf{u}}(\alpha) = (\cos(\alpha), \sin(\alpha))^T \quad \text{and} \quad \hat{\mathbf{v}}(\beta) = (\cos(\beta), \sin(\beta))^T. \tag{4.9}$$

The external forcing at angular frequency ω is represented by $\hat{\mathbf{v}}$ and a scalar phasor $F(\omega)$, encoding its magnitude and phase:

$$\delta\mathbf{f}(\omega) = \hat{\mathbf{v}}\,F(\omega). \tag{4.10}$$

The resulting displacement $\delta\boldsymbol{a}(\omega)$ is likewise represented by a complex amplitude. Its scalar projection onto the measurement direction $\hat{\mathbf{u}}$ is defined as

$$a_{\mathrm{p}}(\omega) = \hat{\mathbf{u}}^T \delta\boldsymbol{a}(\omega). \tag{4.11}$$

It generally is complex and can be expressed by its magnitude and phase:

$$a_{\mathrm{p}}(\omega) = \big|a_{\mathrm{p}}(\omega)\big| e^{i \arg\left(a_{\mathrm{p}}(\omega)\right)}. \tag{4.12}$$

Since the displacement relates to the forcing through the mechanical susceptibility $\boldsymbol{\chi}$, its projection is given by

$$a_{\mathrm{p}}(\omega) = \hat{\mathbf{u}}^T \boldsymbol{\chi}\, \hat{\mathbf{v}}\, F(\omega) \;\equiv\; \chi_{\mathrm{p}}(\omega)\, F(\omega), \tag{4.13}$$

where the projected susceptibility is defined as

$$\chi_{\mathrm{p}}(\omega) = \hat{\mathbf{u}}(\alpha)^T \boldsymbol{\chi}(\omega)\, \hat{\mathbf{v}}(\beta). \tag{4.14}$$

In the special case where the susceptibility has only diagonal entries, $\boldsymbol{\chi} = \mathrm{diag}(\chi_1, \chi_2)$, the projected susceptibility is

$$\chi_{\mathrm{p}}(\omega) = \cos(\alpha)\cos(\beta)\chi_1 + \sin(\alpha)\sin(\beta)\chi_2. \tag{4.15}$$

The displacement of the individual modes is obtained from $\chi_p(\alpha)F$ by choosing $\alpha = 0$ for mode 1 and $\alpha = \pi/2$ for mode 2 resulting in

$$A_1(\omega) = \chi_p(\alpha = 0)F = \chi_1 \cos(\beta)F \quad \text{and} \quad A_2(\omega) = \chi_p(\alpha = \pi/2)F = \chi_2 \cos(\beta)F. \tag{4.16}$$

Their magnitudes and phases $|A_i|$ and $\arg(A_i)$, $i = 1, 2$ relate to the phase and magnitude of a_p:

$$\begin{aligned} |a_p(\omega)|^2 = {} & \cos^2(\alpha)\,|A_1(\omega)|^2 + \sin^2(\alpha)\,|A_2(\omega)|^2 \\ & + \cos(\alpha)\,\sin(\alpha)\,|A_1(\omega)|\,|A_2(\omega)|\,\cos\big(\arg(A_1(\omega)) \;-\; \arg(A_2(\omega))\big), \end{aligned} \tag{4.17}$$

$$\begin{aligned} \arg\big(a_p(\omega)\big) = \arctan\Big[& \cos(\alpha)\,|A_1(\omega)|\,\sin\big(\arg(A_1(\omega))\big) + \sin(\alpha)\,|A_2(\omega)|\,\sin\big(\arg(A_2(\omega))\big), \\ & \cos(\alpha)\,|A_1(\omega)|\,\cos\big(\arg(A_1(\omega))\big) + \sin(\alpha)\,|A_2(\omega)|\,\cos\big(\arg(A_2(\omega))\big)\Big]. \end{aligned} \tag{4.18}$$

Interference terms are present in a_p which could lead to unreliable detection of $|A_1(\omega_1)|$ and $|A_2(\omega_2)|$ at low resonance frequency splitting, when not corrected. Also the phases are pushed together at low splitting possibly impacting phase-sensitive measurements. In our measurements, we assume $|a_p(\omega_1)| \gg |A_2(\omega_1)|$ and $|a_p(\omega_2)| \gg |A_1(\omega_2)|$ such that we can approximate

$$|a_p(\omega_1)|^2 \approx \cos^2(\alpha)|A_1(\omega_1)|^2 \quad \text{and} \quad |a_p(\omega_2)|^2 \approx \cos^2(\alpha)|A_2(\omega_2)|^2. \tag{4.19}$$

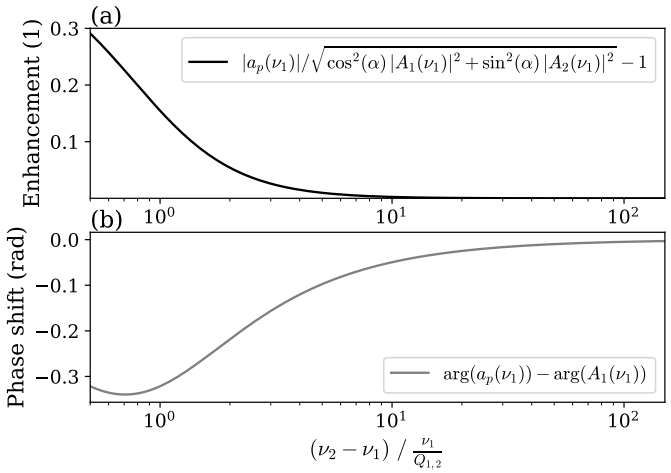

Fig. 4.2. Effects of interference contributions in a_p. (a) Relative magnitude enhancement at low resonance frequency splitting considering the line width. (b) Phase change at mode 1 due to the interference.

4.4 Projected Displacement-Noise Power Spectral Density

We now consider thermal forcing, $\delta\mathbf{f} = \mathbf{f}_{th}$, and focus on a displacement-noise PSD measurement projected along $\hat{\mathbf{u}} = (\cos(\alpha), \sin(\alpha))$. Under $\boldsymbol{\chi}^\dagger(\omega) = \boldsymbol{\chi}(-\omega)$ the FDT (Chap. 2, appendix A.3) provides the displacement-noise PSD[1]

$$\mathbf{S}_a(\omega) = \langle \delta\boldsymbol{a}(\omega)\, \delta\boldsymbol{a}(\omega)^\dagger \rangle = 4k_B T \boldsymbol{\chi}\, \boldsymbol{\Gamma}\, \boldsymbol{\chi}^\dagger. \tag{4.20}$$

The projected PSD along the defined direction is

$$S_{\mathrm{p}}(\omega, \alpha) = \hat{\mathbf{u}}^T \mathbf{S}_r(\omega) \hat{\mathbf{u}}. \tag{4.21}$$

Mapping S_{p} across a set of measurement angles $\alpha \in [0, \pi)$, one effectively probes the response of the nanowire in the transverse plane, and traces out the mode directions $\boldsymbol{a}_i$. If $\mathbf{K}$ is symmetric, the modes are orthogonal [38, 12]. In this case, the recorded PSD makes up a linear combination of the individual modes' displacement-noise PSDs projected onto the measurement direction:

$$S_{\mathrm{p}}(\omega, \alpha) = S_1(\omega)\cos^2(\alpha) + S_2(\omega)\sin^2(\alpha) \tag{4.22}$$

where $S_i(\omega) = \hat{\boldsymbol{a}}_i^T \mathbf{S}_r(\omega) \hat{\boldsymbol{a}}_i$ and α is the angle between $\hat{\mathbf{u}}$ and the direction of the softer (lower resonance frequency) mode along $\hat{\boldsymbol{a}}_1$. Assuming the nanowire exhibits naturally decoupled motion along $\boldsymbol{a}_1$ and $\boldsymbol{a}_2$, stiffness and damping matrices are diagonal, $\boldsymbol{K} = \mathrm{diag}(k_1, k_2)$ and $\boldsymbol{\Gamma} = \mathrm{diag}(\Gamma_1, \Gamma_2)$, respectively. The resulting PSD matrix is diagonal as well, $\boldsymbol{S}_a = \mathrm{diag}(S_1, S_2)$,

[1] $\mathbf{S}_a(-\omega) = \mathbf{S}_a^\dagger(\omega)$

with each entry corresponding to the displacement-noise PSD of an independent damped harmonic oscillator:

$$S_i(\omega) = 4k_B T\,\Gamma_i\,|\chi_i(\omega)|^2 = \frac{4k_B T}{m}\cdot\frac{\omega_\mathrm{i}/Q_i}{\left(\omega_\mathrm{i}^2-\omega^2\right)^2+\omega^2\left(\omega_\mathrm{i}/Q_i\right)^2}. \tag{4.23}$$

The linear combination of $S_i(\omega)$ with mode indices $i = 1, 2$ in Eq. (4.22) plus an offset constant N yield the measured displacement-noise PSD

$$S_\mathrm{meas} = S_p(\omega, m, T, \alpha, \omega_1, \omega_2, Q_1, Q_2) + N. \tag{4.24}$$

With Eq. (4.24) we can extract a nanowire's mechanical parameters and quantify its force sensitivity. To demonstrate that, we consider the displacement-noise PSD from an optical projection measurement of a nanowire's displacement in Fig. 4.3. A fit of the measurement data to Eq. (4.24) yields resonance frequencies (ν_i), quality factors (Q_i), the measurement angle α, and the effective mass (m). Using these parameters we calculate S_p, S_i and the (theoretical) susceptibility function assuming orthogonal mode directions. We can also compute the nanowire's spring and damping constants, $k_i = m\omega_i^2 \approx 1.4\ \mathrm{mN\,m^{-1}}$ and $\Gamma_i = m\omega_i/Q_i \approx 2.5\times10^{-13}\ \mathrm{kg\,s^{-1}}$, respectively, and determine the square root of the force-noise PSD $(S_{F,i})^{1/2} \approx 35\ \mathrm{aN\,Hz^{-1/2}}$.

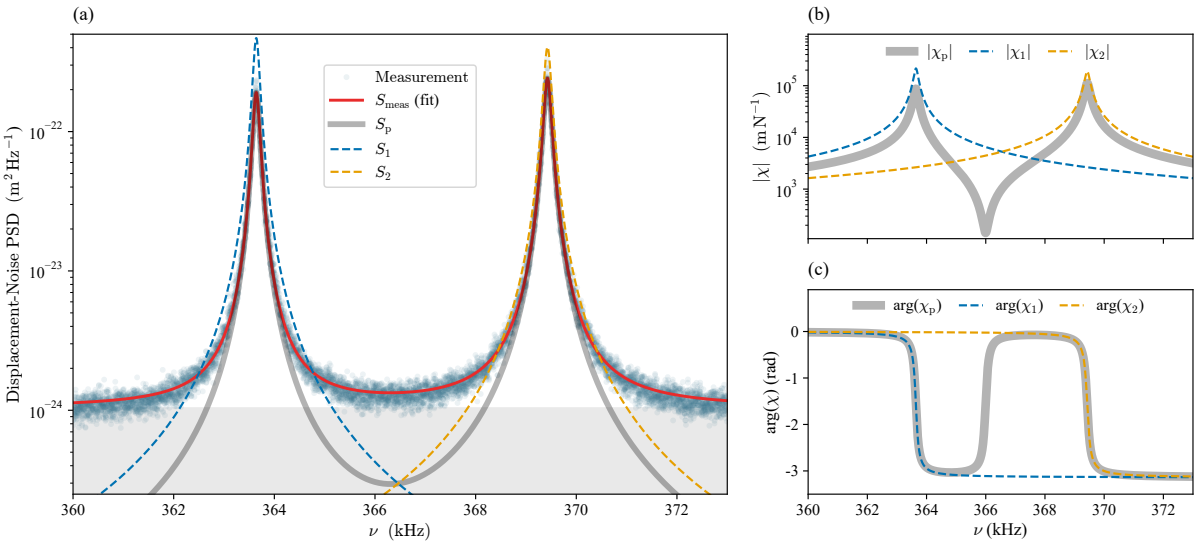

Fig. 4.3. Displacement-Noise PSD and inferred mechanical susceptibility. (a) Measured spectrum of a Si nanowire. Red fit according to Eq. (4.24) yields values $\nu_1 \approx 363.641$ kHz, $\nu_2 \approx 369.428$ kHz, $Q_1 \approx 2550$, $Q_2 \approx 2300$ (pressure of approximately 10^{-5} mbar), $\alpha = 50°$, $m \approx 0.26\cdot10^{-15}$ kg ($T = 90$ K), $N = 10^{-24}$ $\mathrm{m^2\,Hz^{-1}}$. The values are used to reconstruct S_p (grey) and S_i (blue, orange dashed) according to Eqs. (4.22) and (4.23). (b, c) Magnitude and phase of the susceptibility based on Eq. (2.2), the single-degree-of-freedom damped harmonic oscillator, and Eq. (4.15) assuming $\alpha = \beta$.

4.5 Static External Force

In additon to the thermal force, the nanowire is subject to a small, static but position-dependent force $\mathbf{f}_{\text{ext}}(\mathbf{a}_o)$, such that $\delta\mathbf{f} = \mathbf{f}_{\text{ext}} + \mathbf{f}_{\text{th}}$. Assuming small displacements (i.e. linear response), we approximate the external force by a first-order Taylor expansion at the nanowire's equilibrim position $\mathbf{a}_o$:

$$\mathbf{f}_{\text{ext}}(\boldsymbol{a}) \approx \mathbf{f}_{\text{ext}}(\boldsymbol{a_o}, t) + \mathbf{J}^{\text{NW}}\delta\boldsymbol{a}(t), \quad \text{with} \quad \mathbf{J}^{\text{NW}} = (\nabla^{\text{NW}}\mathbf{f}_{\text{ext}})|_{\boldsymbol{a}=\boldsymbol{a}_o}\,. \tag{4.25}$$

The first term, $\mathbf{f}_{\text{ext}}(\boldsymbol{a}_o)$, shifts the static equilibrium position, but does not affect frequency-domain analysis. (As long as we are in the linear response regime). The second term contains the Jacobian in the nanowire-basis with the spatial derivatives $f_{ij}(\mathbf{a}) = \partial f_i(\mathbf{a})/\partial a_j$. It introduces a position-dependent stiffness,

$$\mathbf{K} = \text{diag}(k_1, k_2) + \mathbf{J}^{\text{NW}} = \begin{pmatrix} k_1 - f_{11} & -f_{12} \\ -f_{21} & k_1 - f_{22}. \end{pmatrix}$$

Thermal spectra indicate the nanowires operate in the underdamped regime, $\Gamma_i^2 \ll 4k_i m$, implying $Q \gg 1$. We therefore neglect damping in the susceptibility, approximating $\boldsymbol{\chi} \approx (-m\omega^2\mathbf{I} + \mathbf{K})^{-1}$. The squared eigenfrequencies of $\boldsymbol{\chi}$ are given by

$$\omega_{1,2}^2 = \frac{-f_{11} - f_{22} + k_1 + k_2 \pm \sqrt{\Delta}}{2m}, \quad \Delta = (f_{11} - f_{22} + k_1 - k_2)^2 + 4f_{12}f_{21},$$

and correspond to the poles of the eigenvalues of $\boldsymbol{\chi}$, or equivalently, to the roots of $\det(\boldsymbol{\chi}^{-1}) = 0$. The associated eigenvectors, which align with those of the modified stiffness matrix $\mathbf{K}$, are frequency-independent and define the modified mode directions,

$$\boldsymbol{a}_1' = \begin{pmatrix} k_2 - f_{22} - m\omega_1^2 \\ f_{12} \end{pmatrix}, \quad \boldsymbol{a}_2' = \begin{pmatrix} f_{21} \\ k_1 - f_{11} - m\omega_2^2 \end{pmatrix}.$$

If the force is conservative (i.e. $\nabla^{\text{NW}} \times \mathbf{f}_{\text{ext}} = 0$), then $f_{12} = f_{21}$, ensuring that $\mathbf{K}$ remains symmetric and the mode directions are orthogonal, $\boldsymbol{a}_1' \cdot \boldsymbol{a}_2' = 0$. Assuming $\sqrt{4f_{12}f_{21}} \ll |f_{11} - f_{22} + k_1 - k_2| \geq 0$, and $f_{ii} \ll k_i$, we find

$$\omega_i \approx \sqrt{\frac{k_i - f_{ii}}{m}} = \sqrt{\frac{k_i}{m}\left(1 - \frac{f_{ii}}{k_i}\right)} \approx \sqrt{\frac{k_i}{m}}\left(1 - \frac{1}{2}\frac{f_{ii}}{k_i}\right) = \omega_{\text{i,th}} - \frac{\omega_{\text{i,th}}}{2k_i} f_{ii}. \tag{4.26}$$

Note that $\omega_{\text{i,th}}$ represent reference resonance frequencies of the nanowires in the absence of any but thermal forces. With $\omega_i = 2\pi\nu_i$, the frequency shifts are

$$\Delta\nu_i = -\frac{\nu_{\text{i,th}}}{2k_i} f_{ii} = -\frac{1}{8m\pi^2}\frac{1}{\nu_{\text{i,th}}}\frac{\partial f_{\text{i,ext}}}{\partial a_i}. \tag{4.27}$$

This expression provides the foundation for nanowire-based force sensing via frequency shifts in spectral measurements.

5. Magnetic Imaging

This final theory chapter applies the previous results to the specific case of magnetic interactions, explicitly neglecting all non-magnetic interactions. We describe models for tip-sample coupling, from effective monopole approximations to field gradient sensitivities, and discuss how these models determine the contrast mechanism of NW-MFM. In addition to static stray field contrast, we include susceptibility-related contrast, where a sample's temperature-dependent response to the nanowire tip modifies the signal. Within the monopole approximation, we show how the projected force gradient signals along the nanowire modes map directly onto the conventional MFM signal measured with micro-cantilevers, providing a clear correspondence to established interpretations. We also introduce limits to magnetic sensitivity and tip-induced perturbations. This concludes the theoretical framework by showing how the magnetic and mechanical descriptions merge, giving rise to the imaging signals measured in NW-MFM experiments.

5.1 Tip-Sample Interaction Force

We have established that the resonance frequency shifts of a nanowire provide a means to probe weak external force gradients, $f_{ii} \ll k_i$. To probe magnetic force gradients in particular, we derive explicit expressions for the force gradients arising from the interaction between a magnetic tip and the spatially varying stray field of a magnetic sample.

We consider a magnetic nanowire oscillating within a plane of constant height z above the sample surface. This vibrational plane lies parallel to the surface and is embedded in a global coordinate system where the lateral directions are denoted $\hat{\mathbf{x}}$ and $\hat{\mathbf{y}}$. Let $\mathbf{r} = x\hat{\mathbf{x}} + y\hat{\mathbf{y}}$ represent the in-plane position and define the tip apex position as $\mathbf{R} = \mathbf{r} + z\hat{\mathbf{z}}$. Coordinates at the tip described with respect to the tip apex are $\mathbf{R}' = x'\hat{\mathbf{x}} + y'\hat{\mathbf{y}} + z'\hat{\mathbf{z}}$ and $\mathbf{r}' = x'\hat{\mathbf{x}} + y'\hat{\mathbf{y}}$. A point in space, $\mathbf{R} + \mathbf{R}'$, contributes to the magnetostatic interaction energy given by [39, 40, 41, 42]

$$E_m(\mathbf{R}) = -\mu_0 \int \mathbf{M}_{\text{tip}}(\mathbf{R}') \cdot \mathbf{H}(\mathbf{R} + \mathbf{R}')\, \mathrm{d}^3\mathbf{R}'. \tag{5.1}$$

$\mathbf{M}_{\text{tip}}$ is the magnetization of the nanowire's magnetic tip and $\mathbf{H}$ is the stray field emanating from a magnetic or current-carrying sample. By expressing the magnetic field as the gradient of a scalar potential, $\mathbf{H} = -\nabla\phi$, and recognizing the fact that ϕ depends only on $\mathbf{R} + \mathbf{R}'$, we use

the chain rule [1] and integration by parts to rewrite the energy expression:

$$\begin{aligned} E_m(\mathbf{R}) &= \mu_0 \int \mathbf{M}_{\text{tip}}(\mathbf{R}') \cdot \nabla \phi(\mathbf{R} + \mathbf{R}') \, \mathrm{d}^3\mathbf{R}' \\ &= \mu_0 \int \mathbf{M}_{\text{tip}}(\mathbf{R}') \cdot \nabla_{\mathbf{R}'} \phi(\mathbf{R} + \mathbf{R}') \, \mathrm{d}^3\mathbf{R}' \\ &= \mu_0 \int \rho_{\text{tip}}(\mathbf{R}') \, \phi(\mathbf{R} + \mathbf{R}') \, \mathrm{d}^3\mathbf{R}' + \mu_0 \int_{\partial V} \sigma_{\text{tip}}(\mathbf{R}') \, \phi(\mathbf{R} + \mathbf{R}') \, dS', \end{aligned} \tag{5.2}$$

where $\rho_{\text{tip}} = -\nabla_{\mathbf{R}'} \cdot \mathbf{M}_{\text{tip}}(\mathbf{R}')$ is the tip's effective magnetic volume charge density, and $\sigma_{\text{tip}} = \mathbf{M}_{\text{tip}}(\mathbf{R}') \cdot \hat{\mathbf{n}}'$ the effective magnetic surface charge density (SI: A), with $\hat{\mathbf{n}}'$ denoting the outward normal of the tip's surface, including any internal discontinuities in $\mathbf{M}_{\text{tip}}$. Eq. (5.2) highlights that the magnetostatic energy is determined by the convolution of the sample's scalar magnetic potential with the tip's effective magnetic charge distribution.

The magnetic force acting on the tip (nanowire) is derived from the spatial gradient of the magnetostatic energy. The gradient is taken with respect to the tip position $\mathbf{R}$. Considering the field-based form of the energy, Eq. (5.1), and noting that the tip magnetization is independent of $\mathbf{R}$, while assuming $\nabla \times \mathbf{H} = 0$ (magnetostatics), the force becomes [2]

$$\mathbf{F}(\mathbf{R}) = -\nabla E_m(\mathbf{R}) = \mu_0 \int (\mathbf{M}_{\text{tip}}(\mathbf{R}') \cdot \nabla) \mathbf{H}(\mathbf{R} + \mathbf{R}') \, d^3\mathbf{R}'. \tag{5.3}$$

The magnetic charge formulation of the energy, Eq. (5.2), offers an alternative route to the force that emphasizes the role of effective magnetic charges. This is particularly advantageous, when the tip's magnetization can be described as a distribution of idealized magnetic charges. Taking the gradient of this energy formulation yields

$$\begin{aligned} \mathbf{F}(\mathbf{R}) &= -\mu_0 \int \rho_{\text{tip}}(\mathbf{R}') \, \nabla \phi(\mathbf{R} + \mathbf{R}') \, d^3\mathbf{R}' - \mu_0 \int_{\partial V} \sigma_{\text{tip}}(\mathbf{R}') \, \nabla \phi(\mathbf{R} + \mathbf{R}') \, dS' \\ &= \mu_0 \int \rho_{\text{tip}}(\mathbf{R}') \, \mathbf{H}(\mathbf{R} + \mathbf{R}') \, d^3\mathbf{R}' + \mu_0 \int_{\partial V} \sigma_{\text{tip}}(\mathbf{R}') \, \mathbf{H}(\mathbf{R} - \mathbf{R}') \, dS'. \end{aligned} \tag{5.4}$$

5.2 Effective Magnetic Charge

To connect measured frequency shifts to the spatial structure of the sample's stray field, we express the force in $\mathbf{k}$-space following the transfer function approach by Hug et al. [43, 44]. We derive expressions for the force by transforming both real-space formulations: the field-based expression from Eq. (5.3) and the charge-based expression from Eq. (5.4).

[1] If $\tilde{x}(x, x') = x + x'$, and $\phi(\tilde{x})$ arbitrary, then $\frac{\partial \phi}{\partial x} = \frac{\partial \phi}{\partial \tilde{x}} \frac{\partial \tilde{x}}{\partial x} = \frac{\partial \phi}{\partial \tilde{x}} \frac{\partial \tilde{x}}{\partial x'} = \frac{\partial \phi}{\partial x'}$.
[2] $\nabla(\mathbf{M} \cdot \mathbf{H}) = (\mathbf{M} \cdot \nabla)\mathbf{H} + (\mathbf{H} \cdot \nabla)\mathbf{M} - \mathbf{M} \times (\nabla \times \mathbf{H}) - \mathbf{H} \times (\nabla \times \mathbf{M})$

The **k**-space expression for the in-plane force field at fixed height z with in-plane wavevector $\mathbf{k} = (k_x, k_y)$ is defined as

$$\mathbf{F}(\mathbf{k}, z) = \mu_0 \int \mathbf{F}(\mathbf{r}, z) e^{-i\mathbf{k}\cdot\mathbf{r}}\, d^2\mathbf{r}. \tag{5.5}$$

We first evaluate the field-based expression. Inserting Eq. (5.3) into Eq. (5.5), and substituting $\tilde{\mathbf{r}} = \mathbf{r} + \mathbf{r}'$ adjusting the gradient operator ∇ to $\nabla_{(\tilde{\mathbf{r}},z)} = (\partial_{\tilde{x}}, \partial_{\tilde{y}}, \partial_z)$. Accordingly, we obtain

$$\begin{aligned}
\mathbf{F}(\mathbf{k}, z) &= \mu_0 \int \mathbf{M}_{\text{tip}}(\mathbf{R}') \cdot \left(\int \nabla \mathbf{H}(\mathbf{r} + \mathbf{r}', z + z')\, e^{-i\mathbf{k}\cdot\mathbf{r}}\, d^2\mathbf{r} \right) d^3\mathbf{R}' \\
&= \mu_0 \int \left(\int \mathbf{M}_{\text{tip}}(\mathbf{R}') e^{i\mathbf{k}\cdot\mathbf{r}'} d^2r' \right) \cdot \left(\int \nabla_{(\tilde{\mathbf{r}},z)} \mathbf{H}(\tilde{\mathbf{r}}, z + z')\, e^{-i\mathbf{k}\cdot\tilde{\mathbf{r}}}\, d^2\tilde{\mathbf{r}} \right) dz' \\
&= \mu_0 \int \mathbf{M}^*_{\text{tip}}(\mathbf{k}, z') \cdot \nabla_{(\mathbf{k},k)} \mathbf{H}(\mathbf{k}, z + z')\, dz'.
\end{aligned} \tag{5.6}$$

We identify the stray field, $\mathbf{H}(\mathbf{k}, z + z')$ and tip magnetization $\mathbf{M}^*_{\text{tip}}(\mathbf{k}, z')$ in **k**-space. Assuming that the stray field decays exponentially with vertical distance, $\mathbf{H}(\mathbf{k}, z + z') = \mathbf{H}(\mathbf{k}, z) e^{-kz'}$, we integrate by parts to find [20]

$$\mathbf{F}(\mathbf{k}, z) = \mu_0 \left(\int \nabla_{(\mathbf{k},k)} \cdot \mathbf{M}^*_{\text{tip}}(\mathbf{k}, z') e^{-kz'}\, dz' \right) \mathbf{H}(\mathbf{k}, z). \tag{5.7}$$

Let us turn to the charge-based expression of the force given in Eq. (5.4). Inserting it into Eq. (5.5), we proceed analogously to the field-based case:

$$\begin{aligned}
\mathbf{F}(\mathbf{k}, z) &= \mu_0 \int \left(\int \rho_{\text{tip}}(\mathbf{r}', z') \mathbf{H}(\mathbf{r} + \mathbf{r}', z + z')\, e^{-i\mathbf{k}\cdot\mathbf{r}}\, d^3R' \right) d^2\mathbf{r} \\
&\quad + \mu_0 \int \left(\oint_S \sigma_{\text{tip}}(\mathbf{r}', z') \mathbf{H}(\mathbf{r}, z + z')\, e^{-i\mathbf{k}\cdot\mathbf{r}} dS' \right) d^2\mathbf{r} \\
&= \mu_0 \int \left(\int \rho_{\text{tip}}(\mathbf{r}', z')\, e^{i\mathbf{k}\cdot\mathbf{r}'} d^2\mathbf{r}' \right) \left(\int_V \mathbf{H}(\tilde{\mathbf{r}}, z + z')\, e^{-i\mathbf{k}\cdot\tilde{\mathbf{r}}} d^2\tilde{\mathbf{r}} \right) dz' \\
&\quad + \mu_0 \oint_S \sigma_{\text{tip}}(\mathbf{r}', z')\, e^{i\mathbf{k}\cdot\mathbf{r}'} \left(\int \mathbf{H}(\tilde{\mathbf{r}}, z + z')\, e^{-i\mathbf{k}\cdot\tilde{\mathbf{r}}} d^2\tilde{\mathbf{r}} \right) dS' \\
&= \mu_0 \int \rho^*_{\text{tip}}(\mathbf{k}, z') \mathbf{H}(\mathbf{k}, z + z') dz' \\
&\quad + \mu_0 \oint_S \sigma_{\text{tip}}(\mathbf{r}', z')\, e^{i\mathbf{k}\cdot\mathbf{r}'} \mathbf{H}(\mathbf{k}, z + z') dS' \\
&= \mu_0 \left(\int \rho^*_{\text{tip}}(\mathbf{k}, z') e^{-kz'} dz' + \oint_S \sigma_{\text{tip}}(\mathbf{r}', z')\, e^{i\mathbf{k}\cdot\mathbf{r}'} e^{-kz'} dS' \right) \mathbf{H}(\mathbf{k}, z).
\end{aligned} \tag{5.8}$$

Comparing Eq. (5.7) and Eq. (5.8), we identify

$$\sigma^*_{\text{tip,eff}}(\mathbf{k}) = \int \nabla_{(\mathbf{k},k)} \cdot \mathbf{M}^*_{\text{tip}}(\mathbf{k}, z') e^{-kz'}\, dz' = \int \rho^*_{\text{tip}}(\mathbf{k}, z') e^{-kz'} dz' + \oint_S \sigma_{\text{tip}}(\mathbf{r}', z')\, e^{i\mathbf{k}\cdot\mathbf{r}'} e^{-kz'} dS', \tag{5.9}$$

where $\sigma_{\text{tip,eff}}(\mathbf{k})$ (SI unit: A·m) represents the effective surface magnetic charge density of the tip in **k**-space [32].

5.3 Static Stray Field Gradients

Since the magnetic force derives from a scalar potential ($\mathbf{F} = -\nabla E_m$), it is conservative and satisfies $\nabla \times \mathbf{F} = 0$. Consequently, the associated force gradient matrix $\nabla\mathbf{F}$ is symmetric. In the context of in-plane nanowire oscillations, only the in-plane components f_{xx}, f_{xy}, and f_{yy} are relevant. These elements enter the effective stiffness matrix of the nanowire and determine both the resonance frequency shifts and the orientation of the vibrational modes. We therefore restrict our attention to the in-plane submatrix $\mathbf{J}$.

$$\text{Considering} \quad \nabla\mathbf{F}(\mathbf{R}) = \begin{pmatrix} f_{xx} & f_{xy} & \cdot \\ f_{xy} & f_{yy} & \cdot \\ \cdot & \cdot & \cdot \end{pmatrix}, \quad \text{let} \quad \mathbf{J} = \begin{pmatrix} f_{xx} & f_{xy} \\ f_{xy} & f_{yy} \end{pmatrix}. \tag{5.10}$$

In $\mathbf{k}$-space, we have $\mathbf{J}(\mathbf{k})$ with components

$$f_{xx}(\mathbf{k}) = i\,\mu_0\,k_x\,\sigma^*_{\text{tip,eff}}(\mathbf{k})\,H_x(\mathbf{k}), \tag{5.11}$$

$$f_{xy}(\mathbf{k}) = i\,\mu_0\,k_x\,\sigma^*_{\text{tip,eff}}(\mathbf{k})\,H_y(\mathbf{k}), \tag{5.12}$$

$$f_{yy}(\mathbf{k}) = i\,\mu_0\,k_y\,\sigma^*_{\text{tip,eff}}(\mathbf{k})\,H_y(\mathbf{k}). \tag{5.13}$$

We now seek to express $\mathbf{J}(\mathbf{k})$ in the nanowire's intrinsic coordinate frame, defined by the mode directions $\hat{\boldsymbol{a}}_1$ and $\hat{\boldsymbol{a}}_2$, which serve as an orthonormal basis (provided $\boldsymbol{K}$ is symmetric). We define $\hat{\boldsymbol{a}}_1$ to lie at an angle α with respect to the global $\hat{\mathbf{x}}$-axis, which also serves as the measurement axis, $\hat{\mathbf{x}} = \hat{\mathbf{u}}$. Specifically, $\hat{\boldsymbol{a}}_1 = \cos(\alpha)\hat{\mathbf{x}} + \sin(\alpha)\hat{\mathbf{y}}$, and by orthogonality, $\hat{\boldsymbol{a}}_2 = -\sin(\alpha)\hat{\mathbf{x}} + \cos(\alpha)\hat{\mathbf{y}}$. To express the force gradient matrix in the nanowire frame, we apply a similarity transformation using a rotation matrix $\mathbf{P}$ which maps vectors from the global frame to the nanowire frame. $\mathbf{P}$ carries $\hat{\boldsymbol{a}}_1$ and $\hat{\boldsymbol{a}}_2$ as its columns.

$$\mathbf{J}^{\text{NW}}(\mathbf{k}) = \begin{pmatrix} f_{11}(\mathbf{k}) & f_{12}(\mathbf{k}) \\ f_{12}(\mathbf{k}) & f_{22}(\mathbf{k}) \end{pmatrix} = P^\top \mathbf{J}(\mathbf{k}) P, \quad \text{with} \quad P = \begin{pmatrix} \cos\alpha & -\sin\alpha \\ \sin\alpha & \cos\alpha \end{pmatrix}.$$

The components of $\mathbf{J}^{\text{NW}}(\mathbf{k})$ are

$$f_{11}(\mathbf{k}) = \cos^2(\alpha)\,f_{xx}(\mathbf{k}) + 2\cos(\alpha)\sin(\alpha)\,f_{xy} + \sin^2(\alpha)\,f_{yy}, \tag{5.14}$$

$$f_{22}(\mathbf{k}) = \sin^2(\alpha)\,f_{xx}(\mathbf{k}) - 2\cos(\alpha)\sin(\alpha)\,f_{xy} + \cos^2(\alpha)\,f_{yy}(\mathbf{k}), \tag{5.15}$$

$$f_{12}(\mathbf{k}) = f_{21}(\mathbf{k}) = (\cos^2(\alpha) - \sin^2(\alpha))\,f_{xy}(\mathbf{k}) + \cos(\alpha)\sin(\alpha)\,(f_{yy}(\mathbf{k}) - f_{xx}(\mathbf{k})). \tag{5.16}$$

Using Eq. (4.27) and assuming that the magnetic interaction between nanowire and sample dominates over any electrostatic or van der Waal's forces, the two frequency shifts of the two orthogonal modes in $\mathbf{k}$-space are

$$\Delta\nu_1(\mathbf{k}) = -i\,\mu_0\,\sigma^*_{\text{tip,eff}}(\mathbf{k})\,\frac{\nu_{1,\text{th}}}{2k_1}\left(\hat{H}_x\cos(\alpha) + \hat{H}_y\sin(\alpha)\right)(k_x\cos(\alpha) + k_y\sin(\alpha)) \tag{5.17}$$

$$\Delta\nu_2(\mathbf{k}) = -i\,\mu_0\,\sigma^*_{\text{tip,eff}}(\mathbf{k})\,\frac{\nu_{2,\text{th}}}{2k_2}\left(\hat{H}_x\sin(\alpha) + \hat{H}_y\cos(\alpha)\right)(-k_x\sin(\alpha) + k_y\cos(\alpha)). \tag{5.18}$$

If both frequency shifts are known, we rearrange Eq. (4.27):

$$f_{11}(\mathbf{k}) = -\frac{2k_1}{\nu_{1,\mathrm{th}}}\Delta\nu_1(\mathbf{k}), \qquad f_{22}(\mathbf{k}) = -\frac{2k_2}{\nu_{2,\mathrm{th}}}\Delta\nu_2(\mathbf{k}). \tag{5.19}$$

Summation of the two [3] diagonal force gradient elements yields

$$\begin{aligned} f_+(\mathbf{k}) &= -\big(f_{11}(\mathbf{k}) + f_{22}(\mathbf{k})\big) = \frac{2k_1}{\nu_{1,\mathrm{th}}}\,\Delta\nu_1(\mathbf{k}) + \frac{2k_2}{\nu_{2,\mathrm{th}}}\,\Delta\nu_2(\mathbf{k}) \\ &= -i\,\mu_0\,\sigma^*_{\mathrm{tip,eff}}(\mathbf{k})\,\big(k_x H_x(\mathbf{k}) + k_y H_y(\mathbf{k})\big) \\ &= -\mu_0\,\sigma^*_{\mathrm{tip,eff}}(\mathbf{k})\,k\,H_z(\mathbf{k})\,. \end{aligned} \tag{5.20}$$

This relation is independent of the measurement angle α (trace invariance under rotation) and links measurable frequency shifts directly to the z-component of the sample's stray field in $\mathbf{k}$-space, allowing direct comparison with conventional MFM images. Another notable configuration is obtained with $\alpha = 45\ ^\circ$ when subtracting the two measurement signals,

$$\begin{aligned} f_- &= f_{22} - f_{11} \\ &= -\cos(2\alpha)\,(f_{xx} - f_{yy}) - 4\cos\alpha\,\sin\alpha\,f_{xy} \\ &= \frac{2k_2}{\nu_{2,\mathrm{th}}}\,\Delta\nu_2(\mathbf{k}) - \frac{2k_1}{\nu_{1,\mathrm{th}}}\,\Delta\nu_1(\mathbf{k}) \\ &= \mu_0\,\sigma^*_{\mathrm{tip,eff}}(\mathbf{k})\,i\big(k_y H_x(\mathbf{k}) + k_x H_y(\mathbf{k})\big) \\ &= 2f_{xy}(\mathbf{k}). \end{aligned} \tag{5.21}$$

This allows to access the sum of the off-diagonal field gradients.

In MFM imaging, we either display the raw measured resonance frequency shifts ν_i or explicitly plot the trace of the force gradients, $f_+ = -(f_{11} + f_{22})$.

5.4 Cylindrical Magnetic Tip and Effective Magnetic Monopole

We employ elongated magnetic tips in NW-MFM to facilitate signal interpretation. Their elongation produces a strong shape anisotropy that fixes the tip magnetization along the tip axis, preventing it from being altered by the sample's stray field. This stability ensures that the measured signal reflects only the sample response, rather than a convolution of unknown tip and sample magnetizations. The elongated geometry also justifies the use of the effective magnetic monopole model, which simplifies the interpretation of MFM contrast. This model allows simple MFM contrast interpretation. We now derive this model by describing the nanowire tip as a uniformly magnetized cylinder of length L and radius R, magnetized along $-\hat{\mathbf{z}}$, $\mathbf{M} = -M_z\hat{\mathbf{z}}$ (saturation magnetization). Uniform magnetization implies $\rho_{\mathrm{tip}} = 0$, $\sigma_{\mathrm{tip}}(z' = L) = -M_z$ and

[3] Trace invariace under similarity transformation: $\mathrm{tr}(\mathbf{J}^{\mathrm{NW}}(\mathbf{k})) = \mathrm{tr}(\mathbf{J}(\mathbf{k}))$.

$\sigma_{\text{tip}}(z'=0) = +M_z$, where $z'=0$ denotes the apex of the tip above some sample. Evaluating sample stray fields in the tip's coordinate frame, the effective surface charge density is

$$\begin{aligned}\sigma_{\text{tip,eff}}(k) &= \left(M_z - M_z e^{-kL}\right) \int_{|\mathbf{r}'|\leq R} e^{i\mathbf{k}\cdot\mathbf{r}'} d^2r' = M_z \left(1 - e^{-kL}\right) \int_0^R 2\pi r' J_0(kr') dr' \\ &= M_z \frac{2\pi R}{k} J_1(kR) \left(1 - e^{-kL}\right). \end{aligned} \tag{5.22}$$

J_0 and J_1 are Bessel functions of the first kind.[4] The magnetic scalar potential at the tip plane is then

$$\phi(k, z'=0) = \frac{\sigma_{\text{tip,eff}}(k)}{2k}. \tag{5.23}$$

If we take a semi-infinite cylinder $L \to \infty$ such that $1 - e^{-kL} = 1$, and the long-wavelength limit $kR << 1$ such that $J_1(kR) \approx kR/2$, we obtain a $\mathbf{k}$-independent amplitude

$$q_{\text{tip}} = \sigma_{\text{tip,eff}}(L \to \infty, kR << 1) = M_z \frac{2\pi R}{k} J_1(kR) \approx M_z \pi R^2. \tag{5.24}$$

Since q_{tip} is constant in $\mathbf{k}$, its real-space counterpart is a delta function with magnitude $\pi R^2 M_z$. Considering this delta function, it is therefore justified to regard q_{tip} as an effective magnetic point charge in real space. This charge is the defining quantity of the monopole model, valid in the semi-infinite, long-wavelength limit. In practice, however, real nanowire tips are finite in length and radius, so the monopole model cannot hold at all spatial frequencies. Its validity depends on whether the effective surface charge density $\sigma_{\text{tip,eff}}(\mathbf{k})$ remains close to the constant value q_{tip}. Fig. 5.1 illustrates this behavior by plotting the ratio $\sigma_{\text{tip,eff}}(\mathbf{k})/q_{\text{tip}}$ for differently sized cylindrical tips. Increasing the tip length extends the flat region near unity, mainly toward longer spatial wavelengths λ, thereby enlarging the range where the monopole model is reliable, but only for larger spatial features. In contrast, the tip radius controls the roll-off at smaller λ, which sets the ultimate spatial resolution of the model.

Having established the monopole model in the limit of a very long tip, it is also useful to examine the case of a finite tip length and derive an effective dipole description. This is motivated by experimental tip characterization, where monopole and dipole contributions ideally are combined. While the monopole is obtained as a strict limit, the dipole arises from a Taylor expansion of e^{kL} for small kL. For the dipole approximation, we return to Eq. (5.22) and expand $1 - e^{-kL} \approx kL$ for $kL \ll 1$ and $J_1(kR) \approx kR/2$ for $kR \ll 1$. Fixing the total magnetic dipole moment in $\hat{\mathbf{z}}$, $m_z = \pi R^2 L M_z$, Eq. (5.22) reduces to

$$\sigma_{\text{tip,eff}}(k) \approx k m_z. \tag{5.25}$$

As we have defined in the beginning of this section, the magnetization is taken along $-\hat{z}$, so only m_z enters. In the general case, dipole moments m_x and m_y would also contribute.

[4] Since $J_1(-k) = -J_1(k) \Rightarrow J(k)/k = J(-k)/(-k) \Rightarrow \sigma_{\text{tip,eff}}(k) = \sigma_{\text{tip,eff}}(k)^*$.

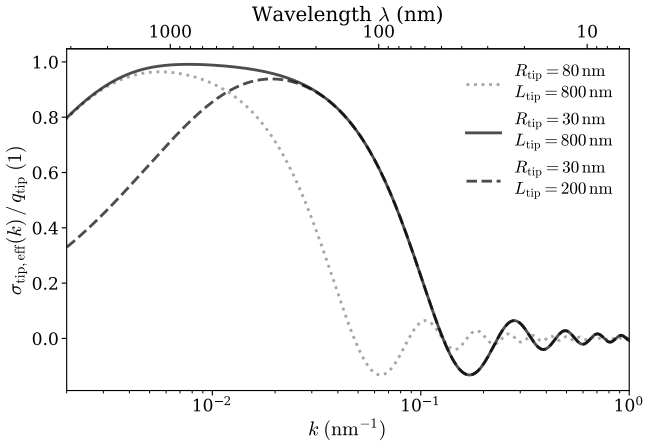

Fig. 5.1. Validity of the monopole model. A larger tip length L_{tip} extends the reliable regime toward larger spatial features, while a smaller tip radius R_{tip} improves resolution at shorter wavelengths. Dotted grey, solid black, and dashed black curves correspond to three different tip geometries.

The monopole and dipole approximations lead to scalar magnetic potentials of the form

$$\phi(k) = \frac{\sigma_{\mathrm{tip,eff}}(k)}{2k} = \begin{cases} \dfrac{q_{\mathrm{tip}}}{2k}, & \text{monopole,} \\ \dfrac{m_z}{2}, & \text{dipole.} \end{cases} \tag{5.26}$$

The monopole potential, *sourced* by q_{tip} at the tip apex ($z' = 0$), and the dipole potential, sourced by $\mathbf{m}$ at the cylinder midpoint (z'= $L_{\mathrm{tip}}/2$), are defined in the tip frame. In Fig. 5.2a we depict the tip in the sample coordinate z while retaining z' as the apex-sample separation along the tip axis. If the magnetization is not assumed to be strictly axial, then the effective monopole and dipole positions are not fixed a priori at the apex and midpoint. Instead, their heights in the sample frame, z_q and z_m, are treated as fit parameters in modelling. This choice accommodates tip tilt and non-axial magnetization while preserving the instructive monopole-dipole picture.

The dipole approximation with dipole $\sigma_{\mathrm{tip,eff}}(k) \approx km_z$ (dipole oriented along $\hat{\mathbf{z}}$) carries and extra k factor compared to the monopole approximation q_{tip}. This factor amplifies high-k components and since large k encodes short spatial wavelengths, the dipole approximation gives greater weight to fine features than the monopole model. The k factor also corresponds to an extra derivative in real space. To avert this derivative and facilitate simple MFM signal interpretation, we try to stay in the monopole regime, at the cost of spatial resolution, i.e. reduced sensitivity to small features. Experimentally, we assess the validity of the monopole model by fitting a combined monopole-dipole form to line scans across a current-carrying strip [45] and identify the dominating term. In real space, expressed in the $\{\hat{\boldsymbol{a}}_1, \hat{\boldsymbol{a}}_2, \hat{\mathbf{z}}\}$ basis, the monopole-

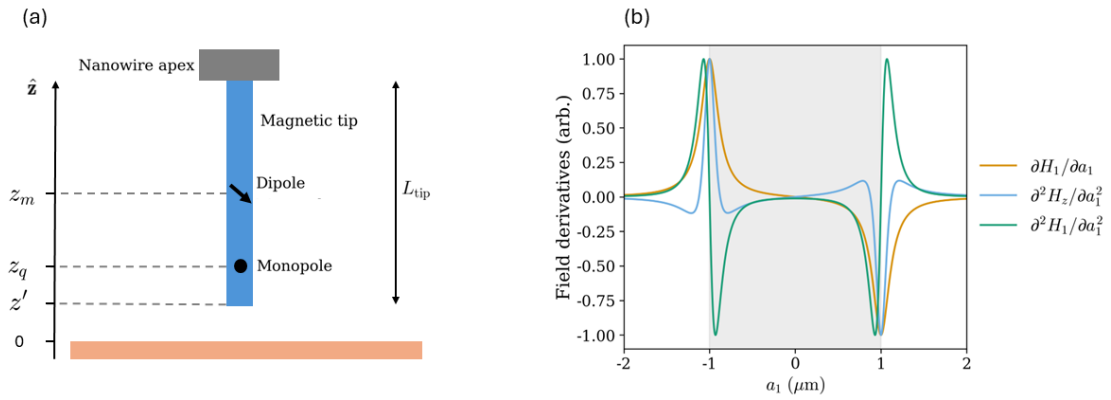

Fig. 5.2. General monopole-dipole model geometry and stray field derivatives. (a) Illustration of a magnetic tip at the free end of a cantilever nanowire. Its magnetization (not purely along $\hat{\mathbf{z}}$) is modeled as an effective monopole (magnetic charge) and a dipole at locations indicated by the black dot and arrow, respectively. (b) First and second derivatives of the Biot-Savart field above a current-carrying rectangular wire (width: 2 μm, denoted by the grey background).

dipole form yields force gradient elements

$$f_{11} = q_{\text{tip}} \frac{dH_1}{da_1} + m_1 \frac{d^2H_1}{da_1^2} + m_2 \frac{d^2H_2}{da_1^2} + m_z \frac{d^2H_z}{da_1^2}, \tag{5.27}$$

$$f_{22} = q_{\text{tip}} \frac{dH_2}{da_2} + m_1 \frac{d^2H_1}{da_2^2} + m_2 \frac{d^2H_2}{da_2^2} + m_z \frac{d^2H_z}{da_2^2}. \tag{5.28}$$

In this basis we write $\mathbf{H} = (H_1, H_2, H_z)$ and $\mathbf{m} = (m_1, m_2, m_z)$, with spherical components $m_1 = |\mathbf{m}| \sin(\theta_m) \cos(\phi_m)$, $m_2 = |\mathbf{m}| \sin(\theta_m) \sin(\phi_m)$, $m_z = |\mathbf{m}| \cos(\theta_m)$. A torque contribution may be included for completeness. However, for the approximately 20 μm long nanowires considered here, this contribution is typically negligible compared to the monopole and dipole terms.

To build intuition for the features that appear in the nanowire frequency shift signal, Fig. 5.2b shows the first and second derivatives of the stray field above a current-carrying strip. The first derivative of the in-plane field, $\partial H_1/\partial a_1$, exhibits a peak at the first wire edge and a dip at the second. The second derivative of the out-of-plane field, $\partial^2 H_z/\partial a_1^2$, shows a similar overall peak-dip structure, but with two weaker dips around the main peak and two weaker peaks around the main dip. By contrast, the second derivative of the in-plane field, $\partial^2 H_1/\partial a_1^2$, exhibits a peak followed by a dip at the first wire edge, and a dip followed by a peak at the second. In this example, the derivatives are taken along the mode 1 direction $\hat{\boldsymbol{a}}_1$, while the current is set along $\hat{\boldsymbol{a}}_2$.

5.5 Tip-Induced Perturbation and Response

Originally developed for imaging static stray fields, MFM has also been employed to probe magnetic susceptibility. In high-frequency MFM, an amplitude-modulated current applied to a write head generates magnetic fields at GHz frequencies that are down-converted into the cantilever detection band, providing access to dynamic field distributions [3, 46, 4, 47, 48]. This technique exploits the susceptibility of the tip magnetization, which responds to the oscillating field and converts it into a measurable force signal. In high-field MFM, contrast arises from field-induced magnetization of non-ferromagnetic regions, enabling phase discrimination through differences in susceptibility [49]. More recently, susceptibility contrast has been formalized as a nonlinear tip-sample interaction, where the tip field polarizes the sample and generates additional magnetic charges that feed back on the probe [50]. Here, we attempt to extend this framework to the dynamic regime, in which the interaction separates naturally into stiffness shifts and dissipative damping, both directly linked to the real and imaginary parts of the magnetic susceptibility. This framework provides the basis for interpreting the contrasts observed in our measurements on $Cr_2Ge_2Te_6$ and $EuGe_2$.

A magnetic tip's effective magnetic charge is located at height $z = z_\sigma > 0$, above a magnetic thin film sample confined to the plane $z = 0$ with a film thickness much smaller than z_σ and the relevant lateral wavelengths. The tip oscillates laterally about the equilibrium position $\mathbf{r} = \mathbf{r_0} = 0$ along the two mode directions, which we assume to be aligned with $\hat{\mathbf{x}}$ and $\hat{\mathbf{y}}$. The lateral displacement is $\delta\mathbf{r} = (\delta x, \delta y)$ with mode amplitudes A_1, A_2. Corresponding to the oscillation directions, we define the gradient $\nabla_\mathbf{r} = (\partial/\partial_x, \partial/\partial_y)$.

The oscillation of the tip results in a spatially oscillating scalar magnetic potential $\phi(\mathbf{r}, z)$. Assuming the lateral variation scale $\ell_\phi \gg |\delta\mathbf{r}(t)|$, we expand the potential at z_σ to first order:

$$\phi(\mathbf{r}, z_\sigma, t) \approx \phi(\mathbf{r}, z_\sigma) - \delta\mathbf{r}(t) \cdot \nabla_\mathbf{r}\phi(\mathbf{r}, z_\sigma). \tag{5.29}$$

Transformation to $\mathbf{k}$-space and using integration by parts yields

$$\begin{aligned}
\phi(\mathbf{k}, z_\sigma, t) &= \int \left[\phi(\mathbf{r}, z_\sigma) - \delta\mathbf{r}(t) \cdot \nabla_\mathbf{r}\phi(\mathbf{r}, z)\right] e^{-i\mathbf{k}\cdot\mathbf{r}}\, d^2\mathbf{r} \\
&= \int \phi(\mathbf{r}, z_\sigma)\, e^{-i\mathbf{k}\cdot\mathbf{r}}\, d^2\mathbf{r} - \delta\mathbf{r}(t) \cdot \int \nabla_\mathbf{r}\phi(\mathbf{r}, z_\sigma)\, e^{-i\mathbf{k}\cdot\mathbf{r}}\, d^2\mathbf{r} \\
&= \phi(\mathbf{k}, z_\sigma) - \delta\mathbf{r}(t) \cdot \left[\int \nabla_\mathbf{r}\left(\phi(\mathbf{r}, z_\sigma)\, e^{-i\mathbf{k}\cdot\mathbf{r}}\right) d^2\mathbf{r} - \int \phi(\mathbf{r}, z_\sigma)\, \nabla_\mathbf{r} e^{-i\mathbf{k}\cdot\mathbf{r}}\, d^2\mathbf{r}\right] \\
&= \phi(\mathbf{k}, z_\sigma) - \delta\mathbf{r}(t) \cdot \left[0 + i\mathbf{k} \int \phi(\mathbf{r}, z_\sigma)\, e^{-i\mathbf{k}\cdot\mathbf{r}}\, d^2\mathbf{r}\right] \\
&= \phi(\mathbf{k}, z_\sigma) - i\,(\mathbf{k} \cdot \delta\mathbf{r}(t))\, \phi(\mathbf{k}, z_\sigma) \\
&= (1 - i\,\mathbf{k} \cdot \delta\mathbf{r}(t))\, \phi(\mathbf{k}, z_\sigma).
\end{aligned}$$

Eq. (1.37) propagates $\phi(\mathbf{k}, z_\sigma, t)$ from the tip height z_σ to $z = 0$ with a vertical decay. Eq. (1.38) then maps the propagated potential to the tip's stray field at the film plane. In the frequency domain

$$\mathbf{H}_{tip}(\mathbf{k}, z = 0, \omega) = -\nabla_{(\mathbf{k},k)} \left(1 - i\,\mathbf{k} \cdot \delta\mathbf{r}(\omega)\right) \phi(\mathbf{k}, z_\sigma) e^{-kz_\sigma}. \tag{5.30}$$

The total field separates into a static and oscillating component,

$$\mathbf{H}^0_{tip}(\mathbf{k}, 0, 0) = -\nabla_{(\mathbf{k},k)} \phi(\mathbf{k}, z_\sigma) e^{-kz_\sigma} \quad , \quad \delta\mathbf{H}_{tip}(\mathbf{k}, 0, \omega) = -i\ \left(\mathbf{k} \cdot \delta\mathbf{r}(\omega)\right) \mathbf{H}^0_{tip}(\mathbf{k}, 0, 0). \tag{5.31}$$

The tip's stray field acts as an external perturbation at the film. The linear response of the film is governed by its magnetic susceptibility $\boldsymbol{\chi}_m(k, \omega)$, which relates the induced magnetization to the applied field:

$$\delta\mathbf{M}(\mathbf{k}, \omega) = \boldsymbol{\chi}_m(\mathbf{k}, \omega) \mathbf{H}_{tip}(\mathbf{k}, 0, \omega). \tag{5.32}$$

The film's Green's function $\mathbf{G}(\mathbf{k}, z, \omega)$ maps the induced magnetization at the film plane to the stray field at height $z > 0$.

$$\delta\mathbf{H}_{\text{sample}}(\mathbf{k}, z, \omega) = \mathbf{G}(\mathbf{k}, z, \omega)\, \delta\mathbf{M}(\mathbf{k}, \omega) \tag{5.33}$$

Eqs. (5.32) and (5.33), together with the tip field at the film plane from Eq. (5.30) yield the tip-sample interaction evaluated at $z = z_\sigma$:

$$\mathbf{F}(\mathbf{k}, z_\sigma, \omega) = -\mu_0\, \sigma^*_{\text{tip,eff}}(\mathbf{k}) \cdot \mathbf{G}(\mathbf{k}, z_\sigma, \omega)\, \boldsymbol{\chi}_m(\mathbf{k}, \omega) \mathbf{H}_{tip}(\mathbf{k}, 0, \omega). \tag{5.34}$$

Separating the static and dynamic contributions in Eq. (5.34) and transforming back to real space gives the static force and dynamic force at frequency ω, respectively:

$$\mathbf{F}^0(z_\sigma, 0) = -\frac{\mu_0}{4\pi^2} \int \boldsymbol{\sigma}^*_{\text{tip,eff}}(\mathbf{k}) \cdot \mathbf{G}(\mathbf{k}, z_\sigma, 0)\, \boldsymbol{\chi}_m(\mathbf{k}, 0)\, \mathbf{H}^0_{\text{tip}}(\mathbf{k}, 0, 0)\, e^{i\mathbf{k}\cdot\mathbf{r}}\, d^2k, \tag{5.35}$$

$$\delta\mathbf{F}(z_\sigma, \omega) = -\frac{\mu_0}{4\pi^2} \int \boldsymbol{\sigma}^*_{\text{tip,eff}}(\mathbf{k}) \cdot \mathbf{G}(\mathbf{k}, z_\sigma, \omega)\, \boldsymbol{\chi}_m(\mathbf{k}, \omega)\, \delta\mathbf{H}_{\text{tip}}(\mathbf{k}, 0, \omega)\, e^{i\mathbf{k}\cdot\mathbf{r}}\, d^2k. \tag{5.36}$$

As the nanowire is sensitive only to the lateral components, we define the in-plane forces (lowercase $\mathbf{f}$) through a single 2×2 operator $\mathbf{K}(\omega)$:

$$\mathbf{f}^0(\mathbf{r}_0 + \delta\mathbf{r}, \omega = 0) \approx \mathbf{f}^0(\mathbf{r}_0, \omega = 0) - \mathbf{K}_{\text{mag}}(\mathbf{r}_0, \omega = 0)\, \delta\mathbf{r}, \tag{5.37}$$

$$\delta\mathbf{f}(\omega) = -\,\mathbf{K}_{\text{mag}}(\omega)\, \delta\mathbf{r}(\omega), \tag{5.38}$$

with a lateral projection matrix $\mathbf{P}$ and the transpose of the $\mathbf{k}$ vector ($\mathbf{k}^\top$) the definition of $\mathbf{K}_{\text{mag}}$ is

$$\mathbf{K}_{\text{mag}}(\omega) = \frac{i\,\mu_0\,\mathbf{P}}{4\pi^2} \int \boldsymbol{\sigma}^*_{\text{tip,eff}}(\mathbf{k}) \mathbf{G}(\mathbf{k}, z_\sigma, \omega)\, \boldsymbol{\chi}_m(\mathbf{k}, \omega)\, \mathbf{H}^0_{\text{tip}}(\mathbf{k}, 0, 0)\, \mathbf{k}^\top\, e^{i\mathbf{k}\cdot\mathbf{r}}\, d^2k, \quad \mathbf{P} = \begin{pmatrix} 1 & 0 & 0 \\ 0 & 1 & 0 \end{pmatrix}. \tag{5.39}$$

Eqs. (5.37) and (5.38) have direct consequences for the measured mechanical response of the nanowire. We elaborate on these two expressions in turn and adjust the mechanical susceptibility of the nanowire. In Eq. (5.37), we linearize the static term about the equilibrium position, $\mathbf{r}_0$, where $\mathbf{K}_{\mathrm{mag}}(0) \equiv -\nabla_r \mathbf{f}^0\big|_{\mathbf{r}_0}$. The static in-plane force gradient (stiffness) matrix $\mathbf{K}_{\mathrm{mag}}(0)$ modifies the nanowire's intrinsic stiffness and produces frequency shifts of the modes. It does not add damping. Eq. (5.38) is a feedback relation. The tip displacement $\delta\mathbf{r}$ modulates the tip field, which drives the film. The film responds, generating a stray field that acts back on the tip. The feedback force depends on the generally complex $\mathbf{K}(\omega \neq 0)$. Both $\mathrm{Re}(\mathbf{K}_{\mathrm{mag}})$ and $\mathrm{Im}(\mathbf{K}_{\mathrm{mag}})$ contain linear combinations of $\mathrm{Re}(\chi_{\mathbf{m}})$ and $\mathrm{Im}(\chi_{\mathbf{m}})$.

Introducing $\mathbf{K}_{\mathrm{mag}}(0)$ and $\mathbf{K}(\omega)$ to the nanowire response, its mechanical susceptibility (cf. Eq. (4.4)) becomes

$$\begin{aligned}
\boldsymbol{\chi}(\omega) &= \left[-\omega^2 M\mathbf{I} - i\omega\boldsymbol{\Gamma} + \mathbf{K} + \mathbf{K}_{\mathrm{mag}}(0) + \mathbf{K}_{\mathrm{mag}}(\omega)\right]^{-1} \\
&= \left[-\omega^2 M\mathbf{I} + \left(\mathbf{K} + \mathbf{K}_{\mathrm{mag}}(0) + \mathrm{Re}\left(\mathbf{K}_{\mathrm{mag}}(\omega)\right)\right) - i\omega\left(\boldsymbol{\Gamma} - \frac{1}{\omega}\mathrm{Im}\left(\mathbf{K}_{\mathrm{mag}}(\omega)\right)\right)\right]^{-1}, \\
&= \left[-\omega^2 M\mathbf{I} + \mathbf{K}'(\omega) - i\omega\boldsymbol{\Gamma}'\right]^{-1}, \qquad (5.40)
\end{aligned}$$

where we defined the effective stiffness and damping matrices $\mathbf{K}'(\omega) = \mathbf{K} + \mathbf{K}_{\mathrm{mag}}(0) + \mathrm{Re}\left(\mathbf{K}_{\mathrm{mag}}(\omega)\right)$ and $\boldsymbol{\Gamma}' = \boldsymbol{\Gamma} - \mathrm{Im}\left(\mathbf{K}_{\mathrm{mag}}(\omega)\right)/\omega$. Operationally, each nanowire mode perturbs the film most strongly near its own resonance, so the relevant stiffness correction for mode i is evaluated at $\omega = \omega_i$. This acts as a frequency-specific but quasi-static addition to the mode's mechanical stiffness.

For magnetization confined to the 2D plane at $z = 0$, we use the half-space magnetostatic Green's function matrix [51, 52]

$$\mathbf{G}(\mathbf{k}, z) = -\tfrac{1}{2}\, e^{-kz} \begin{pmatrix} k_x^2/k & k_x k_y/k & ik_x \\ k_x k_y/k & k_y^2/k & ik_y \\ ik_x & ik_y & -k \end{pmatrix}. \qquad (5.41)$$

With this choice of $\mathbf{G}(\mathbf{k}, z)$ the magnetic interaction matrix is symmetric, $\mathbf{K}_{\mathrm{mag}}(\omega) = \mathbf{K}_{\mathrm{mag}}^{\top}(\omega)$ and therefore $\mathbf{K}'(\omega)$ is symmetric as well. Hence we may work in the eigenbasis of $\mathbf{K}'(\omega)$. Any residual mode mixing relevant for damping then arises solely from the off-diagonal elements of $\boldsymbol{\Gamma}'$. When the off-diagonal damping is small or the resonance frequencies are well separated (equivalently, high Q so splitting $\gg$ linewidth), the off-diagonal corrections to the damping are negligible as the separate-damping approximation in the inequalities (4.8) apply.

In imaging we report two scalar contrasts: a resonance frequency-based modal trace f_+ (stiffness) and a frequency-weighted but oscillation amplitude-based modal trace Γ_+ (damping). In unperturbed force gradient imaging (no magnetic feedback), f_+ equals the trace of the force gradient

matrix. Here, under negligible off-diagonal damping, we keep the same nomenclature but report the combined diagonal contributions evaluated at the two mode resonances:

$$\begin{aligned} f_+(\mathbf{r}_0) &= \left[K_{\mathrm{mag},11}(0) + \mathrm{Re}(K_{\mathrm{mag},11}(\omega_1, \mathbf{r}_0))\right] + \left[K_{\mathrm{mag},22}(0) + \mathrm{Re}(K_{\mathrm{mag},22}(\omega_2, \mathbf{r}_0))\right] \\ &\approx \frac{2k_1}{\nu_{1,\mathrm{th}}}\,\Delta\nu_1 + \frac{2k_2}{\nu_{2,\mathrm{th}}}\,\Delta\nu_2. \end{aligned} \tag{5.42}$$

The measured resonance frequency shifts at position $\mathbf{r}_0$ are denoted by $\Delta\nu_i$, while $\Delta\nu_{i,th}$ are the unperturbed resonance frequencies measured in the absence of a magnetic signal (away from the magnetic region). The static susceptibility term $\mathbf{K}_{\mathrm{mag}}(0)$ is included in f_+.

The magnetic damping contrast is obtained from the decrease of the on-resonance amplitudes. Reference amplitudes in the absence of magnetic damping are denoted $|A_i(\omega_i)|_{ref}$, intrinsic damping constants are $\Gamma_i = m\omega_i/Q_i$. At resonance,

$$\begin{aligned} \Gamma_+ &= \frac{\mathrm{Im}(K_{\mathrm{mag},11})}{\omega_1} + \frac{\mathrm{Im}(K_{\mathrm{mag},22})}{\omega_2} \\ &= \left(\frac{F(\omega_1)\,(\Gamma_1\omega_1)^{-1}}{F(\omega_1)\,\omega_1\left(\Gamma_1 + \dfrac{\mathrm{Im}(K_{\mathrm{mag},11})}{\omega_1}\right)^{-1}} - 1 \right)\Gamma_1 + \left(\frac{F(\omega_2)\,(\Gamma_2\omega_2)^{-1}}{F(\omega_2)\,\omega_2\left(\Gamma_2 + \dfrac{\mathrm{Im}(K_{\mathrm{mag},22})}{\omega_2}\right)^{-1}} - 1 \right)\Gamma_2 \\ &= \left(\frac{|A_1(\omega_1)|_{\mathrm{ref}}}{|A_1(\omega_1)|} - 1 \right)\Gamma_1 + \left(\frac{|A_2(\omega_2)|_{\mathrm{ref}}}{|A_2(\omega_2)|} - 1 \right)\Gamma_2. \end{aligned} \tag{5.43}$$

$F(\omega_i)$ denotes an actuation force at ω_i (e.g. optical or electrostatic). It makes clear that we used Eq. (2.2) in Eq. (5.43). For a position-independent drive, F cancels exactly in $|A_i(\omega_i)|_{\mathrm{ref}}/|A_i(\omega_i)|$. If the drive varies with position, normalize both amplitudes by a drive monitor (or use a local field-free reference) so the ratio is F-independent.

Assuming a tip described by the monopole model, as discussed in Appendix C.2, both the perturbing field and the effective surface charge scale with the magnetic charge q_{tip}. Consequently, the interaction matrix elements scale as $K_{\mathrm{mag},ii} \propto q_{\mathrm{tip}}^2$, so the measured contrast depends on q_{tip}^2. The imaging contrast is therefore insensitive to the sign of q_{tip} (the polarity of the tip magnetization). An independence of the contrast on the polarity was likewise reported by Stepanova et al., who emphasize that the susceptibility contribution does not change under reversal of the tip magnetization [50]. We find the same result in the imaging part of the manuscript in Fig. 12.5.

5.6 Magnetic Sensitivity Limits

A nanowire whose magnetic tip is described by the magnetic point charge q_0 has two modes. It sits in a magnetic field. The field's x-component $B(z,x,t)\hat{\mathbf{x}}$ is aligned with the direction of mode 1, $\hat{\mathbf{a}}_1$, and has a static and a dynamic term, $B(z,x,t) = B_0(z,x) + \delta B(z,x,t)$. We separately evaluate mode 1's sensitivity to the field and field gradient arising from the dynamic term and the static term, respectively. First, we consider the dynamic term $\delta B(z,x,t)$ to evaluate the field sensitivity. Mode 1 couples to $\delta B(t)$ via

$$\delta F(t) = q_{\text{tip}}\delta B(t) \Rightarrow \delta F(\nu) = q_{\text{tip}}\delta B(\nu). \tag{5.44}$$

Because the transfer function q_{tip} is constant, any force fluctuations must have their origin in field fluctuations such that we can relate the force-noise PSD, S_F, to the field-noise PSD, S_B, through

$$\langle|\delta F|^2\rangle = q_{\text{tip}}^2\langle|\delta B|^2\rangle \quad \Leftrightarrow \quad S_F = q_{\text{tip}}^2 S_B. \tag{5.45}$$

In exactly the same way that we define the smallest measurable rms force fluctuation and force sensitivity from S_F in section 2, we define the smallest measurable rms field fluctuation and field sensitivity, respectively, as

$$\delta B_{\text{rms}}(\Delta\nu_{\text{BW}}) = \sqrt{\int_{\Delta\nu_{\text{BW}}} S_B\, d\nu} = \frac{1}{q_{\text{tip}}}\sqrt{4\,k_B\,T\,\Gamma\,\Delta\nu_{\text{BW}}}, \tag{5.46}$$

$$B_{\text{min}} = \frac{\delta B_{\text{rms}}(\Delta\nu_{\text{BW}})}{\Delta\nu_{\text{BW}}}. \tag{5.47}$$

Experimentally, Eq. (5.46) helps to quantify q_{tip} (in the monopole model). For that we measure the displacement-noise PSD, S_1, to find S_F. We then evaluate $\delta B_{\text{rms}}(\Delta\nu_{\text{BW}})$ as the smallest magnetic actuation $B_{\text{act}}(\nu)$ that still permits resolving the increase in the oscillation amplitude and a well-established phase of mode 1, i.e. $|A_1|$ and $arg(A_1)$, near the resonance frequency ν_1. With that we calculate

$$q_{\text{tip}} = \left(\frac{S_F}{S_B}\right)^{1/2} = \left(\frac{S_F}{\delta B_{\text{rms}}(\Delta\nu_{\text{BW}})/\Delta\omega_{\text{BW}}}\right)^{1/2} = S_F^{1/2}\,\frac{\Delta\omega_{\text{BW}}^{1/2}}{\delta B_{\text{rms}}(\Delta\nu_{\text{BW}})^{1/2}} \tag{5.48}$$

Second, we consider the gradient arising from the expansion of the static field term, $B_{11} = \partial B_0(z,x)/\partial x$, to evaluate the magnetic field gradient sensitivity of mode 1. We proceed by relating B_{11} to the force gradient f_{11} which relates to frequency shift $\Delta\nu_1$. Fortunately for us, an expression analogue to $f_{11,min}$ relating phase-noise to frequency-noise is given by Albrecht et al. (1991) [53]. In our notation,

$$f_{11,\text{rms}}(\Delta\omega_{\text{BW}}) = \frac{\sqrt{2}}{|A_1|}\sqrt{S_F(\omega)\Delta\omega_{\text{BW}}} = \frac{\sqrt{2}}{|A_1|}\sqrt{\frac{4k_BTm\omega_1\Delta\omega_{\text{BW}}}{Q}}. \tag{5.49}$$

The smallest measurable rms force gradient $f_{11,\text{rms}}$ depends inversely on the actuation amplitude $|A_1|$. Increasing $|A_1|$ results allows to measure a lower force gradient. For the corresponding

smallest measurable rms magnetic field gradient, $B_{11,\mathrm{rms}}$, and field gradient sensitivity $B_{11,\mathrm{min}}$ we multiply Eq. (5.49) by q_{tip} :

$$B_{11,\mathrm{rms}}(\Delta\omega_{\mathrm{BW}}) = \frac{\sqrt{2}}{q_{\mathrm{tip}}|A_1|}\sqrt{S_F(\omega)\Delta\omega_{\mathrm{BW}}} = \frac{\sqrt{2}}{q_{\mathrm{tip}}|A_1|}\sqrt{\frac{4k_BTm\omega_1\Delta\omega_{\mathrm{BW}}}{Q}}. \tag{5.50}$$

The sensitivity limits to magnetic field and field gradient are quantified by B_{min} and $B_{11\,\mathrm{min}}$, respectively. The square of both quantities inherits a scaling with $\Gamma = m\omega_1/Q$ from S_F. While Q empirically decreases approximately with the thickness b of a nanowire, the numerator of Γ reflects a geometric scaling factor b^3/L. Combined, they yield an overall geometric scaling factor of b^2/L. Thus, longer and thinner nanowires improve sensitivity to both field and field gradient.

Both sensitivities scale inversely with the magnetic point charge q_{tip}, which in turn depends on the saturation magnetization of the tip material. A larger q_{tip} improves performance, so the saturation magnetization should be as high as possible. $B_{11,\mathrm{min}}$ is also inversely proportional to $|A_1|$, so increasing the oscillation amplitude enhances gradient sensitivity. $|A_1|$ can be increased up to the point where geometric non-linearity set in, according to the Euler-Bernoulli assumption in Eq. (3.10). Longer nanowires can be driven at larger $|A_1|$ before reaching this limit. In practice, higher oscillation amplitudes require larger actuation power, which may introduce additional dissipation and thereby degrade sensitivity. Large $|A_1|$ also reduces spatial resolution by effectively enlarging the magnetic tip diameter, introducing a trade-off between sensitivity and resolution.

Microscope and Nanowire

Our NW-MFM scanning probe system relies on a calibrated, custom-built setup that preserves the nanowire's intrinsic sensitivity. In this part, we document the setup architecture, the preparation and characterization of the nanowire and magnetic tip, and the procedures for handling and mounting samples. By calibration we mean, in particular, establishing the detection and actuation transfer functions, determining the nanowire's displacement scale, mode orientations and quality factors, quantifying the magnetic-field or force gradient sensitivity, and verifying the tip model (e.g. effective monopole character and its parameters). Together, the experimental chapters provide the practical basis for the MFM imaging that we will discuss in the next part of the manuscript.

6. Microscope Setup

We describe the scanning module, the cryogenic vacuum environment, and the optical readout used to detect the nanowire's two flexural modes. Emphasis is on mechanical stability, alignment of the nanowire relative to the sample plane, and control of magnetic field and temperature.

6.1 Scanning Module and Vacuum Chamber

Two stacks of piezo-electric positioners and a confocal objective fixed to a titanium frame constitute the scanning module of our scanning force microscope. For the module we adopt a Cartesian coordinate system, where imaging takes place in the xy-plane, the objective's optical axis lies along $\hat{\mathbf{x}}$, and nanowires extend in -$\hat{\mathbf{z}}$.

The bottom stack of the module shown in Fig. 6.1 holds a heater-equipped sample stage. Stepper units[1] allow coarse navigation in $\hat{\mathbf{x}}$, $\hat{\mathbf{y}}$, and $\hat{\mathbf{z}}$. Fine positioning in $\hat{\mathbf{z}}$ is achieved by applying an offset to the z-stepper. An xy-scanning unit[2] ensures fine positioning in the xy-plane and

[1] ANPx300, Attocube
[2] ANSxy100, Attocube

allows to image an area of 10 μm $\times$ 10 μm (T=4.2 K). The bottom stepper units are connected with copper wiring that provides direct thermal contact to room temperature. When cooling the probe to 4.2 K, this thermal link establishes a gradient such that the bottom stack reaches a base temperature of about 12 K. By adding additional copper wires anchored to the 4.2 K bath, the sample stage temperature can be reduced further to 4.3 K.

The top stack has the same kind of stepper units as the bottom stack but uses an xyz-scanner unit[3] with a 30 μm $\times$ 30 μm $\times$ 15 μm range for fine positioning. It carries a chip with clamped nanowires whose longitudinal axes are aligned approximately normal to the sample surface. Together, the two stacks enable precise positioning of any nanowire within the objective's focal spot and of any suitable sample directly beneath that nanowire's tip. As for the bottom stepper units, the top stack is also connected to copper wiring that provides direct thermal contact to room temperature. This leads to an equilibrium temperature of about 12 K, which is also the temperature of the nanowires mounted on the top stack. Since adding cooling wires to the top stack introduces vibrations, we avoid doing so and accept this operating temperature. To suppress external vibration, the scanning module hangs from four copper springs inside a stainless-steel chamber. The chamber is evacuated to 10^{-6} mbar at room temperature, providing a clean, mechanically quiet environment for sensitive force measurements. Vacuum is maintained by a turbo-molecular pump and optionally by an ion pump, which does not cause any vibration. The chamber base is sealed on a copper disc with an indium gasket. The copper serves as a good thermal interface to the outside. Optical and electrical feedthroughs at the top of the chamber allow to detect and stimulate the nanowire displacement. Electrical feedthroughs allow to set voltages and send currents in and into the vacuum chamber, and to control[4] the piezo-electric positioners. A 16-bit analog output card[5] with BNC output panel[6] supplies voltages to the positioners. The outputs are controlled with LabView.

6.2 Sample Stage with Temperature Control

Sitting atop the bottom piezo-electric stack is a compact sample stage with resistive heater that permits fine temperature control [7] of the sample from cryogenic temperatures to at least 130 K (with the superconducting magnet operable). It comprises a heater element, a temperature sensor [8], and a machined MACOR (glass-ceramics) spacer that thermally isolates the stage from the stack. The heater element consists of a single strand of constantan wire (resistance: 50 Ω, 28.78 Ω/m, D = 0.15mm, Grade 1) twisted onto itself to cancel static Biot-Savart fields and

[3] ANSxyz100lr
[4] ANM150, ANM 200, ANM 300
[5] PXI-6733 National Instruments
[6] BNC-2100, National Instruments
[7] 325 Temperature controller, LakeShore
[8] Cernox, LakeShore; sensor model: CX-1050-SD-HT-1.4L; temperature range: 1.4 K to 325 K

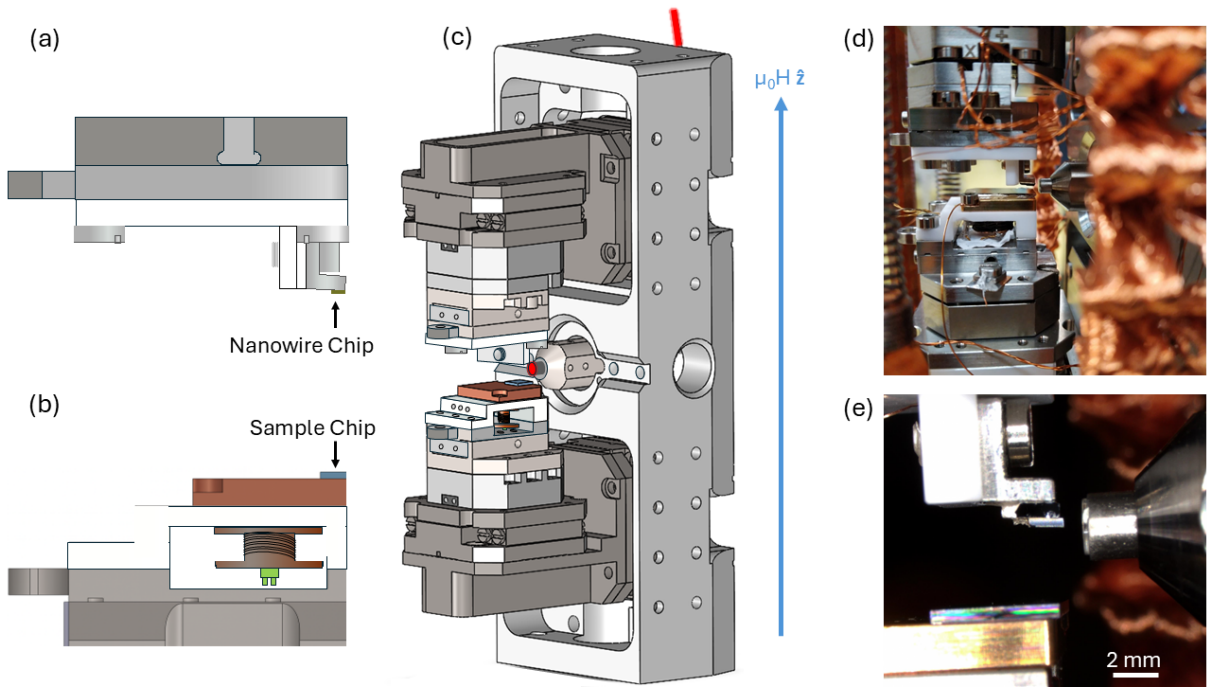

Fig. 6.1. Scanning module. (a) Nanowire holder with MACOR spacer in white, and (b) sample stage with integrated heater spool and temperature sensor (green). (c) Holder and stage are mounted on stacks of piezoelectric positioners held by a titanium frame with objective (false-colored red lens). The blue arrow marks the applicable direction for a uniform field. (d, e) Optical images of the scanning module with nanowire holder, sample stage and objective.

wound around a machined copper spool. A calibrated temperature sensor sits in a cavity within that same spool submersed in cryo-compatible thermal grease[9] and is read out via four-point measurement to eliminate lead-resistance errors. The spool is embedded in a circular bore of MACOR spacer. A 13 × 13 mm oxygen-free copper sample plate can be screwed tightly onto the top of the MACOR spacer, allowing the spool to protrude slightly at room temperature to account for contraction during cool down. A thin smear ofthermal grease fills gaps, ensuring thermal contact between the spool and sample plate. A flexible oxygen-free copper braid thermally anchors the sample plate directly to the 4.2 K helium bath, providing efficient thermalization. This braid was used in most experiments but is not strictly required for standard operation; it hinders accurate temperature readout by introducing a temperature offset between the sensor and the sample plate. In recent experiments, the braid has been replaced by a thin copper wire. The sample stage has been tested to warm the sample from the 4.3 K helium bath base temperature up to 120 K with the superconducting magnet in operation. When the inner chamber is cooled with liquid nitrogen, the stage provides controlled heating from 77 K, though the magnet must

[9] Apiezon N

remain off.

6.3 Cryostat and External Magnetic Field

For experiments requiring cryogenic temperatures or strong magnetic fields, the *in vacuo* scanning module operates inside a dewar-based cryostat with two concentric, vacuum-insulated chambers. The inner chamber is typically filled with liquid helium, cooling the sample stage to $T \approx 4.3$ K and keeping a superconducting solenoid below its critical temperature, which enables the application of a uniform magnetic field $\mathbf{B} = \mu_0 H \hat{\mathbf{z}}$ (see blue arrow in Fig. 6.1b) up to 8 T. The outer chamber is filled with liquid nitrogen to reduce helium boil-off. For vibration-isolation, the cryostat rests on a pressurized-air table.

6.4 Optical Path and Measurement Hardware

Light for detection[10] (1550 nm) and light for optical actuation [11] (1625 nm) propagate through SMF-28e single-mode fibers via AF/APC connectors. Each diode output is attenuated by fixed inline fiber attenuators and polarization-aligned with its own three-paddle polarizer[12]. Polarization increases detection and optical driving efficiencies [54]. The 1625 nm beam additionally passes an acousto-optic modulator [13] (AOM).

The two prepared beams are merged in a wavelength-division multiplexer. The combined beam enters a fused-fiber 95:5 coupler[14], which diverts 5 % to a side-view confocal objective (see Fig. 7.1a for arrangement). Reflections from the cleaved fiber facet inside the objective and from the nanowire ($\approx$ 5 %), picked up by the objective, interfer. The interference signal itself propagates through the coupler, and 95 % passes through a narrowband 1550 nm band-pass filter ($>$ 35 dB rejection at 1625 nm) before being detected by a photoreceiver.

The side-view confocal objective is built around a precision-machined titanium body shown in Fig. 7.1b that houses, in sequence, the cleaved end of an SMF-28e fiber inside a glass ferrule for centering, a collimating lens, and a focusing lens. First, the collimating lens (Thorlabs 354430-C, NA 0.16, f = 5 mm, CA = 1.6 mm) is glued into the ferrule with TorrSeal adhesive. Next, the bare fiber is inserted and axially adjusted until its output is optimally collimated, at which point the fiber is secured in place. Finally, the focusing lens (Thorlabs 354140-C, NA 0.58, f = 1.45

[10] Laser for detection: DFB pro BFY, TOPTICA; digital laser controller: DLC Pro, TOPTICA Photonics

[11] Laser for actuation: 1625LD-1-0-0-1, AeroDIODE; current source: LDX-3620, ILX LIghtwave; temperature controller: TED200C, THORLABS

[12] FPC560, Thorlabs

[13] Fiber-Q S/N 02291536, Gooch & Housego

[14] SMC-1550-2x2-5/95-3.0x45-SMF28e-S-1-S, CSRayzer

mm, CA = 1.6 mm) is added and also fixed with TorrSeal. The objective is then clamped onto the titanium frame of the scanning module.

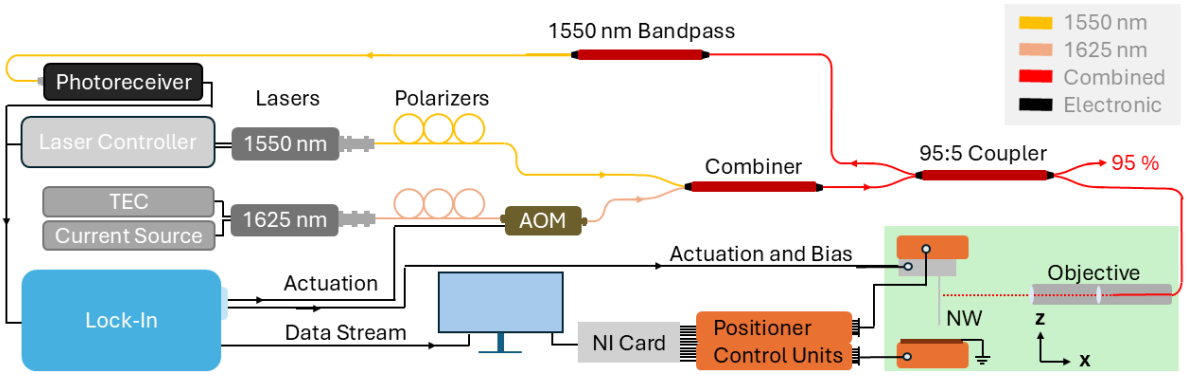

Fig. 6.2. Optical path and connected hardware. Two photo diodes emit laser light at $\lambda_1 = 1550$ nm and $\lambda_2 = 1625$ nm for detection and actuation of the nanowire motion, respectively. The light can be tuned with thermoelectric coolers (TEC) and three-paddle polarizers. The combined light is sent through a 95:5 couler to the scanning module (green background) from Fig. 6.1. The isolated interference contrast of the λ_1 light is sent to a photoreceiver, rendering the measurement signal. A lock-in with two phase-locked loops is used for feedback generation and data processing. Feedback actuation via optical and electrical channel. The optical actuation relies on an acousto-optic modulator (AOM).

The photoreceiver converts the interference signal into a voltage encoding the projection of the nanowire's displacement along the optical axis. This voltage is analyzed by a digital lock-in amplifier[15]. We use the lock-in to record displacement-noise PSDs, which reveal the Lorentzian peaks of the nanowire's fundamental flexural modes and allow us to extract resonance frequencies and quality factors, projection angle, and, given the nanowire's temperature, also its mass. The lock-in also provides actuation signals, enabling us to drive the modes and perform frequency sweeps. By recording the amplitude $|a_\mathrm{p}|$ and phase $\arg a_\mathrm{p}$ during these sweeps, we again identify the resonances and define suitable phase setpoints. Once the resonance conditions are established, two phase-locked loops (PLLs) are engaged to continuously track the resonance frequency and oscillation amplitude of both modes. All lock-in outputs are recorded in LabVIEW to synchronize data acquisition with the scan position, while the same signals are simultaneously streamed via the lock-in's browser interface.

[15] UHF Lock-In Amplifier (600 MHz, 1.8 GSa/s), Zurich Instruments

7. Data Acquisition

In theory, the nanowire dynamics are governed by the mechanical susceptibility $\boldsymbol{\chi}(\omega)$, which acts as the system's response function mapping any applied force to a projected displacement $a_{\mathrm{p}}(\omega)$. Experimentally, we are interested in $a_{\mathrm{p}}(\omega)$, since it contains the information about resonance frequencies and oscillation amplitudes. However, considering the microscope setup described in the previous chapter, $a_{\mathrm{p}}(\omega)$ is not observed directly. Instead, it is converted into a voltage through the optical detection path (see Fig. 6.2). Any deliberate actuation, in turn, is introduced as an input voltage signal from the lock-in that is converted into a force through the actuation path. The two conversions are described by transfer functions: the detection transfer function G_{det}, which maps a_{p} to the photoreceiver voltage V_{det}, and the actuation transfer function G_{act}, which maps an applied actuation signal V_{act} to a force acting on the nanowire. Together with the projected susceptibility χ_p[1], they define the acquisition chain,

$$V_{\mathrm{det}}(\omega) = G_{\mathrm{det}}(\omega)\, a_p(\omega) = G_{\mathrm{det}}(\omega)\, \chi_p\, F(\omega) = G_{\mathrm{det}}(\omega)\, \chi_p\, G_{\mathrm{act}}(\omega)\, V_{\mathrm{act}}(\omega). \tag{7.1}$$

In NW-MFM, data acquisition is typically performed using phase-locked loops (PLLs), which actuate and track the nanowire modes during imaging. Stable phase setpoints in the PLLs are essential. This requires that the detection and actuation transfer functions remain flat in phase to ensure reliable frequency tracking. Moreover, accurate relative amplitude readout during PLL operation demands that the transfer functions remain flat in magnitude, so that oscillation amplitudes are not distorted. In the following, we therefore analyze the detection and actuation paths of our microscope in detail and describe how their transfer functions are characterized.

7.1 Detection

To determine the detection transfer function G_{det}, we consider the interferometer formed by the cleaved fiber facet and the nanowire sidewall. This approach has been successfully applied to Si nanowire displacement detection, where polarization optimization was shown to enhance fringe visibility and displacement sensitivity [54]. Both the fiber facet and the nanowire sidewall act as weak reflectors characterized by power reflectivities R_{core} and R_{NW} with $R_{\mathrm{core}}, R_{\mathrm{NW}} \ll 1$. An incident field E_{inc} is partially reflected at the fiber facet interface producing a reference field

$$\mathbf{E}_{\mathrm{ref}} = \sqrt{R_{\mathrm{core}}}\mathbf{E}_{\mathrm{inc}}. \tag{7.2}$$

[1] χ_p is itself a transfer function.

The transmitted portion of the field propagates beyond the fiber facet, where a small fraction scatters off the nanowire sidewall and couples back into the fiber. This component picks up two Fresnel transmission factors of $\sqrt{1-R_{\mathrm{core}}}$, the nanowire's amplitude reflectivity $\sqrt{R_{\mathrm{NW}}}$, and a round-trip phase delay of $4\pi u/\lambda$, where u is the displacement along the optical axis. The corresponding return field is

$$\mathbf{E}_{\mathrm{NW}} = E_{\mathrm{inc}}(1-R_{\mathrm{core}})\sqrt{R_{\mathrm{NW}}}\mathbf{e}^{i4\pi u/\lambda}. \tag{7.3}$$

Because these two fields recombine in the fiber, the detected optical power is

$$P_{\mathrm{det}} = \left|\mathbf{E}_{\mathrm{ref}} + \mathbf{E}_{\mathrm{NW}}\right|^2 = |\mathbf{E}_{\mathrm{ref}}|^2 + |\mathbf{E}_{\mathrm{NW}}|^2 + 2\mathrm{Re}(\mathbf{E}_{\mathrm{ref}}\mathbf{E}^*_{\mathrm{NW}}). \tag{7.4}$$

Neglecting all terms with second-order reflectivity, i.e. those proportional to $R_{\mathrm{core}}R_{\mathrm{NW}}$, R^2_{core}, and R^2_{NW}, this reduces to

$$P_{\mathrm{det}} \approx \mathbf{E}^2_{\mathrm{inc}}\Big[R_{\mathrm{core}} + R_{\mathrm{NW}} + 2\sqrt{R_{\mathrm{core}}R_{\mathrm{NW}}}\cos\big(\frac{4\pi u}{\lambda}\big)\Big]. \tag{7.5}$$

The cosine term in Eq. (7.5) produces alternating minima and maxima, i.e. interference fringes spaced by $\lambda/2$ shown in Fig. 7.1c and d. In terms of the detected voltage, these extrema define V_{min} and V_{max}. Defining the average power and the fringe visibility, respectively, as

$$P_{\mathrm{avg}} = \mathbf{E}^2_{\mathrm{inc}}\,(R_{\mathrm{core}} + R_{\mathrm{NW}}), \quad \text{and} \quad C = 2\sqrt{R_{\mathrm{core}}R_{\mathrm{NW}}}/(R_{\mathrm{core}} + R_{\mathrm{NW}}) \tag{7.6}$$

gives

$$P_{\mathrm{det}} = P_{\mathrm{avg}}(1 + C\cos\left(\frac{4\pi u}{\lambda}\right)). \tag{7.7}$$

A photoreceiver with gain G_{PD} converts this into a voltage,

$$V_{\mathrm{det}}(u) = G_{\mathrm{PD}}\,P_{\mathrm{det}}(u) = V_{\mathrm{avg}}\big[1 + C\cos\big(\tfrac{4\pi u}{\lambda}\big)\big], \quad V_{\mathrm{avg}} = G_{\mathrm{PD}}\,P_{\mathrm{avg}}. \tag{7.8}$$

For small oscillations $\delta u \ll \lambda/4$, we Taylor expand V_{det} about a working point u_{WP},

$$V_{\mathrm{det}}(u_{\mathrm{WP}} + \delta u) \approx V_{\mathrm{det}}(u_{\mathrm{WP}}) + V'(u_{\mathrm{WP}})\,\delta u + \tfrac{1}{2}\,V''(u_{\mathrm{WP}})\,\delta u^2. \tag{7.9}$$

To eliminate the quadratic term and enforce a purely linear response $\delta V_{\mathrm{det}} \propto \delta u$, we choose u_{WP} at any fringe-inflection point, i.e. where $V''(u_{\mathrm{WP}}) = 0$. The remaining slope

$$G_{\mathrm{det}} = \frac{dV_{\mathrm{det}}}{du}\Big|_{u_{\mathrm{WP}}} = \pm\frac{4\pi}{\lambda}\,C\,V_{\mathrm{avg}} = \pm\frac{2\pi}{\lambda}\,C\,\big(V_{\mathrm{max}} - V_{\mathrm{min}}\big). \tag{7.10}$$

The photoreceiver transfer function, G_{PD}, can be considered frequency-independent within the relevant measurement band. As a result, the overall detection gain G_{det} acts as a constant voltage-displacement conversion factor typically on the order of 1 mV/nm. This scaling does not affect the determination of resonance frequencies or relative oscillation amplitudes. Any phase lag introduced by the photoreceiver electronics manifests only as a fixed phase offset in the detected signal.

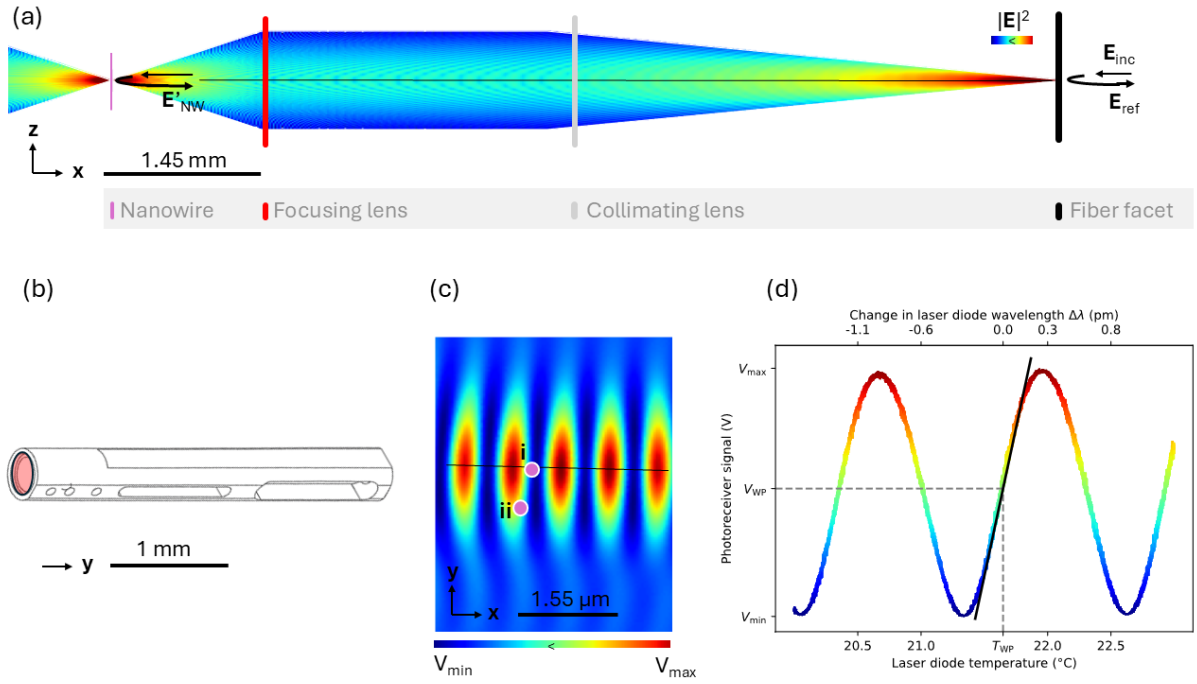

Fig. 7.1. Interferometric detection between the fiber facet and the nanowire sidewall. (a) Optical sketch with a collimated beam exiting the fiber facet and focused onto the nanowire sidewall. A small fraction of the transmitted light scatters from the sidewall and recouples into the fiber, where it interferes with the reference reflection from the cleaved facet. (b) Mechanical assembly with titanium housing that holds the collimating and focusing lenses together with the cleaved fiber tip. (c) Photoreceiver signal with interference fringes spaced by $\lambda/2 = 775$ nm. Two purple dots mark two possible fringe working points u_{WP}: (i) on the optical axis $\hat{\mathbf{x}}$, which maximizes $\partial V/\partial u$ (G_{det}); and (ii) off-axis, which tilts the gradient to detect a mode with direction orthogonal to $\hat{\mathbf{x}}$ when necessary. In practice we select nanowires whose modes never lie purely along $\hat{\mathbf{x}}$, so we always position them at a working point analogous to (i). (d) Working-point adjustment: instead of repositioning the nanowire to counteract drifts, we tune the laser-diode temperature to shift the interferometer phase, restore u_{WP}, and re-establish G_{det} for voltage-to-displacement calibration, provided the nanowire remains on the optical axis. Any off-axis drift still requires repositioning. Minimum and maximum detected voltages yield $G_{\mathrm{det}} \approx 876\ \mu\mathrm{V/nm}$.

7.2 Actuation

In MFM, where the nanowire is typically driven in a PLL, reliable frequency tracking requires not only a stable detection path but also a well-defined actuation path. The drive originates from the lock-in amplifier, which provides a voltage V_{act} at the actuation input. This voltage is converted via the actuation transfer function G_{act} into an oscillatory force acting on the nanowire:

$$F = G_{\mathrm{act}}\, V_{\mathrm{act}}. \tag{7.11}$$

Eq. (7.11) is embedded in the full acquisition chain given in Eq. (7.1). The specific mechanism behind this force depends on the actuation scheme. Possible realizations include piezoelectric excitation of the substrate, dielectric forces between electrodes and the nanowire, radiation-pressure or gradient forces from the detection laser, or magnetic forces generated by the Biot–Savart field of an alternating current in a nearby conductor. In each case, the functional form of G_{act} differs, but the general description remains valid. Stable PLL operation requires that G_{act} remains spectrally flat over the frequency band of interest so that the applied voltage translates into a force with well-defined amplitude and phase.

We employ three practical actuation schemes. Optical actuation is achieved by modulating the intensity of a 1625 nm laser and sending it through the same objective as the detection beam. By focusing the detection beam on the nanowire midpoint, the longer-wavelength actuation beam is slightly defocused. Positioning at the midpoint reduces detection efficiency but increases the drive, which is strongest near the clamped base. Optical actuation works best when imaging close to the sample edge. Beyond the edge, the diverging beam is clipped by the bulk sample, reducing efficiency and eventually suppressing the actuation. Again, positioning at the midpoint provides a bit more range in this regard. Because the optical force is directional, one of the two flexural modes is typically driven more strongly than the other.

Electrostatic actuation is realized by applying a sinusoidal voltage to the nanowire chip and holder while keeping the sample to be imaged grounded, whenever possible using a thin gold coating to ensure good conductivity. In this configuration the actuation is stable as long as the region of interest is not too close to large topographic steps. At the sample edge, sign changes in the electric field lead to a phase flip of the actuation voltage, which degrades performance. Imaging a few microns away from the edge remains reliable.

Magnetic actuation is used mainly to characterize the nanowire's magnetic tip and its field sensitivity. An alternating current passed through a lithographically defined wire produces a well-defined stray field. When the nanowire is positioned above such a wire of rectangular cross section, the stray field distribution is precisely known. Frequency sweeps at defined drive amplitudes then allow us to benchmark the ultimate stray field sensitivity.

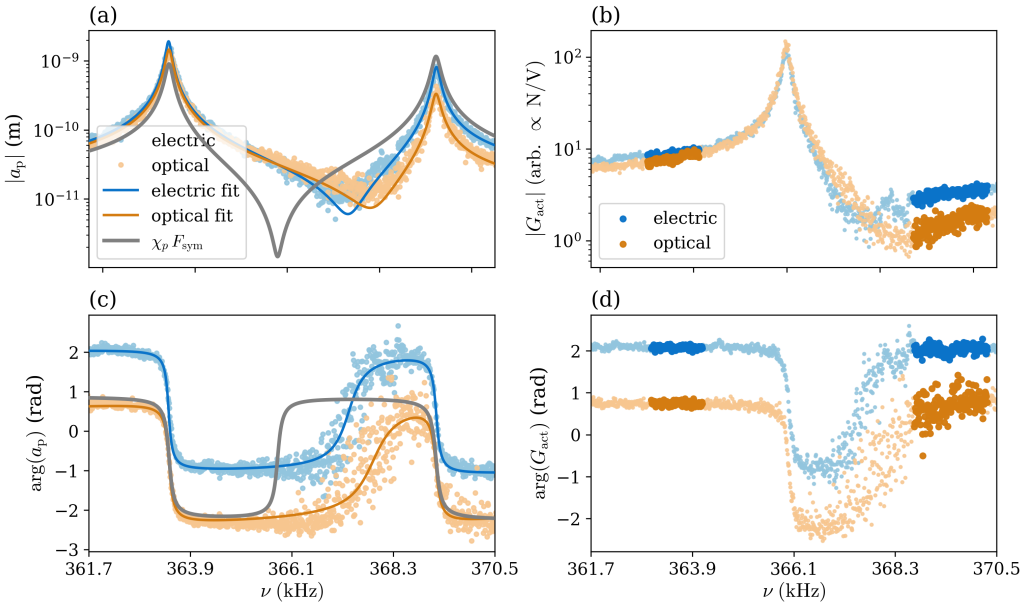

Fig. 7.2. Actuation transfer function for electrostatic (blue) and optical (orange) actuation. (a,c) Measured frequency-response (magnitude and phase) fitted according to Eq. (4.15). For a fixed detection angle α, the fitted actuation directionalities are parametrized by $\beta_{\rm el} \approx 22°$ and $\beta_{\rm opt} \approx 15°$ with respect to the softer mode 1. The gray curve is the displacement amplitude predicted from the displacement-noise PSD S_p (see Fig. 4.3) via $a_p = \chi_p F_{\rm sym}$, assuming a constant symmetric drive $F_{\rm sym}$. (b,d) Actuation transfer functions extracted via Eq. (7.13) using the S_p-based susceptibility χ_p. Bold markers highlight the near-resonance regions.

To determine the actuation transfer function we combine an analysis of the displacement-noise PSD, S_{meas}, with driven-response measurements [55, 56]. We first take a S_{meas} and fit it to extract the mechanical parameters of the nanowire, including effective mass, resonance frequencies, quality factors, and projection angle. Using these parameters we reconstruct the projected susceptibility χ_p according to the damped harmonic oscillator model. In a second step we perform driven-response measurements by applying a sinusoidal actuation and recording response curves. The driven response a_p, with magnitude $|a_p|$ and phase $\arg(a_p)$, is described by

$$a_p(\omega) = \chi_p(\omega)\, G_{\rm act}(\omega)\, V_{\rm act}(\omega). \tag{7.12}$$

Eq. (7.12) is also embedded in Eq. (7.1). Normalizing by the applied actuation voltage yields the measured actuation response

$$G_{\rm meas}(\omega) = \frac{a_p(\omega)}{V_{\rm act}(\omega)} = \chi_p(\omega)\, G_{\rm act}(\omega). \tag{7.13}$$

The response curves therefore provide G_{meas} up to some V_{act} relicts. By dividing G_{meas} by χ_{p}, we isolate the actuation transfer function itself, with magnitude $|G_{\mathrm{act}}|$ and phase $\arg(G_{\mathrm{act}})$.

Now we apply this procedure to the electrical and optical actuation methods. The starting point is S_{meas} shown in Fig. 4.3a, from which we extract the nanowire's mechanical parameters and reconstruct $\chi_p(\omega)$ (Fig. 4.3b, c) according to the damped harmonic oscillator model. Assuming constant and symmetric forcing F_{sym}, we find the theoretical $a_p(F_{\mathrm{sym}})$. It is in plotted in grey in terms of magnitude and phase in Fig. 4.3b, c, and corresponds to a constant G_{act}. In the second step we record the response measurements. Experimental magnitude and phases of a_p are shown in Fig. 7.2a for the electric and optical actuation. From these data we form G_{meas}. Division by χ_p yields G_{act} as shown in Fig. 7.2b, d. $G_{\mathrm{act}}(\omega)$ is flat in both magnitude and phase in the vicinity of the two resonance frequencies, ensuring reliable PLL-based frequency tracking and undistorted relative amplitude readout. To probe $G_{\mathrm{act}}(\omega)$ over a broader frequency range, we will shift the nanowire's resonances (e.g. by electrostatic tuning) and repeat the response sweeps; until such detuning tests are performed, we provisionally assume that $G_{\mathrm{act}}(\omega)$ remains flat over a wider frequency window.

8. Characterization of Magnet-Tipped Nanowires

At the heart of NW-MFM is the nanowire. By *nanowire* we do not mean a conventional metallic wire on a spool, nor a flat wire patterned in a film. We mean a cantilevered, high aspect ratio Si beam with very low mass and two compliant in-plane flexural modes.

This chapter describes the preparation of the nanowire chip allowing for electrical biasing and turning the nanowire into a magnetic probe using cobalt (Co). We verify the tip magnetization and check the tip model (effective monopole character and parameters). We then measure resonance frequencies, quality factors, mode orientations, and effective mass. These numbers set the displacement scale, define the projection axes for force gradients, and determine the ultimate magnetic sensitivity of NW-MFM.

8.1 Nanowire Device Preparation

Si nanowires with lengths of $L \approx 20$ μm and diameters $D = 100$–150 nm (NW 1: 150 nm, NW 2: 110 nm) were supplied by the Budakian group at the University of Waterloo, Canada. They are grown by chemical vapor deposition (CVD) using gold catalysts on n-type Si (111) substrates within lithographically defined regions. Patterned weak links allow these regions to be cleaved into chips bearing one to three rows of nanowires, spaced by approximately 40 μm and positioned within 7 μm of the chip edge to permit unobstructed optical access [57].

A cleaved chip is fixed to an L-shaped titanium mount using Araldite. Electrical contact between chip and mount is established with silver paint[1]. The nanowires are then functionalized by Co deposition. The deposition will be discussed in Sec. 8.3. Afterwards, the mount is screwed to a spacer that, during the imaging described in the MFM imaging part, was fabricated from titanium. In the current design, this spacer has been replaced by MACOR, which electrically isolates the mount with the nanowires from the rest of the holder and the piezoelectric positioner stack. In this configuration, a single lead connected to the mount turns the entire mount (with nanowire chip) into a gate electrode, enabling some control of the tip potential. The spacer itself is attached to a titanium slider. Together these three parts (mount, spacer, and slider) constitute the complete nanowire holder shown in Fig. 6.1b. The holder slides into a matching platform at the piezoelectric positioner stack and is fixed.

8.2 Electrical Biasing and Actuation

A potential applied to the nanowire mount can be used to actuate the nanowire, as already demonstrated in Fig. 7.2, and it can likewise be used to apply a voltage bias V_b. The applied voltage generally is

$$V(t) = V_b + V_0 \cos(\omega t). \tag{8.1}$$

In the imaging configuration, the biased nanowire chip faces the grounded sample surface, forming a capacitor. Variations in the curvature of the capacitor's electrostatic energy modify the nanowire's effective spring constants and thereby shift its resonance frequencies. These variations are governed by the potential difference between the nanowire chip and the sample surface, which consists of the applied bias V_b, the oscillating voltage $V_0 \cos(\omega t)$, and the contact potential difference V_{CPD}. V_0 provides the periodic actuation of the nanowire, while the static contributions V_b and V_{CPD} tune the resonance frequencies through tension-induced stiffening. As discussed in Sec. E, a more general formulation may include additional terms such as magneto-electric contributions V_{ME} from the sample, although they are not relevant in this section.

[1] ACHESON Silver DAG 1415

Unlike in the conventional cantilever geometry, where the beam oscillates along $\hat{\mathbf{z}}$ and only the second derivative of the capacitance along $\hat{\mathbf{z}}$ contributes to electrostatic stiffening, in the nanowire pendulum geometry the oscillations are lateral, so derivatives of the potential along $\hat{\mathbf{x}}$ or $\hat{\mathbf{y}}$ also enter. The corresponding expressions for the electrostatic spring-constant shifts in these two geometries are derived in appendix E (see Eqs. (E.2) and (E.3)).

To test the electrical biasing and actuation, we performed measurements with the nanowire positioned tens of microns above a gold-coated sample surface held at ground. In this configuration, only V_b and V_{CPD} contribute, with V_0 fixed at 50 mV. The results are shown in Fig. 8.1. Selected response curves of amplitude and phase are displayed in panels (a) and (b). The amplitude $|a_{\mathrm{p}}|$ curves demonstrate that, as $|V_b|$ increases, the resonance frequencies shift upward due to electrostatic attraction that stiffens the nanowire modes. This trend is made clearer in Fig. 8.1d, where the resonance-frequency shifts $\Delta\nu_i(V_b)$ are plotted against V_b. The data follow a quadratic dependence, consistent with electrostatic tension-induced stiffening. Quadratic fits (red) to these parabolas yield the tuning coefficients $c_1 \approx 21.5\ \mathrm{Hz\,V^{-2}}$ and $c_2 \approx 22.1\ \mathrm{Hz\,V^{-2}}$, as well as the contact potential difference $V_{\mathrm{CPD}} \approx -1.0$ V (relative difference between modes: 6 %). The resonance frequencies at $V_b = V_{\mathrm{CPD}}$ correspond to the electrically unperturbed values. At this compensation point the potential gradients are nulled, making electrostatic actuation practically impossible. Accordingly, operation of a PLL close to V_{CPD} is not suitable. The peak oscillation amplitude $|a_{\mathrm{p}}(\nu_i)|$, summarized in Fig. 8.1c, increases linearly with $|V_b - V_{\mathrm{CPD}}|$ for both nanowire modes $i = 1, 2$, consistent with the expected capacitive driving force $F_{\mathrm{drive}} \propto V_0(V_b - V_{\mathrm{CPD}})$ at fixed $V_0 = 50$ mV. This dependence demonstrates that the nanowire acts as part of the capacitor formed with the underlying gold-coated surface, in line with previous reports of linear bias dependence in capacitive cantilever actuation [58]. In general, such offsets arise from work-function differences or stray charges in the measurement setup [32]. While this compensation point has no particular significance for the present measurements far from the surface, it becomes highly valuable in imaging experiments close to a sample, where setting $V_b = V_{\mathrm{CPD}}$ suppresses electrostatic force gradients and thereby enhances the magnetic contrast in MFM [59].

8.3 Cobalt Tips

To impart magnetic sensitivity, we draw on lessons from early tests with GaAs/GaMnAs nanowires bearing MnAs droplets [60] and standalone Co probes grown by focused-electron-beam-induced deposition (FEBID) [21]. In those initial experiments GaAs wires, carrying roughly spherical MnAs droplets ($D \approx 200$ nm), exhibit high mechanical quality factors between $Q = 35\,000$ and $Q = 45\,000$) [61], but the large droplet size limits spatial resolution and the lack of a well-defined magnetic anisotropy axis makes the interpretation of magnetic signals challenging without previous characterization. Shaping the MnAs droplets by focused ion beam milling in an attempt

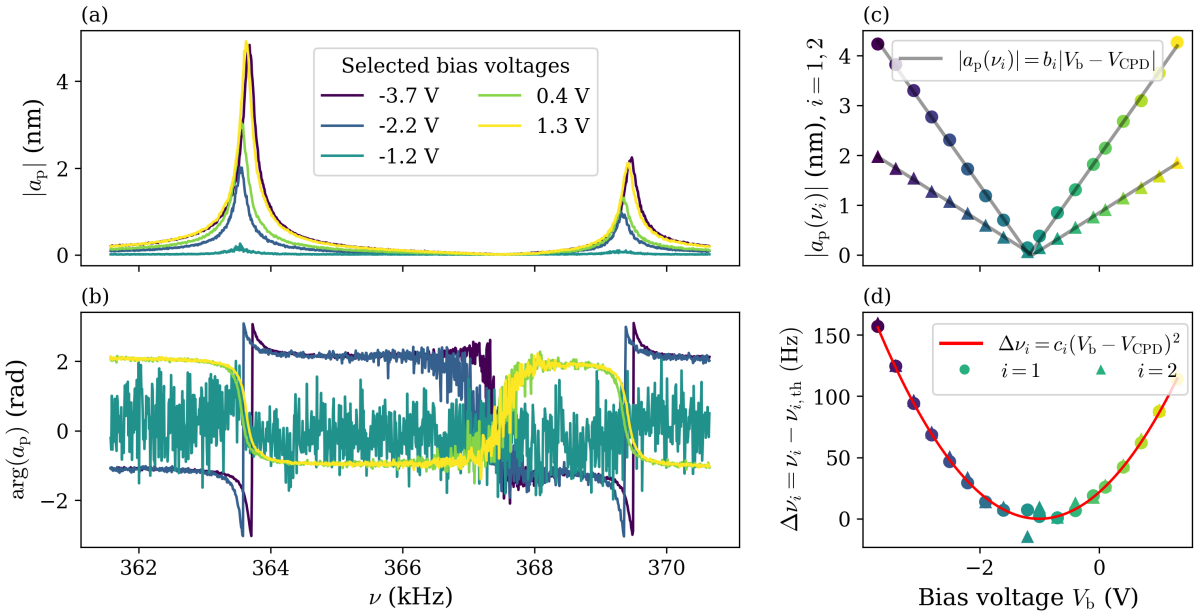

Fig. 8.1. Bias-dependent electromechanical response of a nanowire. (a) Oscillation magnitude $|a_p|$ of frequency-response sweeps under electrostatic gate actuation for five selected gate biases. (b) Corresponding phases $\arg(a_p)$ traces. All magnitude curves are fitted. The fit parameters include the bias-dependent (c) peak values $|a_p(\nu_i)|$ and (d) resonance frequencies ν_i, $i = 1, 2$ denoting the two nanowire modes. (c) The peak values quantify the bias-dependent actuation efficiency. Linear fits (grey) yield coupling coefficients (slopes) $b_1 = 1.70$ nmV^{-1}, $b_2 = 0.76$ nmV^{-1} and the contact-potential difference $V_{CPD} = -1.1$ V. (d) Quadratic fits (red line) return the nanowire intrinsic resonance frequencies $\nu_{1,th} = 363.515$ kHz, $\nu_{2,th} = 369.306$ kHz, tuning coefficient $c_i = 21.5$ HzV^{-2}, and contact potential difference $V_{CPD} = -1.0$ V.

to increase geometric anisotropy did not pin the magnetization sufficiently in those droplets. FEBID-grown Co wires are much thinner (D = 80–100 nm) and thus offer superior resolution and sensitivity down to 3 nTHz$^{-1/2}$ at 250 nm tip-sample distance [21], owed to their low mass and large magnetic point charge. However, they suffer from pronounced laser-heating [21, 20], display lower Q, and are limited to a length $L \leq 12\mu$m limiting accessible imaging regions. Their low Q renders acoustic (piezoelectric) actuation unreliable due to a non-flat transfer function, optical actuation reduces their Q and with it their sensitivity, and changes in illumination during imaging lead to added changes in resonance frequency shifts.

Guided by these findings, we currently use FEBID to deposit Co onto the free ends of high-Q Si nanowires from the Budakian group. This hybrid approach yields, in the optimal case, cylindrical magnetic tips (L = 0.3–1μm) with a clear anisotropy axis along $\hat{\mathbf{z}}$. Although the FEBID process reduces the native Q by about 50 %, resulting probes can retain Q between 8 000

and 20 000 at $T \approx 12$ K, higher than the pure Co wires. They also suffer far less from heating, and have an increased spatial resolution compared to the GaAs wires.

In the FEBID of Co process [62], the organo-metallic precursor gas, Co_2CO_8, is delivered through a fine capillary, as part of a gas injection system, into the high-vacuum chamber of a scanning electron microscope[2]. The capillary opening has a diameter of 300 μm. Under irradiation with the focused electron beam, the $Co_2(CO)_8$ molecules decompose predominantly through interactions with the abundant secondary electrons generated in the substrate [63]. While volatile CO ligands into the vacuum, non-volatile Co-containing fragments coalesce at the beam focus, which is set at the free end of a Si nanowire [64]. We employ the following FEBID parameters for deposition: a beam current of 100 pA, an acceleration voltage of 5 kV, and a precursor flux corresponding to a vacuum chamber pressure of 4×10^{-6} mbar. Fig. 8.2 shows a variety of resulting Co-tipped nanowires. All Co tips are deposited at the end of approximately 21 μm long nanowires with a diameters of 150 nm (Fig. 8.2a, b) to 110 nm (c). Critical for successful deposition is careful beam focusing and compensation for gas pressure gradients by adjusting the deposition orientation. Poor focusing can result in drop-shaped tips as seen in 8.2a, while pressure gradients can cause bent tips, as in Fig. 8.2c. While FEBID is inherently a local deposition technique, it is known to suffer from parasitic side deposition [65]. We suspect that such side deposition contributes to the reduction in Q of the Si nanowires. In a separate attempt, motivated both by the idea of reducing parasitic side growth in order to preserve the nanowire Q, and by the prospect of achieving a thinner magnetic tip for improved spatial resolution, we first sharpened a Si nanowire by FIB milling (Fig. 8.2d) and then tried to deposit Co from the side to form a strip-like tip. In practice, however, the growth rate was extremely low, and even long deposition times did not yield a clearly defined strip. We attribute these poor results to the limited generation of secondary electrons in the nanowire body, whose thickness is below 100 nm at the FIB cut, leading to insufficient precursor dissociation [63]. To obtain a rough estimate of suitable growth parameters before depositing onto nanowire tips, we first test the Co deposition directly on the substrate surface, i.e. the Si chip carrying the nanowires. These tests help to establish stable conditions in a geometry where charge dissipation is efficient and no beam-induced motion occurs. Deposition on planar substrates is straightforward regardless of whether the substrate is metallic (e.g. gold) or semiconducting (e.g. Si or GaAs). On an artistic note, FEBID on substrates has even been used to create a nanoscale vase or helical nanowires [66, 67]. In contrast, deposition onto nanowire tips is more challenging. Their higher electrical resistivity leads to beam-induced charging, which disturbs focus and restricts the beam current to 100 pA. In this low-current regime, the local precursor dissociation rate drops, and the Co content in the deposit is reduced. This limits both tip purity and magnetic sensitivity. Beam-induced excitation of the nanowire motion can further complicate stable operation.

[2]FEI Helios Nano Lab 650

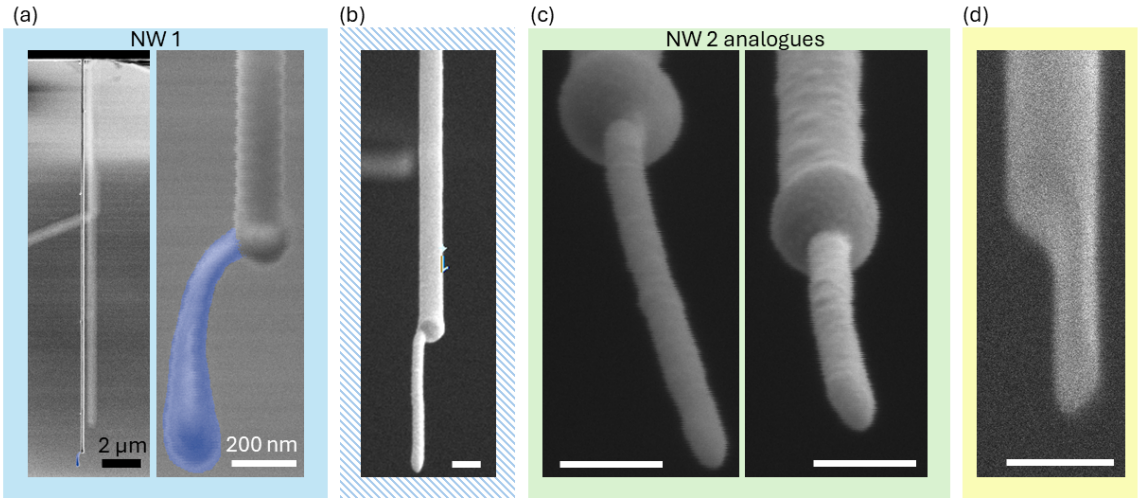

Fig. 8.2. Scanning electron micrographs of Si nanowires with Co tips. (a) and zoom-in (b) show NW 1, a first attempt of FEBID on the tip of a 150 nm wide and 21 μm long nanowire. The cobald tip is highlighted in blue. (b) Analogue to NW 1 on the same sample chip, after readjustment of the focus. (c) Nanowires of 20 μm length and 110 nm diameter with tip sizes between 60–70 nm. Despite standing on a different chip, these wires are analogues to NW 2 that was contaminated and destroyed. (d) FIB milled tip, no deposition. Black and white scale bars denote 2 μm and 200 nm, respectively.

8.4 Nanowires and Their Characterization

We generally use two approaches to characterize the tip's magnetization. The first approach uses the superconducting magnet to measure the resonance frequency response as a function of the applied field, $\mu_0 H\hat{\mathbf{z}}$, applied along the nanowire's longitudinal axis. This approach relies on interpreting both abrupt and continuous changes in the response curves. The second approach uses a patterned current-carrying wire that generates a Biot-Savart field that we use to characterize the magnetic tip [45]. We first present the response curves obtained with the superconducting magnet for two nanowires, NW 1 and NW 2, and then discuss the frequency shifts of NW 2 measured using a current loop.

The frequency response curves follow the formalism of dynamic cantilever magnetometry (DCM) [68], where the curvature of the magnetic energy with respect to small deflection angles sets the shifts $\Delta\nu_i(H)$ $(i = 1, 2)$. In this picture, each flexural mode probes the tip's equilibrium magnetization configuration. Steps in $\Delta\nu_i(H)$ mark magnetization reversal events, while continuous variations reflect the anisotropy landscape of the magnetic tip [61]. We define the reverse-field configuration by $\text{sign}(M_z) = -\text{sign}(H)$. At switching fields $sign(M_z)$ changes. In a pure 180° rotation (reversal) of the magnetization, initially aligned with the field, a sweep from H to $-H$ produces a characteristic pattern: a continuous downshift in resonance frequency as the field

decreases, a step at a single switching field, and a continuous upshift as the magnetization relaxes into the new equilibrium [68]. Accordingly, the steps observed in the response curves of NW 1 and NW 2 in Fig. 8.4 correspond to magnetization reversal events of the Co tips. The magnetization of NW 1 and NW 2 are thus mostly aligned with the external field axis during the sweeps. There are a few features, however, to consider. For NW 1, shown in Fig. 8.4b,c with the full sweep in Fig. 8.4a, we sweep the field from -8 T to $+8$ T (crosses). From -8 T up to 0 T no steps are observed. The tip magnetization remains parallel to the field. Entering small positive fields ($\mu_0 H = 0$–50 mT), the magnetization stays in the same state and is therefore in the reverse-field configuration. Between $\mu_0 H = 50$–80 mT the resonance shifts gradually upward, consistent with a progressive reorientation within the reverse-field region. At $\mu_0 H = 80$ mT the switching field is reached and the magnetization flips to become parallel to the external field. The sweep in the opposite direction (dots) shows analogous behavior. For NW 2, the sweep from -2 T to $+2$ T and back is shown in Fig. 8.4d. Coming from -2 T, two steps appear at 200 mT and at 210 mT, indicating two-step switching of the tip magnetization. The reverse sweep (green dots) exhibits the same two-step pattern.

The main difference between NW 1 and NW 2 concerns their behavior in the reverse-field configuration. NW 1 shows a gradual reorientation before reaching a switching field, whereas NW 2 switches in discrete steps without an extended gradual regime. An SEM image of NW 1 in Fig. 8.2a suggests a possible origin, a tapered, drop-like morphology that can lower local

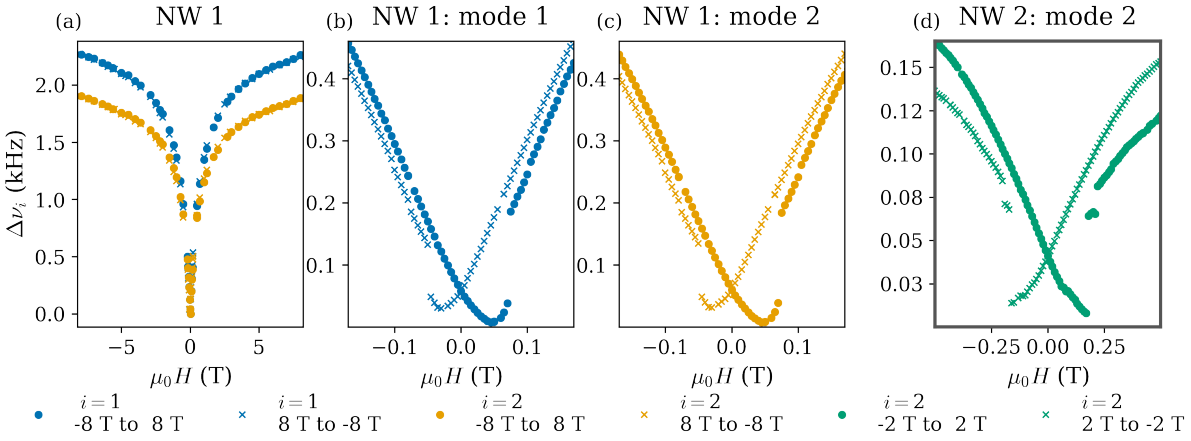

Fig. 8.3. Resonance frequency shifts ν_i as a function of magnetic field $\mu_0 H\hat{\mathbf{z}}$ applied along the nanowire's (NW) longitudinal axis. (a) Full-range frequency shifts ν_i ($i = 1, 2$ denotes the mode) for NW 1 during magnetic field sweeps from -8 T to 8 T and back (b, c) Zoom-in views of modes 1 and 2, highlighting abrupt jumps corresponding to magnetization reversals of the tip. (d) Frequency shift of mode 2 for NW 2 during field sweeps from -2 T to 2 T and back.

anisotropy barriers and favor progressive reorientation. More generally, FEBID-grown Co is typically polycrystalline [69], so uniform reversal behavior is not expected per se.

We characterize the nanowire tips using a patterned current-carrying gold wire fabricated on a Si/SiO_2 chip. The test structure consists of a straight segment with width 2 μm and thickness 50 nm. Two complementary measurements are performed. First, we evaluate the oscillating-current sensitivities of NW 1 and NW 2 by recording response curves as I_{rms} is decreased (Fig. 8.4). Second, we perform line scans across the wire under applied magnetic fields (Fig. 8.5). The resulting absolute resonance-frequency shifts are fitted with a monopole-dipole model to separate and track the monopole and dipole contributions as the external field is varied.

With the NW centered above the wire, an oscillating current with I_{rms} along $\hat{\mathbf{y}}$ generates a Biot-Savart field oscillating mainly along $\hat{\mathbf{x}}$, which magnetically actuates the nanowire modes. Actuation is strongest above the wire center, where the field is oriented purely along $\hat{\mathbf{x}}$. We show the geometry in Fig. 8.4g. At the center position the field geometry is precisely known, enabling an accurate determination of the field sensitivities of NW 1 and NW 2. Using the PLL, we locate this optimal position by maximizing $|a_{\mathrm{p}}|(x)$. Once aligned, we record response curves $|a_{\mathrm{p}}|(I_{\mathrm{rms}})$ and $\arg(a_{\mathrm{p}})(I_{\mathrm{rms}})$ for mode 1, shown in Fig. 8.4b,c for NW 1 and in Fig. 8.4e,f for NW 2. We fit the data with the mechanical susceptibility χ_1 (either magnitude only or full complex fits) and extract the peak responses, which are summarized in Fig. 8.4a,d. A data set at $I_{\mathrm{rms}} = 0$ nA provides a thermal-noise baseline, $a_{\mathrm{p}}(\nu_{1,\mathrm{th}})$. From these measurements, both nanowires are limited to a minimally detectable drive current of $I_{\mathrm{rms}} = 3.5$ nA. Since only the in-plane field component aligned with the mode axis contributes to the actuation, the effective current is reduced by the projection factor $\cos\alpha$: $\delta I_{\mathrm{rms}} = I_{\mathrm{rms}} \cos\alpha$. For both nanowires the mode orientation happens to be similar, with $\alpha \simeq 30°$, giving $\delta I_{\mathrm{rms}} \approx 3.0$ nA. Normalizing to the measurement bandwidth $\Delta\nu_{\mathrm{BW}} = 0.5$ Hz yields the mode-aligned current sensitivity at a lift height $z \approx 120$ nm, $I_{\mathrm{min}} = \delta I_{\mathrm{rms}}\, \Delta\nu_{\mathrm{BW}}^{-1/2} \approx 4.2\ \mathrm{nA\,Hz^{-1/2}}$. Using the Biot-Savart conversion at the wire center, this result corresponds to an ultimate mode-aligned stray field sensitivity of $B_{\mathrm{min}} \approx 1.1\ \mathrm{nT\,Hz^{-1/2}}$. Using Eqs. (2.15) and (5.48), we can combine F_{min} and B_{min} to estimate the effective monopole charges q_{tip} of the two nanowire tips in the monopole model. These values assume a uniform tip magnetization along $\hat{\mathbf{z}}$ and thus should be regarded as theoretical estimates. They are listed together with the other mechanical and sensitivity parameters in Tab. 8.1.

To track how the tip magnetization of NW 2 evolves with field, we fit double-demodulated current line scans across the wire with the monopole-dipole model of Eqs. (5.27) and (5.28). Scans are taken at a nominal spacing of $z = 120$ nm. Fig. 8.5 shows the recovered absolute frequency-shift data for both modes together with the fitted curves. Each field trace displays two dominant peaks with weaker shoulders on their left. At +50 mT, −50 mT, and −150 mT the fits identify a strong monopole term at an effective stand-off $z_q \approx 130$–200 nm and a minor

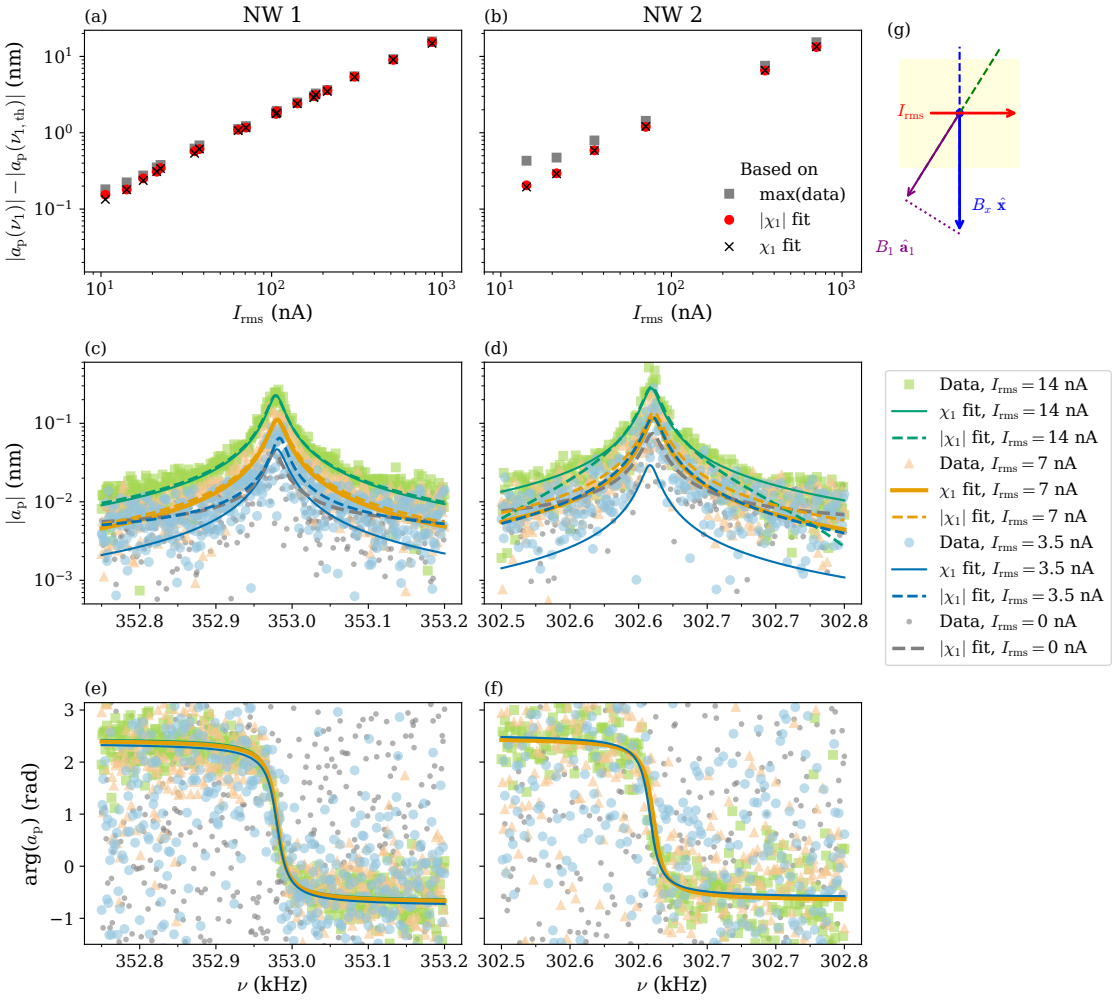

Fig. 8.4. Sensitivity of NW 1 and NW 2 to an oscillating current. Frequency response measurements are performed for multiple rms current amplitudes I_{rms} by sweeping the drive frequency through the mode 1 resonance of each nanowire. The tips are positioned about 120 nm above the center of the wire. (a,d) Peak oscillation amplitude relative to thermal noise; markers denote maxima from frequency sweeps with fits using the full complex response χ_1 and magnitude-only $|\chi_1|$. (b,c) Magnitude and phase for NW 1; (e,f) same for NW 2. (g) Schematic of the drive geometry and mode-aligned field projection.

Table 8.1. Mechanical parameters and derived quantities for NW 1 and NW 2 at $T \approx 12$ K. We provide approximate values far away from any sample surface. $\bar{Q}$ and $\bar{k}$ denote the mean of the two modes quality factors and spring constants. Force sensitivities F_{min} are defined according to Eq. (2.15), stray field sensitivities B_{min} follow Eqs. (5.46)–(5.47), and monopole charges q_{tip} are inferred from the monopole model and Eq. (5.48).

Parameter	NW 1	NW 2
Effective mass m (at tip)	3.2×10^{-16} kg	2.1×10^{-16} kg
Mean quality factor $\bar{Q}$	18 000	28 000
Mode orientation α	32°	33°
Resonance frequency ν_1	352 854 Hz	302 643 Hz
Resonance frequency ν_2	354 754 Hz	303 164 Hz
Mean spring constant $\bar{k}$	1.57×10^{-3} N/m	0.76×10^{-3} N/m
Force sensitivity F_{min}	5.1 aN $\mathrm{Hz}^{-1/2}$	3.1 aN $\mathrm{Hz}^{-1/2}$
Stray field sensitivity B_{min}	1.1 nT $\mathrm{Hz}^{-1/2}$	1.1 nT $\mathrm{Hz}^{-1/2}$
Monopole charge q_{tip} at $z_q = 120$ nm, $\mu_0 H = 0$ T	4.6×10^{-9} A m	2.8×10^{-9} A m
Stray field at sample $\mu_0 H(q_{\mathrm{tip}})$ (120 nm from q_{tip})	32 mT	20 mT

dipole contribution. The fitted monopole strength decreases by about one order of magnitude across this range. We find $q_{\mathrm{tip}} \approx 4 \times 10^{-9}$ A m at +50 mT and $\sim 10^{-10}$ A m in reverse field. As the monopole weakens, the shoulders grow and the dipole term becomes prominent at −230 mT. Fig. 5.2b shows the in-plane dipole signature that matches the observed two-shoulder pattern. In the reverse-field range the fitted dipole height is $z_m \approx 540$–560 nm for fields from −0.15 T to −0.23 T. Between −230 and −250 mT the tip magnetization reverses. At −250 mT the shoulders largely vanish and the characteristic two-peak monopole pattern returns. The same behavior is visible at −270 mT in Fig. 8.5. In summary, in aligned field the magnetic tip of NW 2 shows a largely out-of-plane magnetization that is well described by a monopole. In reverse field the response becomes dipole-like and the in-plane dipole contribution dominates just before the switch.

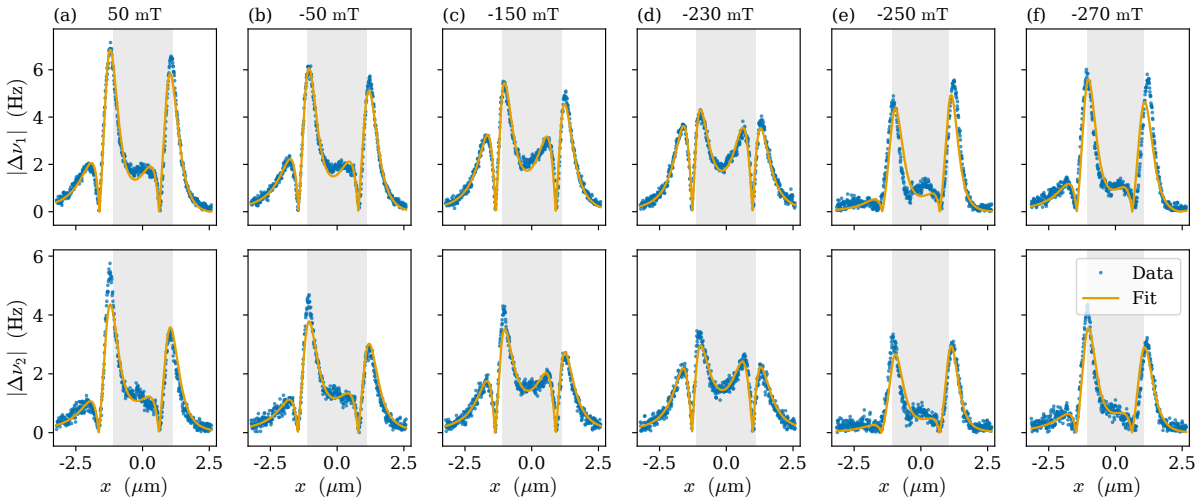

Fig. 8.5. Line scans at different magnetic fields across a straight wire segment with a quasi-DC current of $I = 29$ μA modulated at $\nu_{\mathrm{ref}} = 80$ Hz. The absolute resonance frequency shifts of mode 1 (top row) and mode 2 (bottom row) were obtained by double demodulation of the PLL frequency signal. The data are shown together with fits to a monopole-dipole model. In reverse field, the dipole contribution increases.

9. Sample Preparation and Imaging Constraint

The NW-MFM microscope uses a single nanowire oriented along z, while the sample stage translates in the xy-plane and the confocal beam is directed laterally along x. To prevent the nanowire chip, or any of the wires, from contacting the sample, the sample's top face must be sufficiently flat and free of debris. It should be mounted as parallel to the nanowire chip as possible. Any tilt exceeding the wire length will result in collision.

Equally critical for imaging is ensuring that the region of interest on a sample lies as close as possible to the sample's edge facing the objective. We define the working distance x_{WD} as the lateral distance along the optical axis between the nanowire, which coincides with the optical focus, and the nearest sample edge accessible to the confocal beam, see Fig. 9.1.

The laterally delivered confocal beam is focused onto the nanowire sidewall. At the focal spot the beam waist is smallest, but it diverges both upstream and downstream of the optical axis. Near the edge at small x_{WD} the beam reaches the focus without obstruction, as schematically drawn

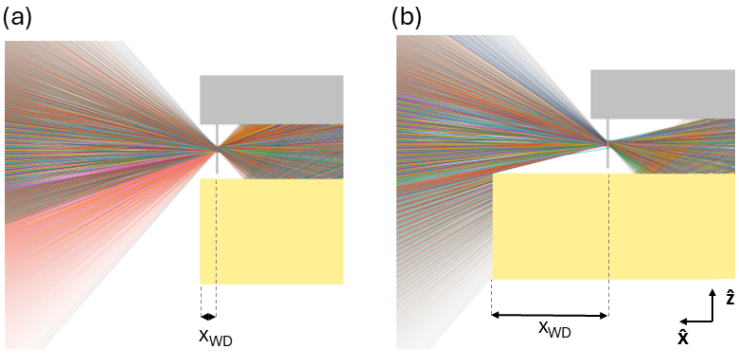

Fig. 9.1. Cartoon of the geometric detection access constraints (simple ray tracer, no wave optics or scattering). (a) Near the sample's (gold) edge (small x_{WD}), beam path and back scattering are unobstructed. (b) Far from the edge (large x_{WD}), the sample occludes the beam and detection is hindered.

in Fig. 9.1a. If the nanowire (and thus the probed sample surface) sits at a working distance $x_{WD} \gtrsim 100$ μm (i.e. more than 100 μm from the edge), a considerable portion of the diverging beam intersects the bulk of the sample before reaching the focal spot on the nanowire. This clipping significantly reduces the collection efficiency. See Fig. 9.1b for a cartoon of this access limitation. While imaging beyond this threshold is not strictly impossible, as demonstrated by in the appendix Fig. D.7 showing an image acquired at $x_{WD} \approx 170$ μm, the detection efficiency becomes severely compromised. For this reason, any region of interest beyond $x_{WD} = 100$ μm-zone is ideally cleaved or sectioned so that it abuts the new edge. In the cartoon, the beam is drawn focused at approximately the mid-length of the nanowire. This focus position improves the accessible imaging region while preserving acceptable detection sensitivity. Detection at the fixed base is not feasible, and we also avoid focusing right at the tip because local heating of the Co tip degrades Q [21].

Finally, whenever possible, to minimize electrostatic forces, sputter[1]-coat a conformal 10-15 nm Au layer onto the sample. This thin conductive film neutralizes surface charge and suppresses stray electric fields that could deflect the low-stiffness nanowire, impede proper approach, or introduce spurious electrical signals that might be mistaken for magnetic ones, all without affecting genuine magnetic measurements.

[1] EM ACE600, Leica

Magnetic Imaging

NW-MFM has been demonstrated at the proof-of-concept level in Refs. [21, 61]. In this part, we use the technique to obtain research-relevant magnetic contrast in a qualitative sense. Imaging procedures are outlined, temperature and field dependences are documented, and controls are included to rule out non-magnetic artifacts. When a magnetic field was used, it was applied exclusively out-of-plane ($\mu_0 H\hat{\mathbf{z}}$). In all images, the top of the frame is closer to the microscope objective than the bottom.

In the images, the mapped quantity is either the frequency shift of individual modes, $\Delta\nu_i$ ($i = 1, 2$), or the negative sum of the force gradients along the two mode directions, $f_+ = -(f_1 + f_2)$, which is comparable to conventional MFM contrast according to Eq. (5.20). For two-dimensional (2D) magnetic systems we perturb the sample with the nanowire's magnetic tip. In this regime f_+ and the oscillation magnitude derived dissipation Γ_+ are interpreted as signatures for the real and imaginary parts of the complex magnetic susceptibility based on Eqs. (5.42) and (5.43).

The chapters that follow present measurements on the chiral helimagnet copper(II)-oxoselenite ($Cu_2O_2SeO_3$), and the two 2D magnetic systems chromium germanium telluride ($Cr_2Ge_2Te_6$), and europium germanide ($EuGe_2$).

10. Magnetic States of $Cu_2O_2SeO_3$

Copper(II)-oxoselenite, $Cu_2O_2SeO_3$, is a chiral magnet with a cubic crystal structure below the magnetic transition temperature of about 58 K [70]. The absence of inversion symmetry, explained by its chirality, permits the antisymmetric Dzyaloshinskii-Moriya interaction (DMI), which arises from spin-orbit coupling [71, 72]. The magnetic ground state of $Cu_2O_2SeO_3$ is governed by the competition between dominant symmetric exchange, DMI, and weak magnetocrystalline anisotropy. This interplay stabilizes a long-wavelength helical spin configuration [70, 73], in which the magnetization rotates within a plane perpendicular to the (helix) propagation vector $\mathbf{q}$. The magnitude of $\mathbf{q}$ defines the wavelength $\lambda = 2\pi/|\mathbf{q}|$, characterizing the spatial

periodicity of the spin structure. The orientation of $\mathbf{q}$ within the crystal's cubic symmetry can be expressed in spherical coordinates, where the polar angle θ specifies its deviation from the [001] axis (approximately the direction of the applied field in our experiment), while the azimuth angle ϕ specifies the orientation of $\mathbf{q}$ within the (001) plane, relative to the cubic axes [100] and [010]. In zero magnetic field, the cubic axes are symmetry-equivalent and energetically degenerate, allowing magnetic domains with $\mathbf{q} \parallel |001|$ [74]. When the magnetic field is applied along [001], the helical domains with $\mathbf{q} \parallel [001]$ become energetically favored. With increasing field strength, the spin system undergoes a phase transition into a tilted spiral phase, in which the magnetization precesses around the field direction. At sufficiently high fields, a transition into the field-polarized (FP, ferromagnetic-like) state occurs.

Of particular interest in $Cu_2O_2SeO_3$ is the coexistence of magnetoelectric coupling and skyrmion-hosting behavior. Noncollinear magnetic textures induce an electric polarization, rendering the system multiferroic and offer a route toward electric-field manipulation of skyrmions [75, 76, 77, 78]. Since electric fields can be applied with negligible dissipation, unlike electric currents which cause Joule heating, this coupling holds promise for low-power operations on memory [78]. Additionally, the reduced thermal load would allow for more compact device architecture.

$Cu_2O_2SeO_3$ exhibits a rich temperature-field phase diagram [79]. In Ref. [78], we study the low-temperature magnetic phases and their transitions in detail, including the observation of a distinct surface state and a skyrmion phase. The primary imaging technique employed is scanning SQUID magnetometry using a superconducting quantum interference device mounted at the apex of a quartz capillary. This probe is scanned across the (001) surface of the crystal, and by applying an electric potential to the tip, individual skyrmions can be moved from their pinning sites. To further investigate the crystal surface's stray field structure and resolve the helical ground state, we employ NW-MFM as a complementary technique. Initial attempts to image the bare surface proved challenging due to strong electrostatic disturbances, likely arising from local surface charge patches. These effects dominate the signal at a lift of 150–170 nm, as illustrated in Fig. E.1. No clear magnetic contrast can be identified. Moreover, the application of external magnetic fields leads to significant frequency shifts even at a large lift of several microns, as shown in Fig. E.2, highlighting the strong long-range electrostatic interactions.

To mitigate electrostatic disturbances, a 10 nm thick gold layer is sputtered onto the sample surface to provide a uniform and grounded electric environment. This metallization effectively suppresses electrostatic disturbances and enables high resolution NW-MFM imaging of the magnetic structure. For the subsequent MFM imaging NW 2 is chosen for its high Q and its mode angle (see Tab. 8.1) that allows to optically address and detect both modes.

Before starting the imaging, we verify the magnetic state of the nanowire tip. A magnetic

field sweep revealed the characteristic jumps in the resonance frequencies shown in Fig. 8.3, confirming the presence of a magnetized tip, with magnetization largely along the crystal's [001] direction. Next, we use the integrated heater to raise the sample temperature above the transition temperature ($T = 65$ K $> T_c$) to reset the magnetic system to its ground state configuration upon zero field cooling (ZFC). All subsequent imaging is performed at 5 K. After ZFC, we image at a tip-sample spacing (lift) of about 30 nm and observe the periodic modulation shown in Fig. 10.2a. The 2D fast Fourier transform (FFT) in Fig. 10.2b shows a well-defined peak at $\mathbf{k} \approx (10.6, 11.1)\ (\mu\text{m})^{-1}$, corresponding to a measured wavelength $\lambda_\text{m} \approx 64$ nm. The modulation propagates along the crystal's [100] axis, consistent with a helical ground state. A complementary view with modulations propagating along both [100] and [010] is shown in Fig. D.2 in the appendix, where two diagonal channels meet and the junction reveals the two propagation directions. Literature values for the helical state's modulation period lie in the range $\lambda \approx 60$–62 nm [70]. Our slightly larger λ_m reflects a rough scanner calibration derived from larger, less well-defined samples. In this sense, the helical period serves as an *in situ* calibration of the

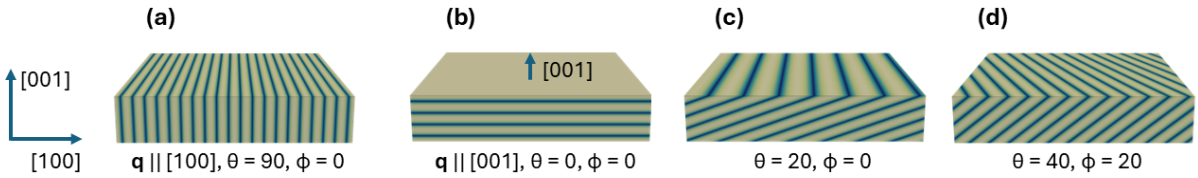

Fig. 10.1. Illustrations of spiral spin textures in $Cu_2O_2SeO_3$. (a) Helical state with propagation vector $\mathbf{q} \parallel [100]$. (b) Helical state with $\mathbf{q} \parallel [001]$ perpendicular to the imaging direction. (c) Tilted spiral with polar angle $\theta = 20°$ and $\phi = 0$, (d) Tilted spiral with $\theta = 40°$ and $\phi = 20°$.

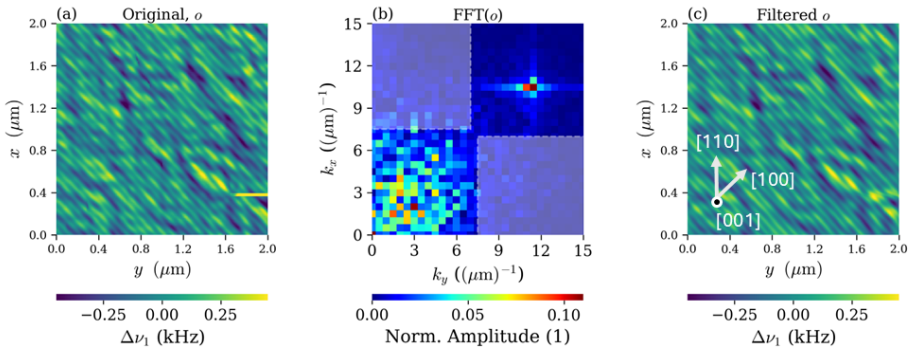

Fig. 10.2. Helical phase after ZFC at $\mu_0 H = 0$ T. (a) Frequency shift of mode 1 at about 30 nm tip-sample distance and (b) FFT, where the peak in the top right corner corresponds to a modulation period of about 64 nm. The white shaded regions are filtered to yield (c) the filtered frequency shift image with annotated crystal axes as extracted from the FFT.

scan distance. Applying a **k**-space mask and inverse transforming yields the filtered real-space image shown in Fig. 10.2c. The measurement of the 64 nm modulation benchmarks the spatial resolution of our sensor and represents the best resolution achieved to date in our NW-MFM setup.

We now focus on the crystal's magnetic field evolution after ZFC shown in Fig. 10.3. The top row (a) shows overview images acquired at a lift of 150–170 nm over a 10 μm $\times$ 10 μm scan area while the magnetic field is increased. The bottom row (b) shows high resolution maps of a 2 μm $\times$ 2 μm area acquired at a smaller lift of 30–40 nm. Both the overview images and the high resolution maps are taken at the same positions throughout the series.

At 0 mT, the overview shows only topographic contrast. Two slightly brighter particulate features act as convenient markers that can be tracked as the field is increased, confirming that we repeatedly image the same region. The white frame marks the area analyzed in Fig. 10.2, where the helical modulation is demonstrated. At a 150–170 nm lift this modulation is blurred and therefore not visible. Increasing the field to 32 mT reveals a diagonal boundary that separates a region with in-plane helical modulation (I) from a region where the modulation disappears (II), consistent with **q** rotating out of plane (a small patch of a second in-plane domain is visible in the lower-left corner). To understand why the contrast vanishes for the lower region, consider Fig. 10.1. In panel a, **q** lies in the surface plane along [100]. In panel b, **q** points out of plane along [001]. NW-MFM images the surface projection of the spiral and thus measures a projected period $\lambda_\mathrm{m} = \lambda / \sin\theta$. For in-plane **q** ($\theta = 90°$) we obtain $\lambda_\mathrm{meas} = \lambda \approx 64$ nm and clear stripes are visible. In the limit $\theta \to 0°$ (out-of-plane **q**), the projected wavelength diverges, and thus no periodic signal can be detected by MFM. As shown in Fig. 10.1, this corresponds to the absence of modulation at the top of the crystal schematic. At 36 mT a channel of in-plane helical modulation forms (I), while a faint stripe pattern develops in the out-of-plane helical domain (II). A similar stripe pattern is already established in another out-of-plane domain in the top-right corner of the overview. (A related channel that hosts in-plane helices is shown in Fig. D.1 in the appendix, recorded after FP at 500 mT.) At 37 mT the in-plane helical channel narrows and the stripe pattern begins to dominate. In the 37 mT high resolution map we clearly see the helical modulation within the channel (I), but not in the stripe pattern region (II). The in-plane helical modulation disappears between 37 and 43 mT. By 43 mT the stripe pattern covers the entire field of view. As the field increases, the stripe state persists and largely orients along [110]. At 51 mT the stripes become fewer and narrower, about 400–600 nm wide in the high resolution image, where we also observe a weak periodic modulation along [110]. At higher fields, the stripe pattern breaks up and vanishes. At 74 mT only the periodic modulation remains. Upon further increase, the modulation period decreases and its propagation direction gradually tilts away from [110] by the azimuth angle ϕ (clearly visible at about 90 mT). At 102 mT any magnetic contrast is gone, consistent with the FP phase. This FP field threshold is position-dependent:

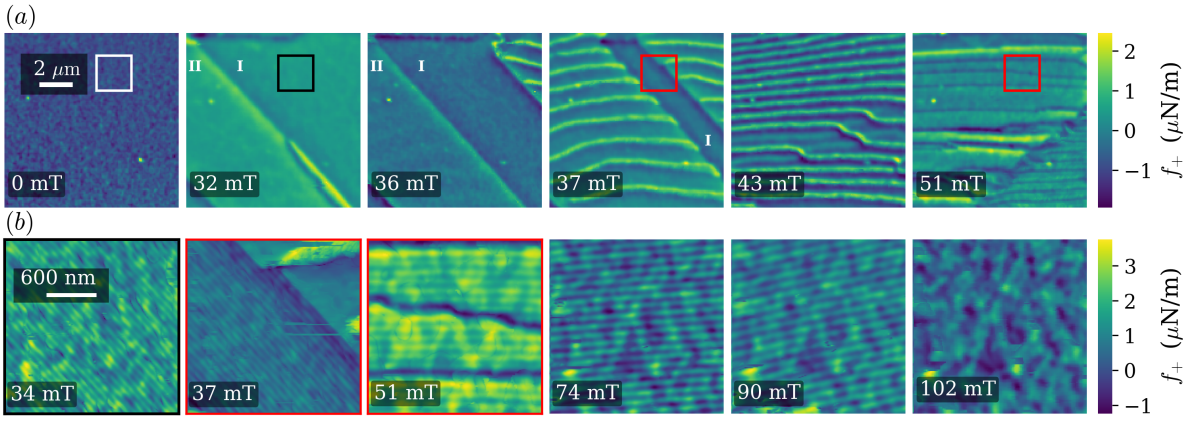

Fig. 10.3. Magnetic contrast between the (001) surface of $Cu_2O_2SeO_3$ and NW 2 at increasing magnetic field after ZFC. The field is oriented approximately along the crystal's [001] axis. The cumulative force gradient f_+ is defined in Eq. (5.20). (a) Overview maps acquired at a lift of 150–170 nm. When a high resolution scan is acquired at the same field, the corresponding overview panel is outlined for convenience. The white frame marks the location used in Fig. 10.2a. Labels I and II indicate regions with $\mathbf{q} \parallel [100]$ and $\mathbf{q} \parallel [001]$, respectively. (b) High resolution maps acquired at the same location at a lift of 30–40 nm. The in-plane helical state ($q \parallel [100]$) persists up to about 38 mT, while the FP state is reached near 102 mT; both transition fields are position dependent.

Within about 30 μm of the sample edge the transition occurs at lower applied field, whereas farther from the edge the polarized state is reached at around 120 mT and nucleates locally as islands, consistent with reduced demagnetizing fields and a slightly thinner crystal near the edge. At the transition to the FP state, SQUID imaging reveals skyrmions. With NW-MFM we were not able to find this skyrmion phase, which could again be due to the closeness to the crystal edge.

The dominant features in the images of Fig. 10.3 beyond the helical phase are the stripe pattern and the onset of a modulation at around 50 mT. The latter corresponds to a tilted spiral phase, where the increase in λ_m corresponds to a larger polar angle θ, as illustrated in Fig. 10.1c. This relation is confirmed by SQUID stray field measurements, from which the angles θ are extracted and plotted in Fig. 10.4a. Their field dependence (λ_m) indicates a progressive reorientation of the propagation vector $\mathbf{q}$ away from [001], consistent with the emergence of a tilted spiral phase evolving from the bulk conical spiral ($\mathbf{q} \parallel [001]$) under increasing field.

The tilt originates from the competition between Zeeman energy, which favors spin alignment along the external field (oriented close to [001]), and magnetocrystalline anisotropy, which favors

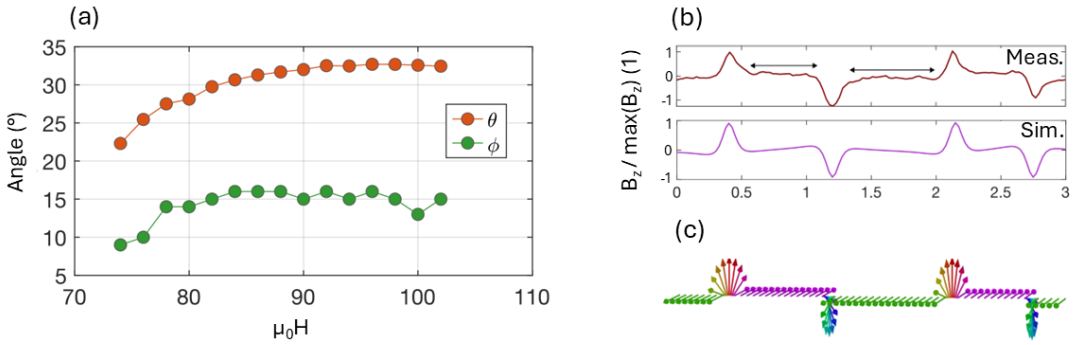

Fig. 10.4. Characteristics of the tilted spiral and surface states. From E. Marchiori et al. [78]. (a) Polar and azimuth angles θ and ϕ, respectively, as function of applied field (obtained from SQUID measurements). (b) SQUID line scan across stripes at low field (- 4 mT) and field simulation data assuming an idealized magnetic stripe state. (c) Schematic of an idealized magnetic stripe state.

propagation along the cubic $\langle 111 \rangle$ axes. This competition drives a steady increase in θ, tilting $\mathbf{q}$ away from the field axis toward a nearby $\langle 111 \rangle$ direction (e.g. [111]). Such a field-induced reorientation has been predicted theoretically [80].

Alongside this evolution of θ, the azimuthal angle ϕ also changes with applied field. The extracted values of ϕ are shown in Fig. 10.4a, and the effect is clearly visible in the high resolution images at 74 mT and 90 mT (Fig. 10.3), where the modulation appears tilted. This reorientation is illustrated schematically in Fig. 10.1d. The gradual evolution of ϕ can be attributed to a small in-plane component of the applied field relative to the crystal cut, which introduces an additional Zeeman energy contribution. As a result, the otherwise smooth reorientation of $\mathbf{q}$ from [001] toward [111] is slightly perturbed, producing a continuous rotation of $\mathbf{q}$ within the surface plane. The combined evolution of both θ and ϕ therefore reflects a multidimensional field response of the spiral, governed by the interplay between magnetocrystalline anisotropy and the precise alignment of the external field with the cubic axes.

The stripe patterns present a qualitatively different behavior. Unlike the tilted spiral phase (70–90 mT), the stripes do not consistently align with the bulk helical propagation directions. At a constant applied field, they display continuous orientation changes even at low fields (36–37 mT), behavior not observed in pure spirals. This deviation suggests that the stripes represent a distinct magnetic surface state arising from broken symmetry at the surface. The origin of such a state can be considered in terms of competing surface and bulk energetics. A surface state based on stacked spin spirals coexisting with the bulk conical phase has been postulated in [81], but its wavelength and field dependence do not match our observations. Instead, the stray field patterns we observe are most consistent with the in-plane magnetic stripe state described by Osorio et

al. [82], particularly near zero field. This state is characterized by distorted helices composed of extended stretches of in-plane magnetization interrupted by short out-of-plane rotations. Strong experimental evidence for this scenario is provided by the SQUID line scan at −4 mT shown in Fig. 10.4b, which reveals the stray field modulation associated with the stripes. The data correspond closely to simulations of an idealized stripe state illustrated in Fig. 10.4c, reinforcing the interpretation of the stripes as a distinct surface-derived magnetic phase.

In summary, the NW-MFM imaging presented here provides a high resolution view of the magnetic textures in $Cu_2O_2SeO_3$. By directly resolving the projected stray field, it captures both the bulk helical and tilted spiral phases as well as surface-derived states such as the stripe pattern. This imaging not only benchmarks the spatial resolution achievable with our nanowire sensors but also reveals subtle aspects of the multidimensional field response in this chiral magnet, underscoring the unique advantages of NW-MFM for investigating noncollinear spin textures at the nanoscale.

11. Magnetic Imaging of $Cr_2Ge_2Te_6$

The ability to mechanically isolate atomically thin layers from bulk crystals, or ideally to directly synthesize them on substrates, has opened access to a wide range of 2D materials. These materials often differ markedly from their bulk counterparts and exhibit properties that vary with layer number. Even a single atomic layer may behave as a distinct material relative to a bilayer [83]. By stacking different layers, heterostructures with entirely new emergent properties can be engineered. This combinatorial flexibility to tune electronic, magnetic, optical, and mechanical behavior has pushed research to the 2D limit.

Magnetism in 2D materials is of both fundamental and practical interest. Fundamentally, it offers access to exotic phases and unconventional magnetic ground states. Practically, it promises impact in spintronics, where 2D magnets are key components for ultra-compact and energy-efficient devices [84]. Chromium germanium telluride, $Cr_2Ge_2Te_6$ (CGT), is a soft ferromagnetic (FM) insulator with a layered crystal structure [85] and uniaxial magnetic anisotropy along [001] [86]. In the bulk, it exhibits a saturation magnetization of $M_s = 3\ \mu$B/Cr and a Curie temperature in the range of $T_C = 61$–68 K [87, 88, 89, 90]. Because its layers can be mechanically separated down to a monolayer using standard exfoliation, CGT is a van der Waals (vdW) material, characterized by weak interlayer bonding. Crucially, FM order persists down to the bilayer limit in CGT [90], making it one of the first materials shown to host intrinsic 2D FM. In exfoliated flakes, T_C decreases with decreasing layer number. In particular, bilayers exhibit a magnetic

transition around $T_C \approx 30\ K$ under an applied out-of-plane field of 75 mT, compared with $T_C \approx 61$–$68\ K$ in bulk [90]. This distinction is important, since the bilayer T_C is field dependent in this magnetically soft system [90]. In the bilayer, the saturation magnetization is reduced to $M_s \approx 2.2\ \mu$B/Cr, which has been attributed to reduced interlayer exchange and enhanced thermal spin fluctuations [90, 91]. As such, CGT is a model system for exploring magnetism in the 2D limit.

CGT is used to investigate the bidirectional interaction between a vibrating magnetic nanowire and the sample's magnetic landscape. The nanowire's dynamics are influenced by the spatial distribution of the sample's stray field, while the magnetic tip perturbs the local magnetization via an effective magnetic potential. These tip-induced changes feed back on the nanowire's motion. Resonance-frequency shifts are assumed to reflect the real part of the magnetic susceptibility, and variations in damping are assumed to reflect the imaginary part.

A CGT flake previously characterized in Ref. [92] serves as the testing ground. As in the previous section, we use NW 2 for this investigation (see Tab. 8.1 for nanowire characteristics). The study proceeds in two stages. First, we verify FM order by mapping the magnetic signal at various out-of-plane fields at $T = 4.5\ K$. Second, we record spatial maps of resonance-frequency shifts and oscillation amplitudes as a function of temperature, tracking how different regions traverse their layer-dependent Curie transitions. Reliable NW-MFM operation requires positioning the region of interest within the working distance $x_{WD} \lesssim 100\ \mu$m (see Chap. 9). To meet this constraint, we cleave the Si/SiO_2 chip carrying the hBN-encapsulated[1] CGT flake to position the flake near the new chip edge, within the imaging-accessible zone. In practice, the cleave intersects the flake, exposing its edge to ambient conditions. For electrostatic screening and imaging stability, we coat the entire chip, including the flake, with a 10 nm Au layer. Without screening, polymer residues from exfoliation induce charging-related kHz-level frequency shifts.

11.1 Field-Dependent Magnetic Contrast

FM order is confirmed across the 13-, 14-, and 16-layer regions by the field-dependent imaging sequence shown in Fig. 11.1. The series begins at −60 mT following a prior +60 mT conditioning field. At −60 mT, the NW 2 tip is magnetized in reverse field. We observe characteristic force gradient contrast between a monopole-like magnetic tip and an out-of-plane sample magnetization. When scanning across an edge toward increasing layer number, a downshift followed by an upshift of the two resonance frequencies indicates that the tip magnetization is opposite to that of the sample. This signature is most pronounced at the flake boundary. Reducing the field to 0 mT produces bright spots that nucleate predominantly at edges. These spots may correspond

[1] The hBN is about 10 nm thick with small variations.

to magnetic bubbles reported for CGT [92, 93, 94], here arising from incomplete saturation during iterative field cycling. A tip-induced mechanism (permanent bubble nucleation by the tip's static stray field) is unlikely, since it would manifest as abrupt stray field changes and step-like frequency jumps that we do not observe. However, considering a tip stray field at the sample of $\mu_0 H_{\text{tip}} < 12.6$ mT[2], it cannot be entirely excluded, especially because formation starts at the thinner layer while in scanning SQUID measurements formation starts at the 16-layer region (though without field cycling). As the field is increased to positive values, the spot density grows, initially filling the 13-layer region between about 3 and 7 mT and then extending into the 14-layer region. Around 10 mT the force gradients become too large for a clear NW-MFM signal. By 15 mT the gradients weaken and standard imaging works again. The evolving patterns are consistent with micromagnetic simulations of labyrinth domains reported for this flake of CGT [92]. By +40 mT, the domain contrast vanishes and the flake aligns with the tip. The layer edges show up-then-down frequency shifts, a signature of aligned flake and tip magnetization, in contrast to the down-then-up frequency shifts at −60 mT. We conclude that the CGT flake exhibits layer-dependent FM order.

Concerning the image at 10 mT in Fig. 11.1, we would like to address the scanning artefacts related to PLL operation. At this field, the tip-sample force gradients are too strong for reliable PLL tracking with NW 2. This is due to the relatively small intrinsic mode splitting of NW 2, only about 520 Hz (see Tab. 8.1). In the presence of strong force gradients, the resonance frequencies of the two modes shift even closer together, leading to the merging of resonance peaks and, most critically for PLL operation, the loss of a well-defined phase response. Under such conditions, PLL tracking becomes unreliable or fails entirely, which limits the spatial resolution: while reducing the tip-sample distance would typically enhance spatial resolution, it also increases force gradients and thus worsens PLL applicability. One way to overcome this limitation is to acquire displacement-noise PSDs and extract the resonance frequencies directly from the spectra. While doable as demonstrated in Ref. [95] (see also appendix Fig. D.3), this approach is very time-consuming. Alternatively, one could engineer a larger intrinsic mode splitting to maintain PLL functionality even in the presence of strong force gradients. This could be achieved by fabricating more asymmetric nanowires or, to some extent, by increasing Q (see Fig. 4.2). Another strategy could involve selectively biasing one mode using a directional force gradient, thereby increasing or preserving the frequency separation between modes.

[2]The value of 12.6 mT is based on a pure monopole field at 150 nm, c.f. Tab. 8.1

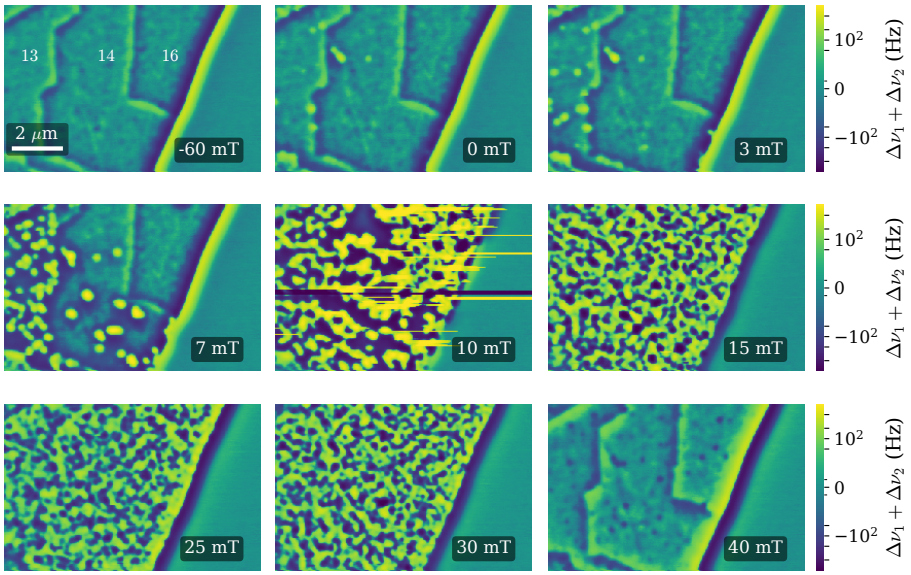

Fig. 11.1. Field-dependent magnetic response of CGT at 4.5 K at a lift of about 150nm. Labels 13, 14, and 16 indicate the layer count (per Ref. [92]). Images correspond to fixed applied fields increased from −60 to +40 mT. The tip is magnetized in reverse at −60 mT. The prior field was +60 mT.

11.2 Temperature-Dependent Magnetic Contrast

To probe the local magnetic susceptibility contrast in CGT, we focus on temperature regimes across the layer-dependent Curie temperatures, where the susceptibility shows sharp increases as described by the Curie-Weiss law, Eq. (1.18). The resulting temperature-dependent imaging is shown in Fig. 11.3. As a reminder, the quantities f_+ and Γ_+ are derived from frequency shifts and oscillation amplitudes. According to Sec. 5.5 with Eq. 5.39 they are directly linked to a magnetic stiffness, which in turn is tightly related to the real and imaginary parts of the sample's magnetic susceptibility.

Our susceptibility measurements are performed at zero applied field, where the magnetic texture is expected to be most responsive to perturbations from the nanowire tip. However, to unambiguously associate the observed contrast in Fig. 11.3 with magnetic susceptibility, we first present reference measurements acquired at an out-of-plane field of 150 mT, shown in Fig. 11.2. At 150 mT applied field in Fig. 11.2, where the scan height is approximately 15 nm closer to the sample than in the corresponding zero field measurements, we observe force gradient contrast from the uniform magnetization of the CGT flake and from topography. As in the previous field-dependent scans, the largest signal appears at the flake's right boundary (16 layers step). The features remain qualitatively unchanged across the full temperature range from 5 K to 85 K, primarily marking the layer edges. The overall signal amplitude gradually decreases with in-

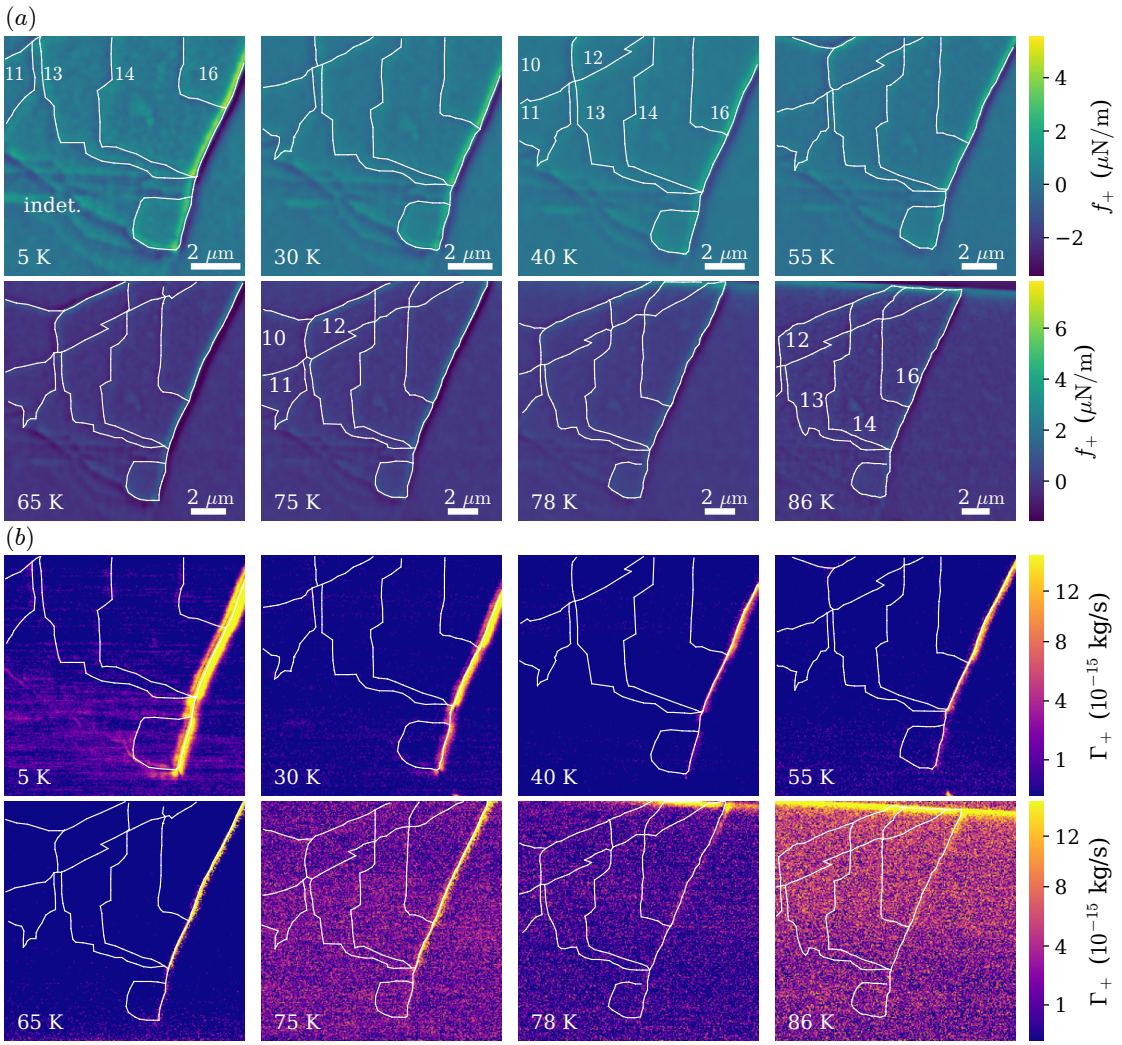

Fig. 11.2. Temperature-dependent imaging of CGT at 150 mT. (a) Force gradient f_+ calculated from resonance frequency shifts, recorded at nominal temperatures between 5 K and 86 K. Tip-sample distances range from approximately 100-130 nm, except at 86 K where the scan height was reduced to about 70 nm. (b) Corresponding dissipation extracted from oscillation amplitudes at the resonance frequencies. White contours delineate regions of different CGT layer thicknesses, based on field-polarized reference scans. Layer numbers follow the assignment in Ref. [92]. (Not all regions could be assigned a layer count.)

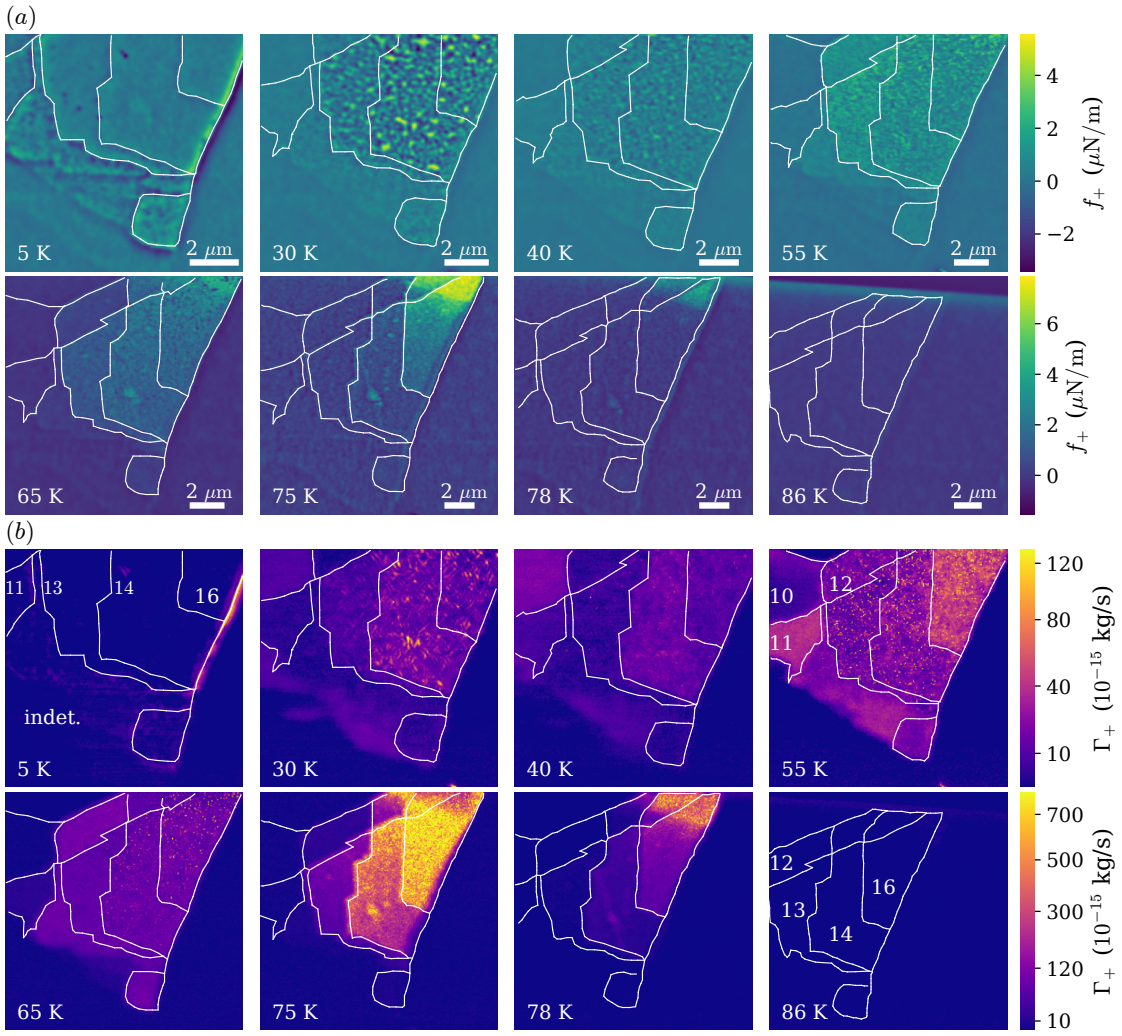

Fig. 11.3. Temperature-dependent imaging of CGT at zero applied field. (a) f_+ contrast calculated from resonance frequency shifts, recorded at nominal temperatures between 5 K and 86 K. Tip-sample distances range from approximately 90-110 nm, except at 86 K where the scan height was reduced to about 60 nm. (b) Corresponding Γ_+ contrast extracted from oscillation amplitudes at the resonance frequencies. White contours delineate regions of different CGT layer thicknesses, based on field-polarized reference scans. Layer numbers follow the assignment in Ref. [92]. (Not all regions could be assigned a layer count.)

creasing temperature, as expected upon approaching the paramagnetic phase. At the top edge of the image at 85 K, the cleaved edge of the flake becomes visible. We also note that the apparent scan area increases slightly with temperature. This is attributed to heating of the piezoelectric positioner stack by the sample heater, which changes the piezoelectric coefficients and thus the displacement per applied voltage. The annotated layer numbers in the images are based on the scanning SQUID measurements in Ref. [92]. In the bottom region of the images, however, a precise layer assignment is still pending.

We now turn to the main result: temperature-dependent imaging at zero applied field, as shown in Fig. 11.3. In this regime, the CGT flake is magnetically less *stiff*, as the spins are no longer pinned by an external field. The tip-sample interaction is therefore more sensitive to local variations in magnetic susceptibility. We discuss the image series in the order they were acquired, from low to high temperature. At 5 K, the thicker part of the flake appears largely uniformly magnetized, while some structure becomes visible in the lower part of the image-corresponding to thinner regions-in the force gradient signal f_+. The dissipation signal Γ_+, by contrast, shows no significant features at this temperature. Upon increasing the temperature to 30 K, strong f_+ contrast emerges in the thicker 13-, 14-, and 16-layer regions. This may be related to the formation of domains as discussed in the previous section. The f_+ contrast in the thinner regions (lower layer count) largely vanishes, however the corresponding Γ_+ contrast increases compared to the 5 K image. The increase in Γ_+ is general, with stripe-like fine structure visible in the thicker areas indicative of local dissipation associated with tip-domain interactions. We cautiously interpret the observed Γ_+ as a local proxy for the crystal's out-of-phase magnetic response $\mathrm{Im}(\chi_m(\omega_0))$, produced by the nanowire's *oscillatory*[3] stray field at $\omega_0/(2\pi) \approx 300$ kHz[4]. When the domain-wall (DW) relaxation time τ_{DW} satisfies $\omega_0\tau_{\mathrm{DW}} = 1$, wall-mediated dissipation is maximal. Reported cutoffs for DW dynamics in layered magnets span kHz–MHz [28, 25, 96]. However, the Γ_+ contrast can also be attributed to tip-stimulated nonlinear DW dynamics. At 40 K, the f_+ contrast decreases in overall intensity but remains present in similar regions. In the dissipation signal Γ_+, we draw particular attention to the top-left corner of the image, corresponding to the 10-layer region, which now shows a clear onset of contrast. This is the first indication of a magnetic response in that region. At 55 K, nearly the entire flake exhibits dissipation contrast. Interestingly, the thinner regions are now more prominent in Γ_+ than the 10-layer region, which showed stronger response at 40 K. This evolution reinforces that the observed contrast is not an artifact of tip-sample distance but tracks changes in the sample's magnetic state.

In the second row of panels in Fig. 11.3a,b we observe the progressive disappearance of contrast with further temperature increase. By 65 K, the 10- and 11-layer regions no longer show

[3]The tip field is static in the tip frame, but tip motion makes it appear oscillatory to any fixed point on the sample.

[4]$\omega_0/(2\pi) \approx (\nu_1 + \nu_2)/2$.

detectable response. At 75 K, the 12-layer region also fades, but both f_+ and Γ_+ contrast increase in the remaining thicker parts of the flake. A particularly notable feature is the bright upshift in frequency (top-right corner), which is not compensated by an equal downshift elsewhere in the image. This lack of symmetry is a hallmark of dynamic tip-sample interactions. At 78 K, the 13-layer region also becomes inactive, and the signal retreats toward the upper-right corner. Finally, at 86 K, no Γ_+ contrast remains, and the residual f_+ signal is attributed solely to topography.

While the sequence points to the expected progressive loss of magnetism upon warming [90], the pronounced dissipation detected at nominal temperatures above the reported bulk $T_C = 61$–68 K [87, 88, 89, 90] present a clear discrepancy. Sizable short-range FM correlations are known to develop well above T_C in CGT [87], and an onset in $M(T)$ derivatives near 80 K has been reported in Ref. [97]. However, because our nanowire resonates at low frequencies ($\omega_0/(2\pi) \approx 300$ kHz), while spin relaxation about 10 K above T_C is fast ($\tau \ll 1/\omega_0$), the response should be quasi-static (in-phase), and the Debye form in Eq. (1.20) predicts negligible dissipation. The fact that we nevertheless detect strong dissipation contrast at 78 K therefore points to a technical origin: the sample temperature likely lagged the sensor reading at high heater power due to our heater-sensor arrangement. The sensor is located inside the heater spool, while the sample sits on a copper carrier thermally anchored to the 4.2 K bath via a copper braid.[5] We therefore attribute the apparent dissipation contrast observed at nominal temperatures above T_C primarily to the sample being colder than indicated by the sensor reading.

To summarize, the 10-, 11-, 12-, 13-, 14-, and 16-layer regions lose contrast successively as the temperature increases. This systematic disappearance supports the interpretation that the nanowire probe senses the evolving magnetic susceptibility of CGT, with each layer group undergoing a distinct magnetic transition. Although residual contrast was detected at nominal temperatures above the reported bulk T_C, we attribute this effect primarily to a calibration offset in the heater-sensor arrangement, rather than to intrinsic magnetic order.

[5] Another experiment revealed a 1 K offset at 20 K.

12. Magnetic Phase Evolution of Few-Layer $EuGe_2$

In the preceding chapter we demonstrated that NW-MFM can resolve magnetic susceptibility contrast at magnetic phase transitions. This establishes the technique as a sensitive probe of field- and temperature-dependent magnetic response in van der Waals magnets. A natural next step is to ask whether such systems can host spatially inhomogeneous states in the 2D limit, where reduced dimensionality and enhanced fluctuations can destabilize uniform long-range order and promote competition between distinct phases. Thickness-controlled van der Waals magnets provide clear examples of this competition. In materials such as $CrCl_3$ and CrSBr the magnetic ground state evolves strongly with layer number, reflecting the changing balance between intra- and interlayer exchange interactions [98, 99]. In this regime, mixed or phase-separated states can occur, enabling phenomena such as exchange bias and tunable magnetic textures.

We now turn to europium germanide, $EuGe_2$, where magnetization measurements on ultrathin films already suggest competing components. Monolayer (1 ML) and bilayer (2 ML) both show strongly reduced saturation magnetization while the bilayer exhibits clear hysteresis [100]. These signatures suggest incomplete ordering and the coexistence of multiple magnetic components, motivating a nanoscale real-space study with NW-MFM. $EuGe_2$ is particularly well suited as a platform to study this because its bulk magnetic order is intrinsically layered. In bulk, $EuGe_2$ is an A-type antiferromagnet (AFM): within each structural layer the Eu moments align ferromagnetically, while adjacent layers are coupled antiferromagnetically along the [001] direction (the c-axis) [101]. Reducing the thickness suppresses this interlayer antiferromagnetic (AFM) coupling while preserving the strong intralayer FM tendency, creating FM/AFM competition in the ultrathin limit. To stay close to the 2D limit, we restrict our attention to the monolayer and bilayer, and ultimately focus on probing phase separation in the bilayer. In the monolayer, the loss of interlayer coupling should favor a fully FM state. However, the measured saturation moment is strongly reduced from the expected 7 μ_B/Eu, indicating that even at 1 ML the system is not fully polarized and likely hosts competing magnetic components [100]. In the bilayer, an interlayer AFM competition re-emerges, yet a finite FM component remains (remanence and hysteresis), demonstrating that 2 ML $EuGe_2$ is not a purely antiferromagnetically stacked system but instead a mixed state in which multiple magnetic components coexist.

Practically, the monolayer lies on a tall mesa that introduces strong topographic artifacts in

NW-MFM, whereas the bilayer sits on a lower plateau. We therefore begin with a short technical section on the monolayer that illustrates topography-dominated contrast and background removal, and then concentrate on the bilayer, which represents the minimal thickness at which interlayer competition is present while FM has not vanished, enabling direct nanoscale tracking of multiple magnetic phases.

12.1 Topography-Dominated Imaging of Monolayer $EuGe_2$

Despite its high stray field sensitivity, disentangling magnetic force gradients from electrostatic or topographic contributions can be challenging in NW-MFM, especially near large edges. In such cases, asymmetries that cannot arise from symmetric edge responses help identify magnetic signals. An alternative is two-pass (lift-mode) imaging [102], which we did not employ here. Instead, we demonstrate the strategy of exploiting asymmetries to reveal the reported in-plane magnetization in 1ML $EuGe_2$ grown by molecular beam epitaxy on a 100 nm plateau [100].

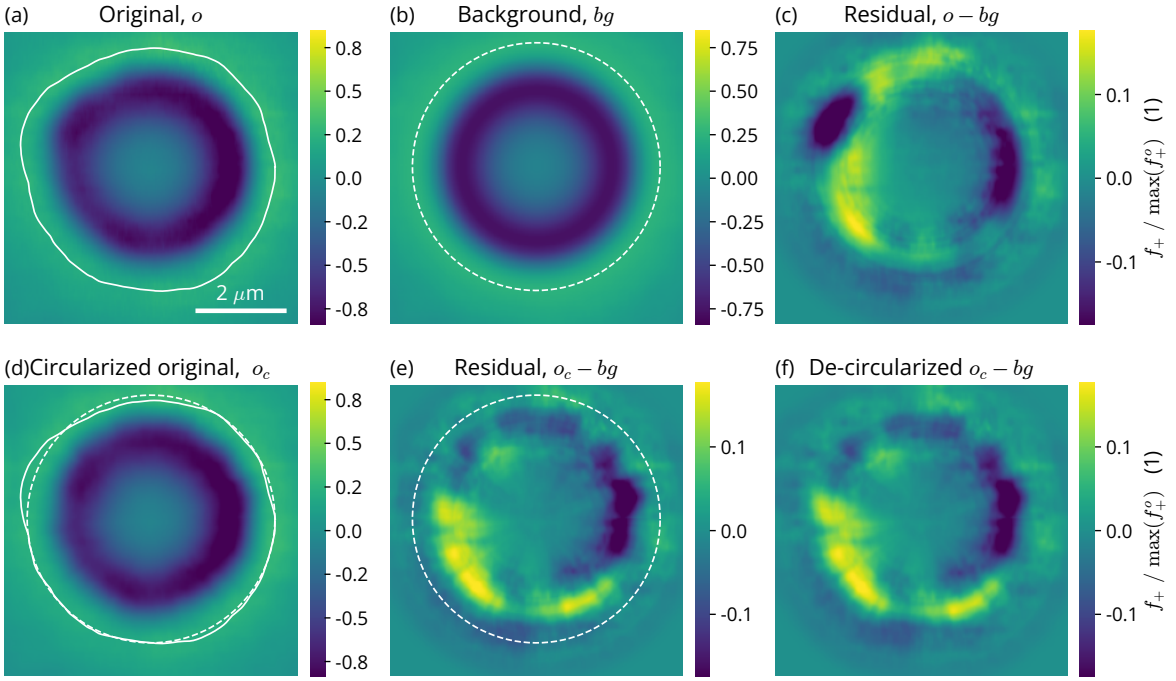

Fig. 12.1. Removal of the plateau-edge background from the 1ML $EuGe_2$ force gradient map. (a) Original f_+ map of the 1ML $EuGe_2$ on the top surface of a disk-shaped Ge plateau. The solid white curve marks the detected plateau boundary. (b) Radially symmetric background bg, with the dashed white circle indicating the topographic edge. (c) Residual in the original frame, $f_+^{(o-bg)} = f_+^o - f_+^{bg}$. (d) Circularized image o_c after boundary normalization. (e) Residual in the circularized frame, $f_+^{(o_c-bg)} = f_+^{o_c} - f_+^{bg}$. (f) De-circularized residual mapped back to the original geometry.

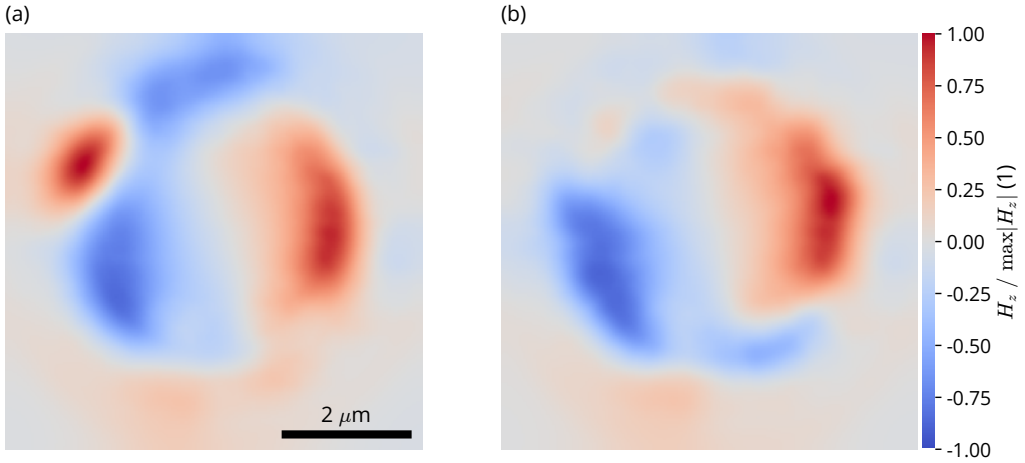

Fig. 12.2. Reconstructed H_z based on the background-removed f_+ maps of 1ML $EuGe_2$, measured at zero field and 5 K. (a) Starting from the residual from Fig. 12.1c, the map is Fourier transformed to **k**-space, operated on according to Eq. (5.20) under the monopole-tip assumption, and inverse transformed to real space to obtain H_z. (b) Equivalent reconstruction applied to the de-circularized residual from Fig. 12.1f. The bipolar contrast in (b) is consistent with a predominantly in-plane magnetization of the disc.

Fig. 12.1 shows the removal of the plateau-edge background from the original force gradient map f_+, denoted o in Fig. 12.1a. We assume that the plateau-edge response is circular, that is, radially symmetric, and construct a background map bg that captures this contribution in Fig. 12.1b. Subtracting this background from the raw map yields the residual $o - bg$ in the original frame, shown in Fig. 12.1c. To mitigate small deviations from perfect circularity, we also apply a boundary normalization (*circularization*), perform the same subtraction in that frame, as shown in Fig. 12.1e, and then map the residual back to the original geometry in Fig. 12.1f. We verified that there is no scan-plane tilt during this measurement. However, the plateau wall height was not profiled by atomic force microscopy, so asymmetric wall heights could imprint an asymmetric residual signal. The residual signal may therefore contain contributions unrelated to the magnetic texture and should be interpreted with caution.

We reconstruct the out-of-plane stray field component H_z from background-removed f_+ maps using the circular-background assumption in Fig. 12.2. For that, we take the residual in the original frame, $o - bg$, from Fig. 12.1c and the de-circularized residual from Fig. 12.1f. Each map is Fourier transformed to **k**-space, operated on according to Eq. (5.20) by dividing by

$k = (k_x^2 + k_y^2)^{1/2}$ under the monopole-tip assumption, and then inverse transformed to real space to obtain H_z. The reconstructed field over the disc displays a pronounced bipolar contrast, with one half exhibiting positive and the other half negative H_z. This dipolar pattern is consistent with opposite magnetic poles on opposite sides of the disc and thus indicates a predominantly in-plane magnetization. The measurement was acquired in the absence of an applied magnetic field at 5 K. Since no in-plane magnetic field could be applied in the experiment, it was not possible to test the stability of this magnetic configuration or the extent of magnetic moment polarization at zero field.

A rigorous control, consistent with the circular background assumption, would be to image the same area using a non-magnetic nanowire on the same chip, in order to isolate purely electrostatic and topographic contrast for comparison with the magnetic-tip map. However, we did not perform this control in the present work. The magnetic-tipped nanowires are equipped with tips that are several hundred nanometers long and are likely to contact the sample surface during scanning. The concern is not only surface contact, but also the risk that these long magnetic tips could break off during such scans. To safely implement this control, one would need a matched pair of nanowires, one magnetic and one non-magnetic, with equally long tips, allowing the same approach height to be maintained while minimizing the risk of tip damage.

12.2 Mapping the Phase-Separated State in Bilayer $EuGe_2$

We study phase separation in $EuGe_2$, a member of the REX_2 (RE = Eu, Gd; X = Si, Ge) family of 2D magnets, as a platform to probe magnetic phase competition. In $EuGe_2$, the interplay between localized 4f moments and conduction electrons in the Ge-like layers leads to indirect exchange interactions that are highly sensitive to structural dimensionality. As the number of layers is reduced, the balance between intralayer and interlayer coupling changes, allowing different magnetic phases to emerge or coexist. In few-layer films, the total magnetic moment remains below the value expected for full spin polarization, which suggests incomplete magnetic ordering or the coexistence of FM and AFM phases. Compared to related compounds, $EuGe_2$ offers distinct advantages for this study. It avoids the anionic vacancies common in GdX_2 and the pseudomorphic strain found in $EuSi_2$, making it structurally more stable. High-quality epitaxial films can be grown with precise thickness control and minimal disorder, enabling spatially resolved studies of the magnetic ground state.

We focus on bilayer $EuGe_2$ epitaxially grown on Ge and patterned into a rectangular bar, which provides well-defined edge crossings for the nanowire probe. Having a nonmagnetic contrast for reference is always convenient. The whole Ge chip and structure is covered with a 10 nm Pt layer to remove electrostatic effects during imaging. The 2ML thickness retains the 2D magnetic

character while avoiding the strong in-plane ferromagnetism of the monolayer. Imaging is carried out with NW 1, whose magnetically coated tip is well described by a monopole model.

Field-dependent images shown in Fig. 12.3 were acquired over $\mu_0 H = 0.1$ to 8 T at $T = 4.7$ K with a lift height of about 210 nm. With increasing field, the force gradient concentrates at the edges of the $EuGe_2$ bar. The color scale in the second row is enlarged by a factor of four to account for the increased signal. Crossing the sample edge (dashed orange lines) produces the characteristic dip-peak feature in f_+ expected from a uniformly out-of-plane magnetized region, consistent with the monopole model. Fig. 12.3b shows a spatial line cut averaged along the long edge of the bar, extracted from scans with the nanowire's softer mode oscillating along $\boldsymbol{a}_1$; the orthogonality of the two modes allows us to neglect f_{22} in this analysis. To quantify the out-of-plane stray field strength at the edge, we employ the monopole transfer function in $\mathbf{k}$-space to relate the measured force gradient to the sample stray field (Eq. (5.20)). After inverse Fourier transformation, we extract the local maxima and plot them as a function of the applied field in Fig. 12.3c. Some points exhibit systematic deviations that can be traced to uncertainties in the calibration of the lift height. For each field setting, the tip-sample distance is evaluated by approaching until the resonances broaden drastically or vanish. However, field-dependent drift requires repeated calibration, and at high fields the reduced nanowire Q makes it more difficult to determine the resonance broadening reliably. Despite these uncertainties, the extracted stray field increases monotonically and saturates just above $\mu_0 H = 2$ T, indicating progressive out-of-plane alignment of the $EuGe_2$ magnetization. At high field, the observed contrast closely matches simulations for a uniformly out-of-plane magnetized structure. No magnetic hysteresis is observed in the out-of-plane sweeps, consistent with a system dominated by in-plane FM/AFM competition. Our current probe does not apply in-plane fields, limiting access to in-plane switching or domain reconfiguration.

We map the 2ML $EuGe_2$ magnetic state around its transition at zero applied field and at a tip-sample distance of about 100 nm (Fig. 12.4). Fig 12.4a shows f_+ images with the corresponding dissipation in Fig. 12.4b. The dissipation Γ_+ is obtained from the combined inverse of the two oscillation amplitudes, normalized by the intrinsic damping of the nanowire modes; Γ_+ is formalized in Eq. 5.43. Above 20 K we observe non-magnetic contrast from electrostatic and van der Waals interactions reflecting the sample topography. Below 15 K, a granular structure forms above the $EuGe_2$ bar. The force gradient signal grows upon cooling, reaching a maximum at $T \approx 6.8$ K as seen in Fig. 12.4c, which plots the edge-averaged f_+ versus temperature. At lower temperatures (down to base 4.7 K), granular structure persists without a clear signature of static ferromagnetism. The dissipation maps (Fig. 12.4b) reveal no features above 15 K, but below this temperature elongated regions (hundreds of nm long, tens of nm wide) appear, densify, and strengthen upon cooling to 10 K. Further cooling reduces the dissipation contrast but does not fully extinguish it. Fig 12.4d shows the dissipation averaged within the dashed boundary versus

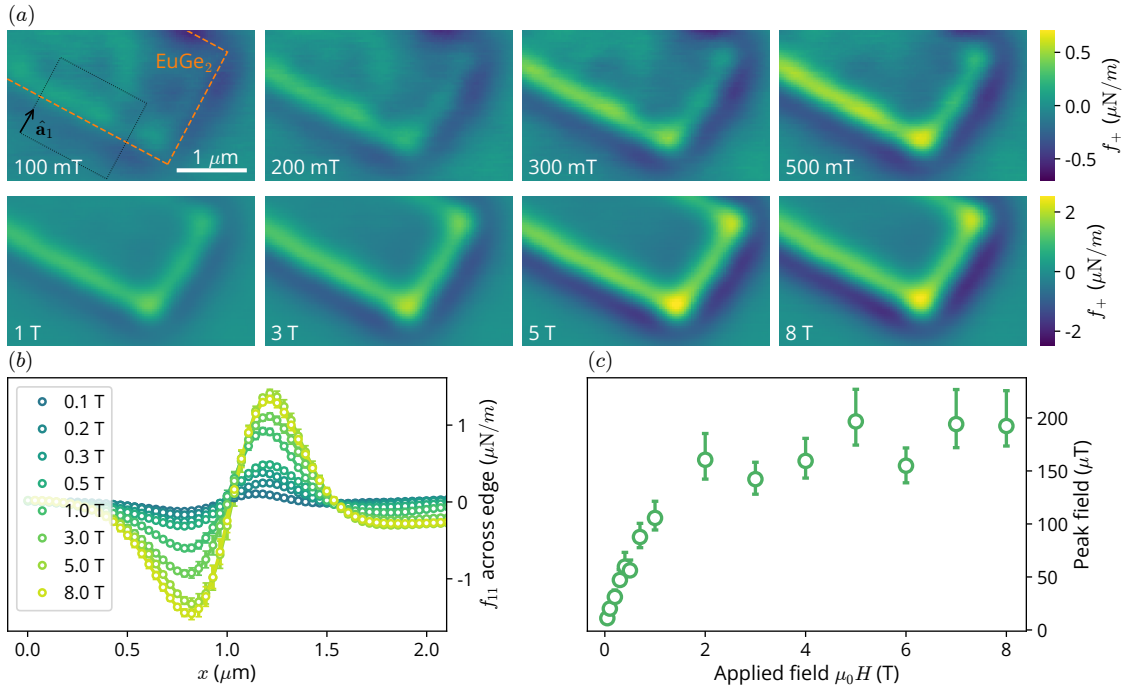

Fig. 12.3. Field dependence at 2ML $EuGe_2$ (4.7 K, about 210 nm lift height). **(a)** f_+ images for increasing $\mu_0 H$. Note the 4 times larger color scale in the second row. **(b)** Edge-averaged line cuts (black rectangle) with the soft mode oscillating along $\boldsymbol{a}_1$. The dashed orange line marks the bilayer edge. **(c)** Peak edge stray field at an effective 150 nm tip height, inferred via the monopole transfer function (Eq. (5.22)). Deviations reflect tip-sample distance calibration uncertainty; saturation occurs just above $\mu_0 H = 2$ T. For imaging, NW 1 was used. Adapted from [103].

temperature. While both f_+ and Γ_+ exhibit strong spatial variation with characteristic length scales of hundreds of nanometers, their local temperature dependencies do not vary significantly across the sample. Even when integrating over 100 nm-sized regions, f_+ and Γ_+ peak near 6.8 K and 9.8 K, respectively.

At zero applied field (as in Fig. 12.4), the nanowire tip's stray field propagating about 100 nm to the sample surface can reach up to about 45 mT (for a monopole at the apex) directly beneath the equilibrium tip position. This field locally perturbs the bilayer magnetization. Consequently, the nanowire measures not the intrinsic stray field gradient of $EuGe_2$ but the response of $EuGe_2$ to the perturbation. Thus, $f_+ \propto \mathrm{Re}(\chi_m)$ and $\Gamma_+ \propto \mathrm{Im}(\chi_m)$. This is supported by the lack of contrast reversal in f_+ upon flipping the tip magnetization: if we measured an ordinary stray field gradient, the effective monopole charge would change sign and the contrast would invert. In the tip-interaction (susceptibility) model, the monopole charge enters quadratically and no sign change occurs [50] (see also Sec. 5.5 and appendix C.2).

The spatial inhomogeneities in f_+ and Γ_+ indicate regions of distinct susceptibility within the 2ML $EuGe_2$. We associate higher-intensity regions with FM-like susceptibility and lower-intensity regions with AFM-like susceptibility. SQUID magnetometry in in-plane fields resolves hysteresis loops and saturation behavior. However, the saturation magnetization remains well below the expected $7\,\mu_B$/Eu. Values between 0.4 and $1.5\,\mu_B$/Eu are observed for 5–15 K [103], pointing to additional magnetic phases. In few-layer $EuGe_2$, shifts in hysteresis loops consistent with FM spin pinning by an AFM phase indicate an intrinsic exchange-bias effect [104].

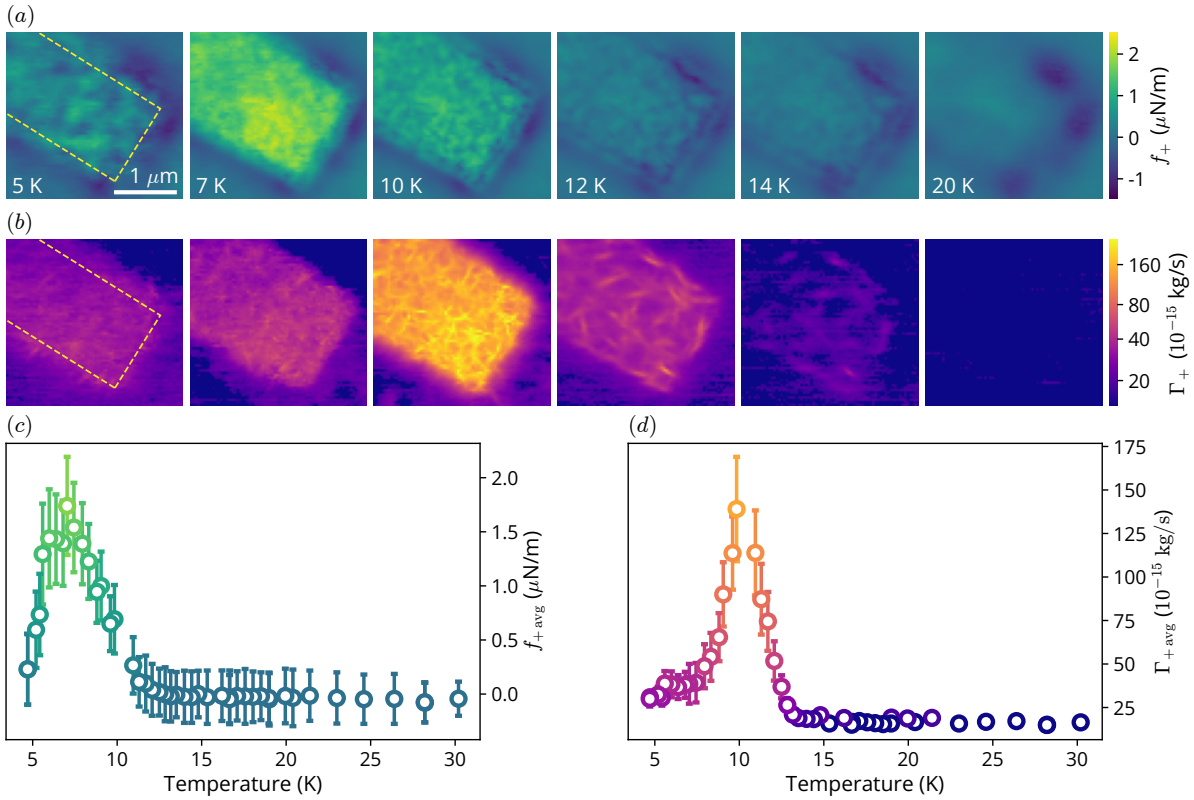

Fig. 12.4. Temperature evolution of the tip-sample interaction at 2ML $EuGe_2$ (zero field, about 100 nm lift height). **(a)** Combined force gradient f_+ from the two mode frequency shifts. **(b)** Corresponding combined dissipation Γ_+ from the oscillation amplitudes (nonlinear color scale). **(c)** Edge-averaged f_+ (dashed boundary identical for all temperatures) peaks at $T \approx 6.8$ K. **(d)** Edge-averaged Γ_+ peaks at $T \approx 10$ K. For imaging, NW 1 was used. Adapted from [103].

12.3 Distinction between Static and Dynamic Imaging Contrast

The distinction between static field gradient contrast and dynamic (susceptibility) contrast is clear in Fig. 12.5. In the left panels the tip magnetization points along $+\hat{\mathbf{z}}$, and in the right panels along $-\hat{\mathbf{z}}$. The $EuGe_2$ bilayer contrast (Fig. 12.5a) is essentially unchanged upon reversal, because the effective surface (monopole) charge contributes quadratically to the dynamic contrast formation (see Eq. (C.1)). By contrast, the static magnetic image of a current-carrying loop (Fig. 12.5b) inverts, since the signal depends linearly on the field gradient (see Eq. (5.20), where the surface charge keeps its sign.). These controls demonstrate that the bilayer maps at zero field primarily measure the magnetic susceptibility χ_m or non-linear dynamic effects not static stray fields.

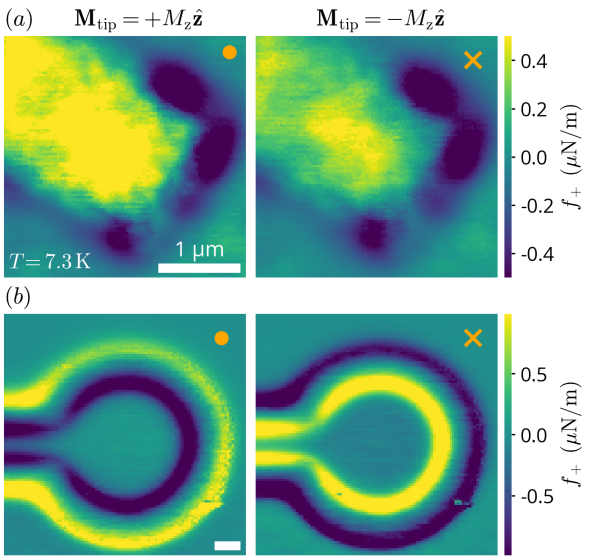

Fig. 12.5. Tip-magnetization reversal test. **(a)** f_+ maps at 2ML $EuGe_2$ (7.3 K, $\mu_0 H = 0$) with tip magnetization pointing out of the plane (left, orange dot) and into the plane (right, orange cross): the contrast is unchanged, consistent with a susceptibility signal. **(b)** Reference over a current-carrying lead ($I = 100$ μA) at $\mu_0 H = 0$ (left) and after tip reversal at $\mu_0 H = 60$ mT (right): the sign reverses as expected for a static field gradient signal. White horizontal scale bar: 1 μm (row-wise).

Conclusion

Magnetic force microscopy with a nanowire cantilever (NW-MFM) adapts conventional MFM by using just a nanowire as the cantilever. Unlike micro-cantilevers that oscillate approximately normal to the sample surface, the nanowire is mounted nearly perpendicular to the surface and oscillates laterally in the $(\hat{\mathbf{x}}, \hat{\mathbf{y}})$ sample plane. Owing to their high aspect ratio, nanowires are accurately described by Euler-Bernoulli beam theory combined with Zener viscoelastic damping (Chap. 3). The resulting dynamics reduce to damped harmonic oscillators. Because their cross section is nearly symmetric, both lateral stiffnesses must be considered. This symmetry yields two flexural modes with comparable resonance frequencies (typically 220–450 kHz for about 20 μm long nanowires) and, to good approximation, orthogonal oscillation directions (Chap. 4). Each mode senses the force gradient along its oscillation direction. The nanowire's low mass and high aspect ratio make it exceptionally compliant. We quantify this by fitting displacement-noise PSDs with linear-response theory using the fluctuation–dissipation theorem (Sec. 4.4). From these fits we obtain spring constants down to about 0.8×10^{-3} N/m (orders of magnitudes lower than those of commercial MFM cantilevers [105]) and force sensitivities down to $F_{\mathrm{min}} \approx 3\ \mathrm{aN\,Hz^{-1/2}}$ at about 12 K, surpassing typical micro-cantilevers.

While a *conventional* cantilever achieved $F_{\mathrm{min}} \approx 5.6\ \mathrm{aN\,Hz^{-1/2}}$ in Ref. [15] that device was thinned to about 60 nm thickness. Nanowires effectively realize this thinning in both lateral dimensions while retaining mechanical robustness. For magnetic imaging, we use Si nanowires (width: about 150 nm for NW 1 and about 110 nm for NW 2; length: about 20 μm) because of their high Q and availability [57]. A magnetic tip provides coupling to the sample's stray field. We fabricate long, slender Co tips by FEBID at the nanowire apex, targeting diameters down to 60 nm. The resulting shape anisotropy fixes the tip magnetization perpendicular to the surface along $\hat{\mathbf{z}}$ as the small diameter supports high spatial resolution down to 64 nm as demonstrated in Fig. 10.2. Additionally, the geometry motivates the monopole model introduced in Sec. 5.4, which treats the tip as a uniformly magnetized cylinder, and facilitates a simple qualitative signal interpretation. We validate the model against the Biot-Savart fields of a current-carrying wire and by tracking resonance frequency shifts under uniform magnetic fields provided by a superconducting coil applied along $\hat{\mathbf{z}}$ (Sec. 8.4). With a magnetic tip in place, each mode detects the magnetic force gradient along its oscillation direction. Combining the two mode signals yields $f_+ \propto \partial H_z/\partial z$, the gradient of the magetic field's out-of-plane component. The NW-MFM f_+ contrast is therefore directly comparable with the conventional MFM contrast while retaining the nanowire's superior force gradient sensitivity, provided both modes are addressed.

In NW-MFM the magnetic tip-sample interaction both produces the measurable signal (stronger tip magnetization increases sensitivity) and can perturb or even modify the sample's magnetic texture. This invasiveness is shared with conventional MFM and contrasts with minimally perturbative probes such as scanning SQUID or NV magnetometry. It can also be exploited [50, 103]. In our $Cr_2Ge_2Te_6$ and $EuGe_2$ imaging, the tip excites local magnetization dynamics governed by the sample's dynamic magnetic susceptibility (Sec. 1.3). We link this susceptibility to the observed mode-dependent frequency shifts and damping (Sec. 5.5).

The nanowire acts as a band-pass detector and narrow-band actuator. Sensitivity peaks at the mode resonances ($\omega_{1,2} \sim \omega_0$), and the drive excites magnetization dynamics near ω_0. When relaxation is fast ($\omega_0\tau \ll 1$), the response is quasi-static and predominantly in phase, appearing mainly in the frequency-derived f_+ with little dissipation Γ_+. When relaxation is slow ($\omega_0\tau \gg 1$), the response within the resonance band is weak in both channels unless nonlinear effects set in. Maximal dissipation arises near $\omega_0\tau \approx 1$, where Γ_+ peaks and f_+ varies most rapidly. Temperature and field tune $\tau(T, H)$ thus shift these response windows. In practice, decreasing temperature tends to slow DW dynamics, so τ may pass through the resonance band, producing strong, localized dissipation and contrast before moving beyond it at lower temperatures. Near T_C, critical slowing can similarly bring order-parameter fluctuations into the resonance band, consistent with the temperature-dependent contrast observed in $Cr_2Ge_2Te_6$ and $EuGe_2$.

At present, several technical challenges limit NW-MFM. Lateral oscillation geometry favors scanning near a sample edge to maintain optical access, which restricts sample layouts. Electrostatic forces couple strongly to the compliant nanowire and can mask magnetic signals (Fig. E.1); Au capping mitigates this but is not always applicable. Strong magnetic or electrostatic interactions can shift resonance frequencies by several kHz, far exceeding intrinsic linewidths and preventing stable PLL operation (Fig. D.4). Closely spaced mode frequencies exacerbate the issue, since large shifts may cause mode overlap and complicate interpretation. These aspects highlight that NW-MFM is not only highly sensitive but also inherently delicate, with boundaries set by force strength, electrostatics, and mode separation.

These limitations point to clear routes for improvement. Magnetic tip fabrication remains central: while FEBID Co tips are effective, further gains in spatial resolution may require shadow-evaporated ultra sharp tips or transfer of prefabricated tips. Nanowire engineering offers complementary benefits. Longer nanowires can ease the edge-scanning constraint, and alternative materials such as SiC or GaN, with higher quality factors [14, 106], could enhance force sensitivity. Reducing effective mass, for example by thinning or adopting hollow geometries, would further improve performance; nanotube-like probes are a plausible path toward ultra-low mass with adequate robustness.

We conclude that NW-MFM is sensitive to stray fields down to about 1.1 $\mathrm{nT\,Hz^{-1/2}}$ at around 12 K in multi-tesla applied fields, while providing sub-100 nm spatial resolution. We demonstrated its applicability as a complementary probe in Ref. [78] by imaging a surface state of $Cu_2O_2SeO_3$ and its helical ground state, and by investigating the temperature-dependent magnetization evolution of the 2D magnets $Cr_2Ge_2Te_6$ and $EuGe_2$ [103]. Taken together, these results show that NW-MFM has progressed beyond proof-of-principle and now functions as a measurement technique capable of addressing open questions in magnetism.

Appendix

A. Linear Response Theory

The frequency-dependent displacement of a nanowire under a small driving force and the response of a magnetic texture to a weak external field both involve dissipative processes. These can be described within the framework of linear response theory. In Kubo's formulation [107], the linear response of an observable to a weak perturbation is expressed through an equilibrium correlation function. In the frequency domain, this relation introduces the generalized susceptibility, or response function,

$$\chi(\omega) = \mathrm{Re}(\chi(\omega)) + i\,\mathrm{Im}(\chi(\omega)), \tag{A.1}$$

The real part $\mathrm{Re}(\chi)$ describes the reactive (elastic) response, and the imaginary part $\mathrm{Im}(\chi)$ encodes dissipation and determines energy absorption. The fluctuation-dissipation theorem (FDT) links spontaneous equilibrium fluctuations to the same susceptibility, thereby relating power spectral densities to $\mathrm{Im}(\chi)$. In the following, we derive the Kubo response formula and the FDT, which form the theoretical basis for interpreting dissipation and noise in these systems. For the derivation we use the book *Hydrodynamic Fluctuations, Broken Symmetry, and Correlation Functions* by D. Forster [108] and lecture notes by A. Tremblay, University of Sherbrooke, Canada [109].

A.1 From Perturbation to Response

We consider a system described by

$$\mathcal{H}(t) = \mathcal{H}_0 + \delta\mathcal{H}(t). \tag{A.2}$$

$\mathcal{H}_0$ is the time-independent equilibrium Hamiltonian, and $\delta\mathcal{H}(t)$ represents a small time-dependent perturbation. This perturbation originates from a weak variation in an external field $f(\mathbf{r}', t')$, which we decompose into a static background and a dynamic component:

$$f(\mathbf{r}', t') = f_0(\mathbf{r}') + \delta f(\mathbf{r}', t'). \tag{A.3}$$

The static background $f_0(\mathbf{r}')$ is already included in $\mathcal{H}_0$, while the perturbation $\delta\mathcal{H}(t)$ captures the influence of the small, time-dependent part $\delta f(\mathbf{r}', t')$, which couples linearly to an observable $A'(\mathbf{r}')$ via

$$\delta\mathcal{H}(t) = -\int d^3\mathbf{r}'\, A'(\mathbf{r}')\, \delta f(\mathbf{r}', t'). \tag{A.4}$$

Eq. (A.4) captures linear coupling to an external field, such as a force field coupling to a displacement or a magnetic field coupling to magnetization.
The statistical state of the system at time t is described by the density matrix

$$\rho(t) = \rho_0 + \delta\rho(t). \tag{A.5}$$

We assume $[\mathcal{H}_0, \rho_0] = 0$ as we set $\rho_0 = \rho(-\infty) = Z^{-1}e^{-\beta\mathcal{H}_0}$ with partition function $Z = \mathrm{Tr}(e^{-\beta\mathcal{H}_0})$, $\beta^{-1} = k_B T$, and Boltzmann constant k_B to be the thermal equilibrium state corresponding to $\mathcal{H}_0$.

To probe the system's response, let $A(\mathbf{r}, t)$ be a physical observable of interest. In a magnetic system, A could represent, while for a mechanical resonator (e.g. nanowire) it could denote the displacement. In the following, we aim to compute the response of this observable A to the external time-dependent perturbation. We define the change in its expectation value relative to thermal equilibrium as

$$\begin{aligned}
\delta\langle A(\mathbf{r}, t)\rangle &:= \langle A(\mathbf{r}, t)\rangle - \langle A(\mathbf{r}, t)\rangle_0 \\
&= \mathrm{Tr}(\rho(t)A(\mathbf{r})) - \mathrm{Tr}(\rho_0 A(\mathbf{r})) \\
&= \mathrm{Tr}((\rho_0 + \delta\rho(t))A(\mathbf{r})) - \mathrm{Tr}(\rho_0 A(\mathbf{r})) \\
&= \mathrm{Tr}(\delta\rho(t)A(\mathbf{r})).
\end{aligned} \tag{A.6}$$

To compute $\delta\langle A(\mathbf{r}, t)\rangle$, we determine how the deviation $\delta\rho(t)$ evolves over time under the influence of the perturbation. Its time evolution is governed by the Liouville-von Neumann equation:

$$\begin{aligned}
i\hbar\frac{\partial}{\partial t}\rho(t) &= [\mathcal{H}(t), \rho(t)] \\
i\hbar\frac{\partial}{\partial t}\delta\rho &= [\mathcal{H}_0, \rho_0] + [\mathcal{H}_0, \delta\rho] + [\delta\mathcal{H}, \rho_0] + [\delta\mathcal{H}, \delta\rho] \\
i\hbar\frac{\partial}{\partial t}\delta\rho &= [\mathcal{H}_0, \delta\rho] + [\delta\mathcal{H}, \rho_0]
\end{aligned} \tag{A.7}$$

which we expanded using Eq. (A.2), (A.5), neglecting $[\delta\mathcal{H}, \delta\rho]$. With the unitary time evolution operator $U_0(t) = e^{-i\mathcal{H}_0 t/\hbar}$ and its complex conjugate $U_0^\dagger(t) = e^{i\mathcal{H}_0 t/\hbar}$ we transform Eq. (A.7), rearrange and simplify to find

$$U_0^\dagger\, i\hbar\frac{\partial}{\partial t}\delta\rho\, U_0 = U_0^\dagger\left([\mathcal{H}_0, \delta\rho] + [\delta\mathcal{H}, \rho_0]\right) U_0 \tag{A.8}$$

$$i\hbar\frac{\partial}{\partial t}\left(U_0^\dagger\delta\rho\, U_0\right) = U_0^\dagger[\delta\mathcal{H}, \rho_0]\, U_0 \tag{A.9}$$

Integrating from $-\infty$ to t, we find:

$$\tilde{\rho}(t) = \frac{1}{i\hbar}\int_{-\infty}^{t} dt'\, U_0^\dagger(t')[\delta\mathcal{H}(t'), \rho_0]U_0(t').$$

Switching back to the Schrödinger picture, we obtain:

$$\delta\rho(t) = \frac{1}{i\hbar}\int_{-\infty}^{t} dt'\, U_0(t-t')[\delta\mathcal{H}(t'), \rho_0]U_0^\dagger(t-t'). \tag{A.10}$$

As we are interested in the observable $A(\mathbf{r}, t)$, we substitute Eq. (A.10) into Eq. (A.6). Using the cyclicity of the trace, we obtain

$$\delta\langle A(\mathbf{r}, t)\rangle = \frac{i}{\hbar}\int_{-\infty}^{t}\int \langle[A(\mathbf{r}, t), A'(\mathbf{r}', t')]\rangle_0\, \delta f(\mathbf{r}', t')\, d^3\mathbf{r}'\, dt' \tag{A.11}$$

$$\delta\langle A(\mathbf{r}, t)\rangle = \int_{-\infty}^{\infty}\int \chi_{AA'}(\mathbf{r}, t; \mathbf{r}', t')\, \delta f(\mathbf{r}', t')\, d^3\mathbf{r}'\, dt', \tag{A.12}$$

where we defined the causal response function

$$\chi_{AA'}(\mathbf{r}, t; \mathbf{r}', t') = \frac{i}{\hbar}\,\langle[A(\mathbf{r}, t), A'(\mathbf{r}', t')]\rangle_0\,\Theta(t-t') \tag{A.13}$$

and used the step function $\Theta(t)$ to enforce causality and extend the limits of integration to $-\infty$. Eqs. (A.12) and (A.13) are the general Kubo formula and the Kubo response function. $\chi_{AA'}$ is the system's response function. It specifies how the observable A reacts to a weak perturbation that couples to another observable A'. In the magnetic case, for example, A' would correspond to the magnetization component that couples directly to the applied magnetic field, while A denotes the component whose response is measured. χ is the magnetic susceptibility relating magnetization to the applied field. For a mechanical resonator, χ is the mechanical susceptibility that relates a displacement to a driving force. A' may represent the coordinate to which the external force couples, while A is the measured displacement. In many applications (e.g. nanowire), and in the next section, we focus on the case $A = A'$, where the susceptibility reduces to an auto-response function and can be directly linked to the observable's own equilibrium fluctuations. To quantify equilibrium fluctuations we introduce the time-domain correlation function,

$$C_{AA'}(r, t, r', t') = \langle A(r, t)A'(r', t')\rangle_0. \tag{A.14}$$

We will soon relate this correlation to measured spectra. For now we use it algebraically:

$$
\begin{aligned}
C_{A'A}(r',t',r,t) &= \langle A'(r',t')A(r,t)\rangle_0 && \text{(A.15)}\\
&= \mathrm{Tr}(\rho_0 A'(r',t')A(r,t)) && \text{(A.16)}\\
&= \mathrm{Tr}(\rho_0 A'(r',t')\,U_0^\dagger(t)A\,U_0(t)) && \text{(A.17)}\\
&= Z^{-1}\mathrm{Tr}(e^{-\beta H_0}A'(r',t')\,U_0^\dagger(t)A\,U_0(t)) && \text{(A.18)}\\
&= Z^{-1}\mathrm{Tr}(U_0^\dagger(t)A\,U_0(t)\,e^{-\beta H_0}A'(r',t')) && \text{(A.19)}\\
&= Z^{-1}\mathrm{Tr}(e^{-\beta H_0}\,e^{\beta H_0}U_0^\dagger(t)A\,U_0(t)\,e^{-\beta H_0}A'(r',t')) && \text{(A.20)}\\
&= Z^{-1}\mathrm{Tr}(e^{-\beta H_0}A(r,t-i\beta\hbar)A'(r',t')) && \text{(A.21)}\\
&= \langle A(r,t-i\beta\hbar)A'(r',t')\rangle_0 && \text{(A.22)}\\
&= C_{AA'}(r,t-i\beta\hbar,r',t'). && \text{(A.23)}
\end{aligned}
$$

Assuming time-translation invariance, we set $\tau = t - t'$, so that $C_{AA'}(\mathbf{r},t;\mathbf{r}',t') = C_{AA'}(\mathbf{r},\mathbf{r}';\tau)$. Then

$$
\begin{aligned}
\chi_{AA'}(\mathbf{r},\mathbf{r}',\tau) &= \frac{i}{\hbar}\left(\langle A(r,t)A'(r',t')\rangle_0 - \langle A'(r',t')A(r,t)\rangle_0\right)\,\Theta(t-t')\\
&= \frac{i}{\hbar}\left(C_{AA'}(\mathbf{r},t;\mathbf{r}',t') - C_{A'A}(\mathbf{r},t;\mathbf{r}',t')\right)\,\Theta(t-t')\\
&= \frac{i}{\hbar}\left(C_{AA'}(\mathbf{r},t;\mathbf{r}',t') - C_{AA'}(\mathbf{r},t-i\beta\hbar;\mathbf{r}',t')\right)\,\Theta(t-t')\\
&= \frac{i}{\hbar}\left(C_{AA'}(\mathbf{r},\mathbf{r}';\tau) - C_{AA'}(\mathbf{r},\mathbf{r}';\tau-i\beta\hbar)\right)\Theta(\tau). \qquad \text{(A.24)}
\end{aligned}
$$

Transforming to frequency space considering $\Theta(\tau) = 0$ for $\tau < 0$ (causality, however not limiting ω) gives

$$
\begin{aligned}
\chi_{AA'}(\omega) &= \frac{i}{\hbar}\int_0^\infty d\tau\, e^{i\omega\tau}\left[C_{AA'}(\tau) - C_{AA'}(\tau-i\beta\hbar)\right]\\
&= \frac{i}{\hbar}\left(1-e^{-\beta\hbar\omega}\right)\int_0^\infty d\tau\, e^{i\omega\tau}C_{AA'}(\tau). \qquad \text{(A.25)}
\end{aligned}
$$

Assuming $C^*_{AA'}(\tau) = C_{AA'}(-\tau)$ which holds for Hermitian observables A and A', the imaginary part of $\chi_{AA'}(\omega)$ can be expressed in terms of the Fourier transform of the correlation function:

$$
\begin{aligned}
\mathrm{Im}(\chi_{AA'}(\omega)) &= \frac{1}{2i}\left(\chi_{AA'}(\omega) - \chi^*_{AA'}(\omega)\right)\\
&= \frac{1}{2\hbar}\left(1-e^{-\beta\hbar\omega}\right)\int_0^\infty d\tau\left(e^{i\omega\tau}C_{AA'}(\tau) - e^{-i\omega\tau}C^*_{AA'}(\tau)\right)\\
&= \frac{1}{2\hbar}\left(1-e^{-\beta\hbar\omega}\right)2\int_0^\infty d\tau\mathrm{Re}\left(e^{i\omega\tau}C_{AA'}(\tau)\right)\\
&= \frac{1}{2\hbar}\left(1-e^{-\beta\hbar\omega}\right)\int_{-\infty}^\infty d\tau e^{i\omega\tau}C_{AA'}(\tau)\\
&= \frac{1}{2\hbar}\left(1-e^{-\beta\hbar\omega}\right)C_{AA'}(\omega). \qquad \text{(A.26)}
\end{aligned}
$$

Eq. (A.26) is the general FDT. It establishes a direct relation between the dissipative part of the linear response function, $\mathrm{Im}(\chi)$, and the equilibrium correlation spectrum, $C_{AA'}(\omega)$. It holds for arbitrary temperature and frequency, without approximation.

A.2 Auto-Correlation and Power Spectral Density

In the previous section, we introduced the time-translation invariant ($t = t'$) correlation function $C_{AA'}(\mathbf{r}, \mathbf{r}'; \tau)$ and showed that its frequency-domain version $C_{AA'}(\omega)$ enters $\mathrm{Im}(\chi_{AA'})$. Here we make the time-frequency correspondence explicit. We keep as single symbol $C_{AA'}$ and use the argument to indicate the domain: $C_{AA'}(\tau)$ in time, $C_{AA'}(\omega)$ in frequency. With that, the Fourier pair is

$$C_{AA'}(\mathbf{r}, \mathbf{r}'; \omega) = \int_{-\infty}^{\infty} e^{i\omega\tau} C_{AA'}(\mathbf{r}, \mathbf{r}'; \tau) d\tau, \quad C_{AA'}(\mathbf{r}, \mathbf{r}'; \tau) = \frac{1}{2\pi} \int_{-\infty}^{\infty} e^{-i\omega\tau} C_{AA'}(\mathbf{r}, \mathbf{r}'; \omega) d\omega. \tag{A.27}$$

Experimentally, $C_{AA'}(\omega)$ is a double-sided power spectral density [110], a spectrum. It specifies the fluctuation power per unit angular frequency (units per rad/s); equivalently, $C_{AA'}(\omega)d\omega$ gives the fluctuations contained in an infinitesimal interval around ω. With the Fourier convention in Eq. (A.27) and the definition in Eq. (A.14), we formulate the variance of an auto-correlation ($A = A'$) at coincident points ($\mathbf{r} = \mathbf{r}'$) at $\tau = 0$:

$$\langle |A(\mathbf{r}, \omega)|^2 \rangle = C_{AA}(\mathbf{r}) = \frac{1}{2\pi} \int_{-\infty}^{\infty} C_{AA}(\mathbf{r}, \omega) d\omega. \tag{A.28}$$

Assuming real observables, $C^*_{AA}(\omega) = C_{AA}(-\omega)$, it is convenient to fold the negative frequencies onto the positive axis and introduce the single-sided power spectral density (PSD) with $\omega > 0$,

$$S_A^{(\omega)}(\mathbf{r}, \omega) = 2\, C_{AA}(r, \omega), \quad \langle |A(\mathbf{r}, \omega)|^2 \rangle = \frac{1}{2\pi} \int_0^{\infty} S_A^{(\omega)}(\mathbf{r}, \omega) d\omega. \tag{A.29}$$

$S_A^{(\omega)}$ is the PSD of the observable A in terms of angular frequency ω, with units $[\mathrm{A}]^2/(\mathrm{rad/s})$. In our experiments, however, PSDs are reported as a function of ordinary frequency $\nu = \omega/(2\pi)$. To ensure consistency, we define

$$S_A^{(\nu)} d\nu = \frac{1}{2\pi} S_A^{(\omega)} d\omega, \quad \langle |A(\mathbf{r})|^2 \rangle = \int_0^{\infty} S_A^{\nu}(\nu) d\nu. \tag{A.30}$$

$S_A^{(\nu)}$ is the PSD of the observable A in terms of frequency ν, with units $[\mathrm{A}]^2/\mathrm{Hz}$. For notional simplicity, we omit the superscript and write $S_A(\nu)$ or just S_A with the understanding that PSDs are in this text always reported in terms of Hz. Note that under this convention, $S_A(\omega)$ likewise carries units $[\mathrm{A}]^2/\mathrm{Hz}$, it simply denotes the same per-Hz PSD evaluated at $\nu = \omega/2\pi$. We never use a per-rad/s definition in this text. We have thus established the Fourier pair for correlation functions and introduced the power spectral density $S_A(\mathbf{r}, \omega)$ as the experimentally accessible measure of fluctuations. In the following, we use these definitions to state the FDT.

A.3 Fluctuation Dissipation Theorem in the Classical Limit

The general FDT, Eq. (A.26), is exact and valid for arbitrary temperature and frequency. In the classical limit $|\beta\hbar\omega| \ll 1$, one expands $1 - e^{-\beta\hbar\omega} \approx \beta\hbar\omega$. Using the definitions of Sec. A.2, the theorem then reduces to a direct relation between the single-sided PSD and the dissipative part of the response function:

$$S_A(\mathbf{r},\omega) \;\approx\; \frac{4k_BT}{\omega}\,\mathrm{Im}(\chi_{AA}(\mathbf{r},\omega))\,. \tag{A.31}$$

This classical form of the FDT provides the link used in the experiment. It connects measured thermal noise spectra (displacement-noise PSDs) to the dissipative response (damping).

B. Magnetic Contrast from a Monopole

B.1 Expected Stray Fields for Uniform In- and Out-of-Plane Magnetized Layers

Depending on the orientation of magnetization stray field and consequently also stray field gradients differ. With regard to that Fig. B.1 can be helpful to quickly determine if the measured NW-MFM signal derives from a uniformly in- or out-of-plane magnetized layer. In this text we exclusively work with magnetic tips of strong out-of-plane magnetization, thus we do not have to concern ourselves with second derivatives of stray field.

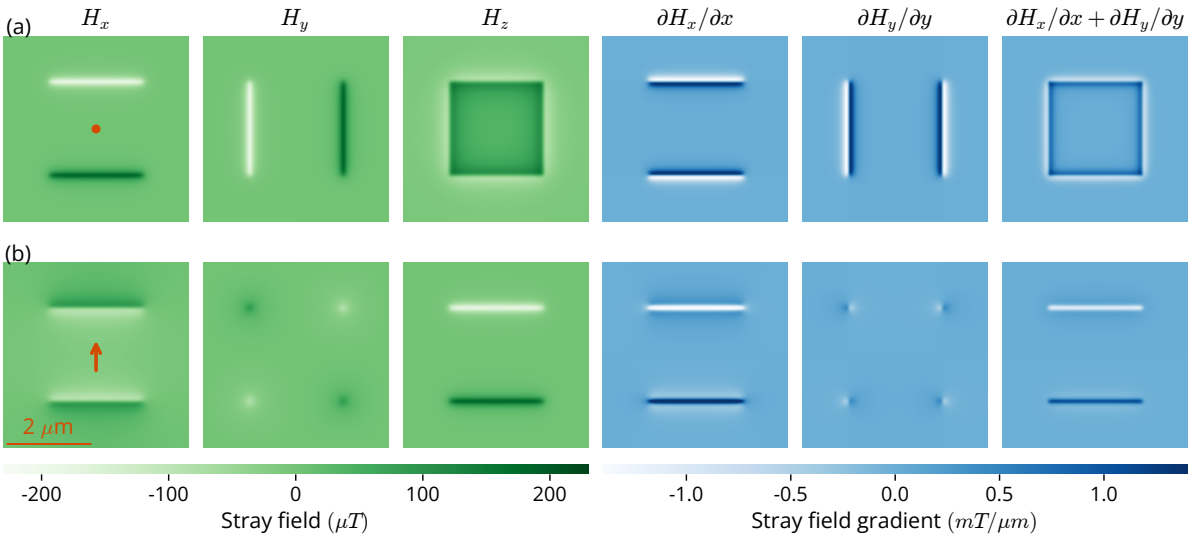

Fig. B.1. Magnetic stray field and field gradients expected for a uniformly magnetized square-shaped layer with (a) out-of-plane magnetization, denoted by the red dot and (b) in-plane magnetization denoted by the red arrow. The components of the stray field $\mathbf{H} = (H_x, H_y, H_z)$ are displayed using a green color scale. The stray field gradients are displayed with a blue color code. The gradient $\partial H_z/\partial z = -\partial H_x/\partial x - \partial H_x/\partial x$. Note that the shown field gradients are most relevant for NW-MFM with a uniformly magnetized tip along $\hat{\mathbf{z}}$.

C. Magnetic Symmetry of a Cylindrical Magnetic Tip

C.1 Potential Gradients

On the symmetry axis ($x = y = 0$) of a semi-infinite magnetic cylinder that is axisymmetric about $\hat{\mathbf{z}}$, the stray field is purely axial, $\mathbf{H}^{\circ}_{\text{tip}} = (0, 0, H^{\circ}_{\text{tip},z})$; off-axis, transverse components exist but are antisymmetric and cancel in (x, y)-plane integrals. See Fig. C.1, which shows the scalar potential and its gradients, exhibiting the same rotational symmetry and odd/even parity underlying this cancellation.

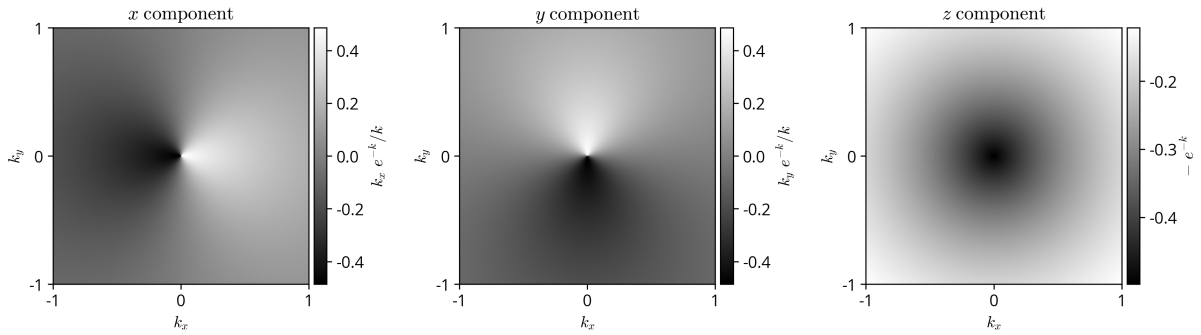

Fig. C.1. Spatial gradients of the magnetic potential of a semi-infinite cylindrical with magnetization oriented along its longitudinal axis $\hat{\mathbf{z}}$. (a) The gradients along $\hat{\mathbf{x}}$ and (b) $\hat{\mathbf{y}}$ are odd functions that vanish when integrating over all space. (c) Gradient along $\hat{\mathbf{z}}$ is an even function. Tip-sample surface distance was set to 1 (arb. units), also the constant prefactor from Eq. (5.24) is set to 1.

C.2 Interaction of a Monopole with a Locally Homogeneous Film

The structure of $\mathbf{K}_{\mathrm{mag}}$ in Eq. (5.38) partly depends on the magnetic tip model. For a monopole (and likewise for a vertical dipole oriented along $\hat{\mathbf{z}}$), the scalar potential at the film plane is rotational symmetric about $\mathbf{r}_0$ (cf. Fig. C.1), so the $\mathbf{k}$-space weight is isotropic, i.e. it only depends on $k = |\mathbf{k}|$.

Here, we consider the monopole tip. However, for a vertical dipole along $\hat{\mathbf{z}}$, the formulas below are recovered by an extra factor of k in the integral, the symmetry arguments are unchanged. Working with the magnetic point charge q_{tip}, the diagonal elements ($j = 1, 2$) of $\mathbf{K}_{\mathrm{mag}}$ are

$$K_{\mathrm{mag},jj}(\omega) = -\frac{i\,\mu_0\, q_{\mathrm{tip}}^2}{16\pi^2} \int e^{-2kz_\sigma}\, e^{i\mathbf{k}\cdot\mathbf{r}}\, T_{jj}(\mathbf{k},\omega) d^2k. \tag{C.1}$$

In Eq. (C.1) we made use of the fact that both the perturbing field, that drives the magnetization and the effective surface that establishes stray field sensitivity are proportional to q_{tip}. As q_{tip} does not depend on k_x nor k_y, we could pull it out of the integral. We explicitly see in Eq. (C.1) that $K_{\mathrm{mag},jj}(\omega) \propto q_{\mathrm{tip}}$. For our imaging this means that susceptiblity contrast is independent of $\mathrm{sign}(q_{\mathrm{tip}})$. To analyze Eq. (C.1) further we defined $T_{jj} = \mathrm{Re}(T_{jj}) + i\,\mathrm{Im}(T_{jj})$ with explicit real

and imaginary parts,

$$\begin{aligned}\mathrm{Re}\,(T_{11}) = &\ \frac{k_x^4}{k^2}\,\mathrm{Im}(\chi_{xx}) + \frac{k_x^3 k_y}{k^2}\,\mathrm{Im}\,(\chi_{xy}{+}\chi_{yx}) + \frac{k_x^2 k_y^2}{k^2}\,\mathrm{Im}(\chi_{yy}) - \ k_x^2\,\mathrm{Im}(\chi_{zz}) \\ &+ \frac{k_x^3}{k}\,\mathrm{Re}(\chi_{xz}) + \frac{k_x^2 k_y}{k}\,\mathrm{Re}(\chi_{yz}) + \frac{k_x^3}{k}\,\mathrm{Re}(\chi_{zx}) + \frac{k_x^2 k_y}{k}\,\mathrm{Re}(\chi_{zy}), \qquad \text{(C.2)}\end{aligned}$$

$$\begin{aligned}\mathrm{Im}\,(T_{11}) = &\ -\frac{k_x^4}{k^2}\,\mathrm{Re}(\chi_{xx}) - \frac{k_x^3 k_y}{k^2}\,\mathrm{Re}\,(\chi_{xy}{+}\chi_{yx}) - \frac{k_x^2 k_y^2}{k^2}\,\mathrm{Re}(\chi_{yy}) + \ k_x^2\,\mathrm{Re}(\chi_{zz}) \\ &+ \frac{k_x^3}{k}\,\mathrm{Im}(\chi_{xz}) + \frac{k_x^2 k_y}{k}\,\mathrm{Im}(\chi_{yz}) + \frac{k_x^3}{k}\,\mathrm{Im}(\chi_{zx}) + \frac{k_x^2 k_y}{k}\,\mathrm{Im}(\chi_{zy}). \qquad \text{(C.3)}\end{aligned}$$

$$\begin{aligned}\mathrm{Re}\,(T_{22}) = &\ \frac{k_x^2 k_y^2}{k^2}\,\mathrm{Im}(\chi_{xx}) + \frac{k_x k_y^3}{k^2}\,\mathrm{Im}\,(\chi_{xy}{+}\chi_{yx}) + \frac{k_y^4}{k^2}\,\mathrm{Im}(\chi_{yy}) - \ k_y^2\,\mathrm{Im}(\chi_{zz}) \\ &+ \frac{k_x k_y^2}{k}\,\mathrm{Re}(\chi_{xz}) + \frac{k_y^3}{k}\,\mathrm{Re}(\chi_{yz}) + \frac{k_x k_y^2}{k}\,\mathrm{Re}(\chi_{zx}) + \frac{k_y^3}{k}\,\mathrm{Re}(\chi_{zy}), \qquad \text{(C.4)}\end{aligned}$$

$$\begin{aligned}\mathrm{Im}\,(T_{22}) = &\ -\frac{k_x^2 k_y^2}{k^2}\,\mathrm{Re}(\chi_{xx}) - \frac{k_x k_y^3}{k^2}\,\mathrm{Re}\,(\chi_{xy}{+}\chi_{yx}) - \frac{k_y^4}{k^2}\,\mathrm{Re}(\chi_{yy}) + \ k_y^2\,\mathrm{Re}(\chi_{zz}) \\ &+ \frac{k_x k_y^2}{k}\,\mathrm{Im}(\chi_{xz}) + \frac{k_y^3}{k}\,\mathrm{Im}(\chi_{yz}) + \frac{k_x k_y^2}{k}\,\mathrm{Im}(\chi_{zx}) + \frac{k_y^3}{k}\,\mathrm{Im}(\chi_{zy}). \qquad \text{(C.5)}\end{aligned}$$

Under the integration in Eq. (C.1) terms proportional to $k_x^m k_y^n$ with $m{+}n$ odd (the second lines in eqs. (C.2)-(C.5)) vanish when evaluated at $\mathbf{r} = \mathbf{r_0}$, provided the film is locally homogeneous so that $\chi_m(\mathbf{k},\omega) = \chi_m(-\mathbf{k},\omega)$ with no $\mathbf{k}$-mixing.[1] The even terms remain.

$$\mathrm{Re}(T_{11})\Big|_{\text{even}} = \frac{k_x^4}{k^2}\,\mathrm{Im}(\chi_{xx}) + \frac{k_x^3 k_y}{k^2}\,\mathrm{Im}(\chi_{xy}{+}\chi_{yx}) + \frac{k_x^2 k_y^2}{k^2}\,\mathrm{Im}(\chi_{yy}) - \ k_x^2\,\mathrm{Im}(\chi_{zz}), \qquad \text{(C.6)}$$

$$\mathrm{Im}(T_{11})\Big|_{\text{even}} = -\frac{k_x^4}{k^2}\,\mathrm{Re}(\chi_{xx}) - \frac{k_x^3 k_y}{k^2}\,\mathrm{Re}(\chi_{xy}{+}\chi_{yx}) - \frac{k_x^2 k_y^2}{k^2}\,\mathrm{Re}(\chi_{yy}) + \ k_x^2\,\mathrm{Re}(\chi_{zz}). \qquad \text{(C.7)}$$

$$\mathrm{Re}(T_{22})\Big|_{\text{even}} = \frac{k_x^2 k_y^2}{k^2}\,\mathrm{Im}(\chi_{xx}) + \frac{k_x k_y^3}{k^2}\,\mathrm{Im}(\chi_{xy}{+}\chi_{yx}) + \frac{k_y^4}{k^2}\,\mathrm{Im}(\chi_{yy}) - \ k_y^2\,\mathrm{Im}(\chi_{zz}), \qquad \text{(C.8)}$$

$$\mathrm{Im}(T_{22})\Big|_{\text{even}} = -\frac{k_x^2 k_y^2}{k^2}\,\mathrm{Re}(\chi_{xx}) - \frac{k_x k_y^3}{k^2}\,\mathrm{Re}(\chi_{xy}{+}\chi_{yx}) - \frac{k_y^4}{k^2}\,\mathrm{Re}(\chi_{yy}) + \ k_y^2\,\mathrm{Re}(\chi_{zz}). \qquad \text{(C.9)}$$

We notice in eqs. (C.6) - (C.9) that, for the even (surviving) contributions, $\mathrm{Re}(T_{ii})$ depends only on $\mathrm{Im}(\chi_m)$, whereas $\mathrm{Im}(T_{ii})$ depends only on $\mathrm{Re}(\chi_m)$. Because of the overall factor i in Eq. (C.1), the real part of $K_{\mathrm{mag},jj}$ depends on the real parts of the susceptibility, while the imaginary part depends on imaginary parts of the magnetic susceptibility elements.

[1] If these conditions are violated (e.g. tilted/non-radial tip magnetization, domain walls/edges, or nonlocal/chiral $\mathbf{k}$-odd response), odd terms may survive.

D. Additional Imaging

D.1 Helical State of $Cu_2O_2SeO_3$ After Field Polarization

After field polarization (FP), the in-plane helix in $Cu_2O_2SeO_3$ re-emerges in selected regions. Its re-entrance is signaled by the nucleation and progressive opening of the characteristic channels that host the helical modulations. This recovery is already visible at positive field after FP at 500 mT (Fig. D.1); as the field is reduced toward zero, the in-plane helical channel broadens and extends. Intersections between two orthogonal in-plane helical domains are also observed (Fig. D.2). Interestingly, upon increasing the field the in-plane helical texture retracts from the sample edge (top of the images).

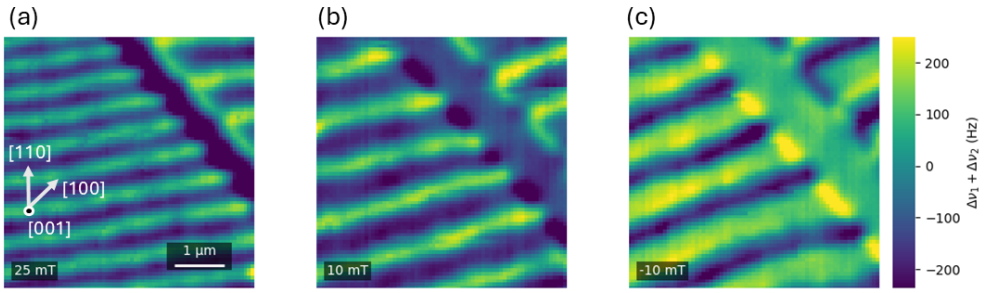

Fig. D.1. Reappearance of the helical state on the (001) surface of $Cu_2O_2SeO_3$ after polarizing the sample at 500 mT, adapted from Ref. [78]. (a) Surface state with a diagonal channel along [010] that hosts in-plane helical modulations. (b) Same area with extended channel. (c) Change in surface state contrast.

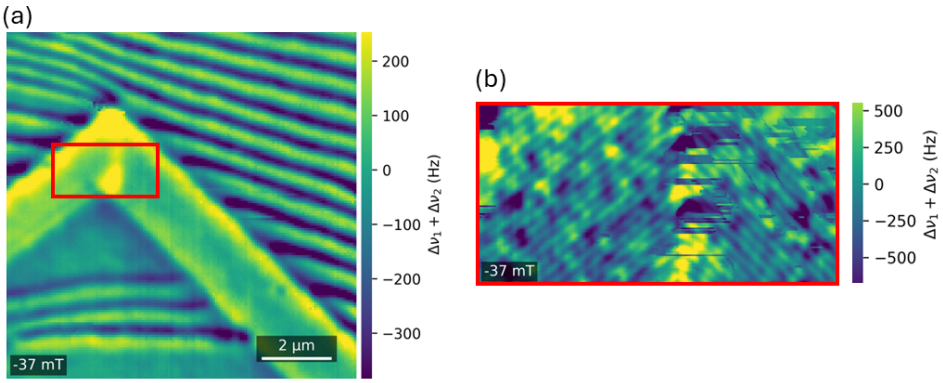

Fig. D.2. Helical state on the (001) surface of $Cu_2O_2SeO_3$ propagating along [100] and [010], adapted from Ref. [78]. (a) Overview map showing surface state stripes and two diagonal channels that intersect. (b) High resolution view of the junction showing in-plane helical modulations with $\mathbf{q} \parallel [100]$ and $\mathbf{q} \parallel [010]$.

D.2 Bilayer $EuGe_2$ at Elevated Temperature

Comparison of MFM images of 2ML $EuGe_2$ at 4.7 K and 45 K (46 K) confirms that the contrast observed at base temperature is magnetic in origin. This becomes evident when comparing Fig. D.3(a) and (b). At 4.7 K the signal amplitude is larger, indicating stronger force gradients, but the images appear blurrier with lower spatial resolution. By contrast, at 45-46 K the sample is well above the transition temperature and only topographic contrast remains. The signal is weaker but the spatial resolution is higher. Notably, even above the transition temperature the Eu spins remain field-susceptible. Applying an out-of-plane field aligns them and restores measurable contrast.

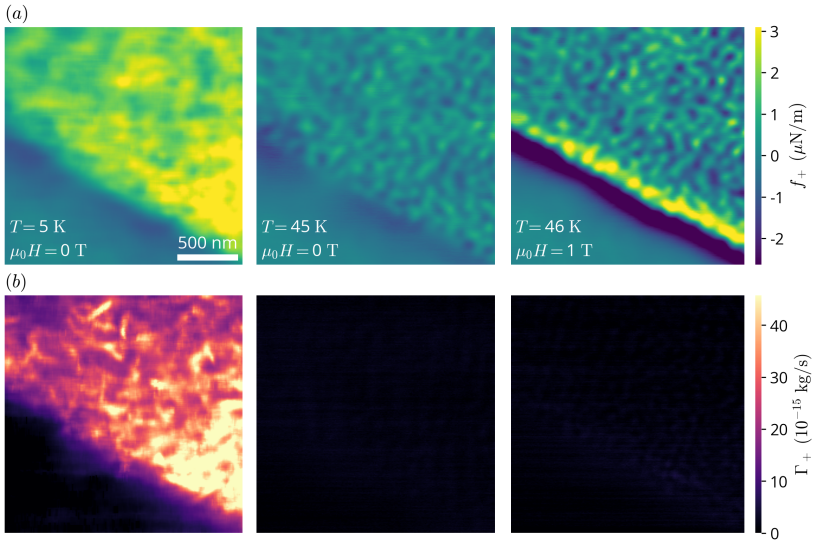

Fig. D.3. Comparison of 2ML $EuGe_2$ at low and high temperature. (a) Force gradient maps at (left to right) 5 K, 0 T; 45 K, 0 T; and 46 K under an out-of-plane field of $\mu_0 H = 1$ T. (b) Corresponding dissipation maps under the same conditions. White scale bar: 500 nm (applies to all panels).

D.3 Huge Force and Force Gradients Above $EuFe_2(As_{0.79}P_{0.21})_2$

During imaging of the superconducting FM $EuFe_2(As_{0.79}P_{0.21})_2$ [95], the nanowire sensor (NW 1) experienced extreme force gradients that shifted its resonance frequencies by several kHz. With an already small mode splitting of about 520 Hz, PLL operation could not be maintained. We therefore recorded displacement-noise PSDs and extracted the resonance frequencies from the spectra. Each spectrum required about 15 s, and even with modest pixel sizes a single image took hours to acquire. I just want to show a few of these images in Fig. D.4 and Fig. D.5 since they took so long to acquire. The first series (Fig. D.4) tracks the evolution of the domain Meissner state (DMS) after ZFC when applying field. the second series (Fig. D.5) tracks the DMS after field polarization. In Fig. D.6 we show how upon further cooling to the domain vortex state (DVS), tip-surface forces grow so large that they lead to static nanowire deflection.

In the DMS regime at 19.8 K after ZFC, defined by minimizing superconducting vortices to about one per $10\,\mu\text{m} \times 10\,\mu\text{m}$ (about 1 mT), only ferromagnetic domains are visible in Fig. D.4. At 7 mT, vortices begin to populate the field of view, predominantly at Y-shaped defects of the domain structure. As the field increases further, the domain configuration reorganizes. At about 75 mT, the stripe domains tend to align nearly vertically, likely due to a small in-plane component of the applied field from a slight sample tilt. At the same time, up-polarity domains broaden while down-polarity domains narrow, which increases the overall period. At higher fields

the density of vortices with the up-polarity becomes so large that individual cores are no longer resolved. Dark stripes fragment into shorter segments and then isolated bubbles. Above about 400 mT the FM is saturated and the domain contrast is no longer visible. Any residual signal in this state likely reflects surface topography and stray fields from steps and edges.

When the field is decreased in Fig. D.5, down-polarity domains reappear via the penetration of magnetic bubbles. With further reduction of the field, bubbles form chains and then fuse into continuous dark stripes. Near zero applied field (about +5 to −10 mT), the very short-period DMS is restored and is decorated by small numbers of uncorrelated vortices and antivortices. Around −5 to −10 mT we observe a single chain of discrete dark antivortices within the same down domain. This chain then merges into a nearly featureless, high frequency shift stripe, which we interpret as a densely packed train of closely spaced antivortices bound by short-range attraction. As the field is decreased further toward negative saturation, the behavior mirrors the positive-field side: light up regions become minority domains, shrink, and break into bubbles.

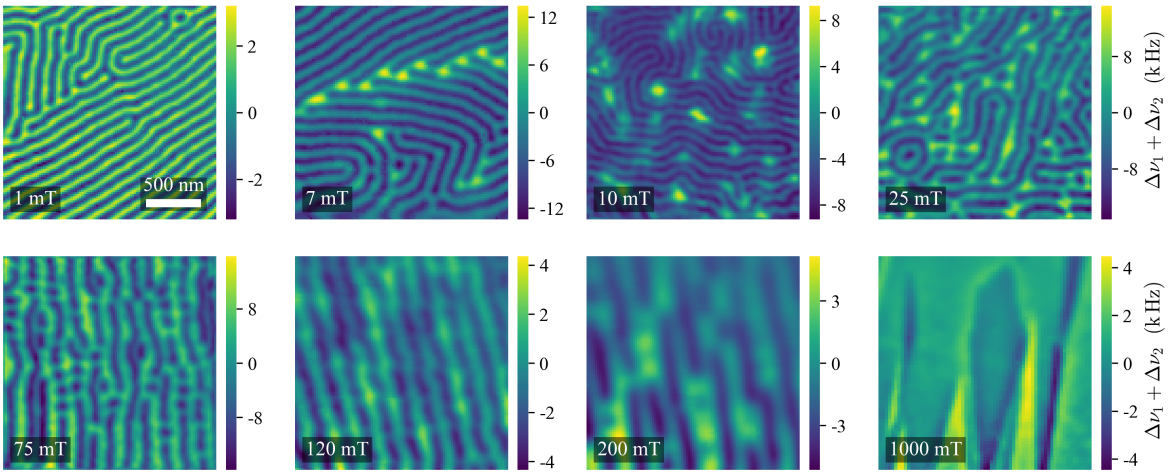

Fig. D.4. Imaging at increasing field after ZFC the DMS of $EuFe_2(As_{0.79}P_{0.21})_2$ at 19.8 K. Adapted from Ref. [95]. Imaging involved the acquisition of displacement-noise PSDs and resonance frequency extraction.

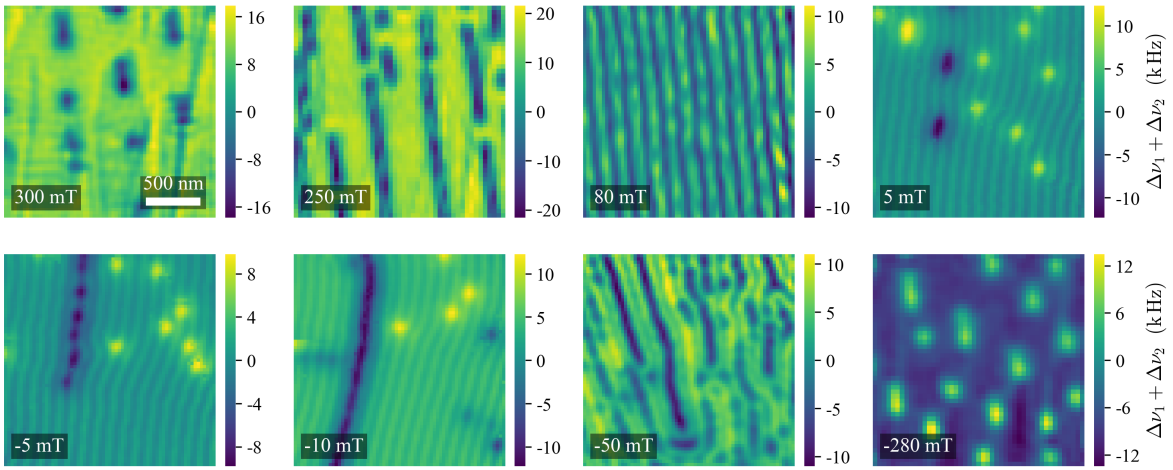

Fig. D.5. Imaging of $EuFe_2(As_{0.79}P_{0.21})_2$ at 19.8 K after field polarization. Adapted from Ref. [95]. Imaging involved the acquisition of displacement-noise PSDs and resonance frequency extraction.

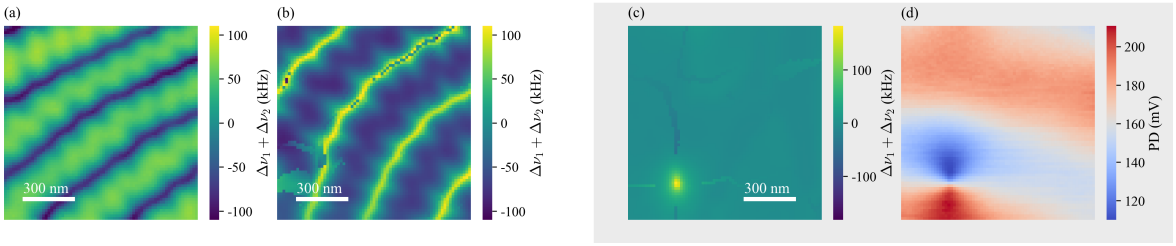

Fig. D.6. Image distortions due to static nanowire deflection from large forces between $EuFe_2(As_{0.79}P_{0.21})_2$ and nanowire in the DVS at about 4.3 K. (a) Frequency shift image after ZFC with the tip magnetization $\mathbf{M}+ \approx M_z\hat{\mathbf{z}}$ and (b) after ZFC with $\mathbf{M} \approx -M_z\hat{\mathbf{z}}$. (c) Frequency shift image of a magnetic bubble at 740 mT taken at about 40 nm lift of height and (d) corresponding photoreceiver signal connected to the nanowire position in the optical detection focus. The imaging region is contained in the imaging region of figs. D.4 and D.5.

D.4 Current Limit on Scannable Area

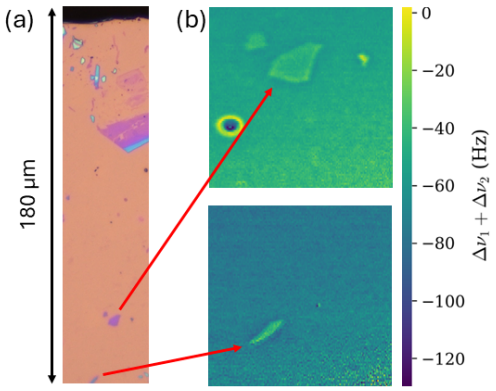

Fig. D.7. Current imaging reach from a sample edge using a 20 μm nanowire probe. (a) Optical micrograph of a sample. The sample edge (black) runs along the top. Red arrows mark the locations tested in (b). (b) Nanowire frequency shift image recorded at the marked positions, demonstrating that stable imaging remains feasible several tens of μm inside from the edge.

E. Electrostatics

E.1 Electrostatic Spring Constant Change

We consider a general mechanical resonator with unit displacement direction $\hat{\mathbf{w}}$. The $\hat{\mathbf{z}}$ direction corresponds to a conventional cantilever oscillating normal to a sample's surface. The $\hat{\mathbf{x}}$ and $\hat{\mathbf{y}}$ directions correspond to the laterally oscillating nanowire. Modes 1 and 2 of the nanowire lie along $\hat{\mathbf{x}}$ and $\hat{\mathbf{y}}$, respectively. The math for mode 1 and mode 2 is analogous. Let $\mathbf{R} = (x, y, z)$. Let $C = C(\mathbf{R})$. Let $V = V(\mathbf{R})$ denote an electrostatic potential difference. The electrostatic energy is $E_{\mathrm{el}} = C\,V^2/2$. All spatial derivatives act with respect to $\mathbf{R}$. The curvature of E_{el} modifies the spring constant of each mode with

$$k_{\mathrm{el}} = \hat{\mathbf{w}}^\top \left(\nabla\nabla E_{\mathrm{el}}\right) \hat{\mathbf{w}} = \tfrac{1}{2}\, V^2\, \hat{\mathbf{w}}^\top (\nabla\nabla C)\, \hat{\mathbf{w}} + 2\, V\, \left(\nabla C \cdot \hat{\mathbf{w}}\right)\left(\nabla V \cdot \hat{\mathbf{w}}\right) + C\left[\left(\nabla V \cdot \hat{\mathbf{w}}\right)^2 + V\, \hat{\mathbf{w}}^\top (\nabla\nabla V)\, \hat{\mathbf{w}}\right]. \tag{E.1}$$

For the cantilever mode along $\hat{\mathbf{z}}$ with $\partial V/\partial z = 0$:

$$k_{\mathrm{el},z} = \tfrac{1}{2}\, V^2\, \frac{\partial^2 C}{\partial z^2}. \tag{E.2}$$

For the nanowire mode 1 along $\hat{\mathbf{x}}$ (analogue for mode 2 along $\hat{\mathbf{y}}$ at fixed z:

$$k_{\mathrm{el},1} = \tfrac{1}{2}\, V^2\, \frac{\partial^2 C}{\partial x^2} + 2\, V\, \frac{\partial C}{\partial x}\, \frac{\partial V}{\partial x} + C \left[\left(\frac{\partial V}{\partial x} \right)^2 + V\, \frac{\partial^2 V}{\partial x^2} \right]. \tag{E.3}$$

The difference in Eqs. (E.2) and (E.3) comes from the assumption that the derivative of V along $\hat{\mathbf{z}}$ vanishes, whereas laterally it does not.

Experimentally, the potential difference depends on the contact potential difference between tip and sample, V_{CPD}, a voltage bias term V_b, and possibly on the applied field $\mu_0 H$ if some magneto-electric effect is present, V_{ME}, is present in the sample. We define

$$V(\mathbf{R}, H) = V_{\mathrm{CPD}}(\mathbf{R}) + V_{\mathrm{ME}}(\mathbf{R}, H) - V_b. \tag{E.4}$$

If we assume a spatially uniform V_b, then the V-derivative terms in Eq. (E.3) only depend on $V_{\mathrm{CPD}} + V_{\mathrm{ME}}$.

E.2 Electrostatic Effects at $Cu_2O_2SeO_3$

Without an Au layer on the $Cu_2O_2SeO_3$ crystal, approaching the surface for MFM is difficult. Strong electrostatic contrast dominates the signal and prevents close approach. As shown in Fig. E.1(a,b), images taken at opposite fields, +30 mT and −30 mT, are dominated by such contrast. In an attempt to find magnetic signal, we consider the difference, $\Delta\nu_1(30\,\mathrm{mT}) - \Delta\widetilde{\nu}_1(-30\,\mathrm{mT})$, shown in Fig. E.1(c). This subtraction tends to suppress components that are even in field and emphasize the odd-in-field response expected for magnetic contributions. However, neither the magnetic state nor the electrostatic landscape need be strictly even/odd under $H \to -H$ (e.g. due to hysteresis, chirality, or field-dependent charging), so residual nonmagnetic features can remain. The field dependence in Fig. E.2 follows from Eqs. (E.3) and (E.4) with $V_b = 0$. At $H = 0$ the magnetoelectric contribution is small because the helical texture averages

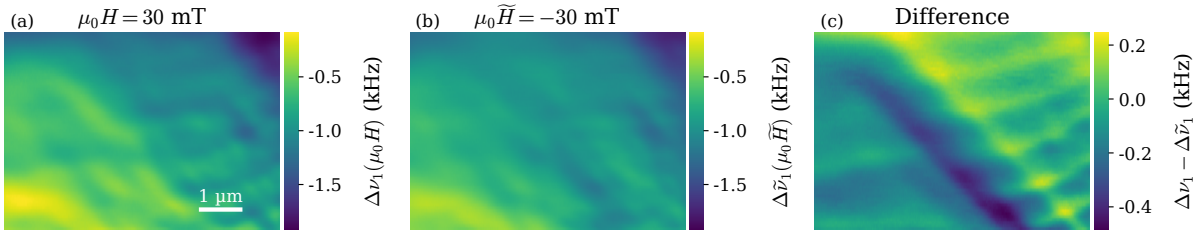

Fig. E.1. Imaging of $Cu_2O_2SeO_3$ without Au capping at 5 K. (a,b) MFM images of the same region at external fields $\mu_0 H = +30$ and $\mu_0 \widetilde{H} = -30$ mT, respectively. Strong electrostatics do not allow to determine a proper tip-sample distance measurement. (c) Only the difference image, $\nu_1(\mu_0 H) - \Delta\widetilde{\nu}_1(\mu_0 \widetilde{H})$, reveals some modulation.

the polarization, and we take V_{ME} to be loosely proportional to the sample polarization P. Thus, $V(0) \approx V_{\mathrm{CPD}}$. Because the nanowire is parked close to a crystal edge, the edge-induced capacitance curvature together with the lateral gradients and curvature of V produce a stiffnening (frequency increase) above the dashed baseline even at a tip-sample spacing of about 5 μm. As the field increases to ward the helical-to-conical transition the magnetoelectric term turns on with a sign that partially cancels the local CPD at the measurement point, which reduces both V and its lateral curvature and brings $\nu_1(H)$ to a shallow minimum. This minimum near 60 mT coincides with the magnetoelectric peak reported in [111]. At higher field the projected polarization reverses sign and grows in magnitude for this orientation, so V_{ME} adds to V_{CPD}, the lateral potential landscape steepens near the edge, and the stiffening reaches a pronounced maximum around 120-140 mT with an upshift of about 30 kHz relative to the dashed line. With still higher field the texture approaches the field-polarized state, the polarization and V_{ME} diminish, and $\nu_1(H)$ returns toward the CPD baseline.

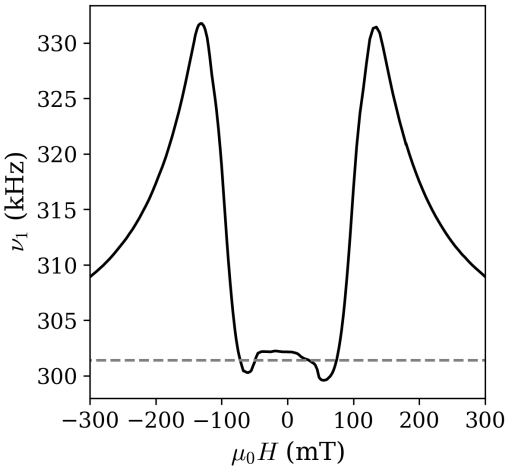

Fig. E.2. Field-dependent electrostatic interaction between $Cu_2O_2SeO_3$ and the nanowire at 5 K. Resonance frequency (first mode) versus external field $\mu_0 H$ at a tip-sample spacing of approximately 5 μm. The dashed grey line indicates the unperturbed resonance frequency.

Bibliography

[1] Estefani Marchiori, Lorenzo Ceccarelli, Nicola Rossi, Luca Lorenzelli, Christian L. Degen, and Martino Poggio. "Nanoscale magnetic field imaging for 2D materials". In: *Nature Reviews Physics* 4.1 (Jan. 1, 2022), pp. 49–60. DOI: 10.1038/s42254-021-00380-9 (cited on p. 1).

[2] Nissim Amos, Rabee Ikkawi, Robert Haddon, Dmitri Litvinov, and Sakhrat Khizroev. "Controlling multidomain states to enable sub-10-nm magnetic force microscopy". In: *Applied Physics Letters* 93.20 (Nov. 21, 2008), p. 203116. DOI: 10.1063/1.3036533 (cited on p. 1).

[3] M. Abe and Y. Tanaka. "High frequency write head measurement with the phase detection magnetic force microscope". In: *Journal of Applied Physics* 89.11 (June 1, 2001), pp. 6766–6768. DOI: 10.1063/1.1359232 (cited on pp. 1, 41).

[4] Michael R. Koblischka, Jian-Dong Wei, Michael Kirsch, and Uwe Hartmann. "High Frequency Magnetic Force Microscopy-Imaging of Harddisk Write Heads". In: *Japanese Journal of Applied Physics* 45.3 (Mar. 27, 2006), p. 2238. DOI: 10.1143/JJAP.45.2238 (cited on pp. 1, 41).

[5] P. Maletinsky, S. Hong, M. S. Grinolds, B. Hausmann, M. D. Lukin, R. L. Walsworth, M. Loncar, and A. Yacoby. "A robust scanning diamond sensor for nanoscale imaging with single nitrogen-vacancy centres". In: *Nature Nanotechnology* 7.5 (May 2012), pp. 320–324. DOI: 10.1038/nnano.2012.50 (cited on p. 2).

[6] Denis Vasyukov, Yonathan Anahory, Lior Embon, Dorri Halbertal, Jo Cuppens, Lior Neeman, Amit Finkler, Yehonathan Segev, Yuri Myasoedov, Michael L. Rappaport, Martin E. Huber, and Eli Zeldov. "A scanning superconducting quantum interference device with single electron spin sensitivity". In: *Nature Nanotechnology* 8.9 (Sept. 2013). tex.ids= vasyukov_scanning_2013-1 number: 9 publisher: Nature Publishing Group, pp. 639–644. DOI: 10.1038/nnano.2013.169 (cited on p. 2).

[7] G. Romagnoli, E. Marchiori, K. Bagani, and M. Poggio. "Fabrication of Nb and MoGe SQUID-on-tip probes by magnetron sputtering". In: *Applied Physics Letters* 122.19 (May 8, 2023), p. 192603. DOI: 10.1063/5.0150222 (cited on p. 2).

[8] M. Lange, S. Guénon, F. Lever, R. Kleiner, and D. Koelle. "A high-resolution combined scanning laser and widefield polarizing microscope for imaging at temperatures from 4

K to 300 K". In: *Review of Scientific Instruments* 88.12 (Dec. 11, 2017), p. 123705. DOI: 10.1063/1.5009529 (cited on p. 2).

[9] J. Rudge, H. Xu, J. Kolthammer, Y. K. Hong, and B. C. Choi. "Sub-nanosecond time-resolved near-field scanning magneto-optical microscope". In: *Review of Scientific Instruments* 86.2 (Feb. 11, 2015), p. 023703. DOI: 10.1063/1.4907712 (cited on p. 2).

[10] John Kerr. "XLIII. On rotation of the plane of polarization by reflection from the pole of a magnet". In: *The London, Edinburgh, and Dublin Philosophical Magazine and Journal of Science* 3.19 (May 1, 1877), pp. 321–343. DOI: 10.1080/14786447708639245 (cited on p. 2).

[11] Tao Zhou, Mathew Cherukara, and Charudatta Phatak. "Differential programming enabled functional imaging with Lorentz transmission electron microscopy". In: *npj Computational Materials* 7.1 (Sept. 6, 2021), p. 141. DOI: 10.1038/s41524-021-00600-x (cited on p. 2).

[12] Nicola Rossi, Floris R. Braakman, Davide Cadeddu, Denis Vasyukov, Gözde Tütüncüoglu, Anna Fontcuberta i Morral, and Martino Poggio. "Vectorial scanning force microscopy using a nanowire sensor". In: *Nature Nanotechnology* 12.2 (Feb. 2017), pp. 150–155. DOI: 10.1038/nnano.2016.189 (cited on pp. 2, 27, 30).

[13] J. Moser, A. Eichler, J. Güttinger, M. I. Dykman, and A. Bachtold. "Nanotube mechanical resonators with quality factors of up to 5 million". In: *Nature Nanotechnology* advance online publication (Oct. 26, 2014). DOI: 10.1038/nnano.2014.234 (cited on p. 2).

[14] Francesco Fogliano, Benjamin Besga, Antoine Reigue, Laure Mercier de Lépinay, Philip Heringlake, Clement Gouriou, Eric Eyraud, Wolfgang Wernsdorfer, Benjamin Pigeau, and Olivier Arcizet. "Ultrasensitive nano-optomechanical force sensor operated at dilution temperatures". In: *Nature Communications* 12.1 (July 5, 2021). Number: 1 Publisher: Nature Publishing Group, p. 4124. DOI: 10.1038/s41467-021-24318-y (cited on pp. 2, 16, 92).

[15] T. D. Stowe, K. Yasumura, T. W. Kenny, D. Botkin, K. Wago, and D. Rugar. "Attonewton force detection using ultrathin silicon cantilevers". In: *Applied Physics Letters* 71.2 (July 14, 1997), pp. 288–290. DOI: 10.1063/1.119522 (cited on pp. 2, 16, 91).

[16] Alexina Ollier, Marcin Kisiel, Xiaobo Lu, Urs Gysin, Martino Poggio, Dmitri K. Efetov, and Ernst Meyer. "Energy dissipation on magic angle twisted bilayer graphene". In: *Communications Physics* 6.1 (Nov. 28, 2023). Number: 1 Publisher: Nature Publishing Group, pp. 1–9. DOI: 10.1038/s42005-023-01441-4 (cited on p. 2).

[17] Anil Kumar Chopra. *Dynamics of Structures*. 4th ed. Boston Columbus Indianapolis New York San Francisco: Pearson Higher Education, 2014 (cited on pp. 2, 23, 27).

[18] Laure Mercier de Lépinay, Benjamin Pigeau, Benjamin Besga, Pascal Vincent, Philippe Poncharal, and Olivier Arcizet. "A universal and ultrasensitive vectorial nanomechanical sensor for imaging 2D force fields". In: *Nature Nanotechnology* 12.2 (Feb. 2017), pp. 156–162. DOI: 10.1038/nnano.2016.193 (cited on pp. 2, 27).

[19] Nicola Rossi. "Force sensing with nanowires". Thesis. Basel, Switzerland: University of Basel, 2019. 136 Seiten. DOI: 10.5451/unibas-007178292 (cited on p. 2).

[20] Hinrich Mattiat. "Nanowire Magnetic Force Microscopy". PhD thesis. Basel, Switzerland: University of Basel, June 20, 2023. 142 pp. (cited on pp. 2, 35, 60).

[21] H. Mattiat, N. Rossi, B. Gross, J. Pablo-Navarro, C. Magén, R. Badea, J. Berezovsky, J. M. De Teresa, and M. Poggio. "Nanowire Magnetic Force Sensors Fabricated by Focused-Electron-Beam-Induced Deposition". In: *Physical Review Applied* 13.4 (Apr. 16, 2020), p. 044043. DOI: 10.1103/PhysRevApplied.13.044043 (cited on pp. 2, 16, 59, 60, 68, 69).

[22] Robert M. White. *Quantum Theory of Magnetism: Magnetic Properties of Materials*. Red. by Manuel Cardona, Peter Fulde, Klaus Von Klitzing, Roberto Merlin, Hans-Joachim Queisser, and Horst Störmer. Vol. 32. Springer Series in SOLID-STATE SCIENCES. Berlin, Heidelberg: Springer, 2007. DOI: 10.1007/978-3-540-69025-2 (cited on pp. 4, 5, 8).

[23] Norberto Majlis. *The Quantum Theory of Magnetism*. World Scientific, 2007. 392 pp. (cited on pp. 5, 6).

[24] M. J. Dunlavy and D. Venus. "Critical slowing down in the two-dimensional Ising model measured using ferromagnetic ultrathin films". In: *Physical Review B* 71.14 (Apr. 12, 2005), p. 144406. DOI: 10.1103/PhysRevB.71.144406 (cited on p. 8).

[25] Changmin Lee, Praveen Vir, Kaustuv Manna, Chandra Shekhar, J. E. Moore, M. A. Kastner, Claudia Felser, and Joseph Orenstein. "Observation of a phase transition within the domain walls of ferromagnetic Co3Sn2S2". In: *Nature Communications* 13 (May 30, 2022), p. 3000. DOI: 10.1038/s41467-022-30460-y (cited on pp. 9, 81).

[26] Mikko Kataja and Sebastiaan Van Dijken. "Magneto-optical Kerr effect susceptometer for the analysis of magnetic domain wall dynamics". In: *Review of Scientific Instruments* 82.10 (Oct. 1, 2011), p. 103901. DOI: 10.1063/1.3647313 (cited on p. 9).

[27] O. A. Tretiakov, D. Clarke, Gia-Wei Chern, Ya. B. Bazaliy, and O. Tchernyshyov. "Dynamics of Domain Walls in Magnetic Nanostrips". In: *Physical Review Letters* 100.12 (Mar. 28, 2008), p. 127204. DOI: 10.1103/PhysRevLett.100.127204 (cited on p. 9).

[28] Xin-Yue Zhang, Yu-Xuan Wang, Thomas A. Tartaglia, Thomas Ding, Mason J. Gray, Kenneth S. Burch, Fazel Tafti, and Brian B. Zhou. "ac Susceptometry of 2D van der Waals Magnets Enabled by the Coherent Control of Quantum Sensors". In: *PRX Quantum* 2.3 (Sept. 28, 2021), p. 030352. DOI: 10.1103/PRXQuantum.2.030352 (cited on pp. 9, 81).

[29] Michael J. Dunlavy. “Static and Dynamic Critical Phenomena in Ultrathin Films of Iron on W(110)”. thesis. 2003 (cited on p. 9).

[30] Yu Wang, Jie Wang, Takayuki Kitamura, Hiroyuki Hirakata, and Takahiro Shimada. “Effective modeling of magnitude-fluctuated magnetization dynamics: Dynamic precursor effect in magnets”. In: *Physical Review B* 106.9 (Sept. 20, 2022), p. 094423. DOI: 10.1103/PhysRevB.106.094423 (cited on p. 9).

[31] K. Binder. “Time-Dependent Ginzburg-Landau Theory of Nonequilibrium Relaxation”. In: *Physical Review B* 8.7 (Oct. 1, 1973), pp. 3423–3438. DOI: 10.1103/PhysRevB.8.3423 (cited on p. 9).

[32] Ernst Meyer, Roland Bennewitz, and Hans J. Hug. *Scanning Probe Microscopy: The Lab on a Tip*. Graduate Texts in Physics. Cham: Springer International Publishing, 2021. DOI: 10.1007/978-3-030-37089-3 (cited on pp. 11, 35, 59).

[33] C. Schönenberger and S. F. Alvarado. “Understanding magnetic force microscopy”. In: *Zeitschrift für Physik B Condensed Matter* 80.3 (Oct. 1, 1990), pp. 373–383. DOI: 10.1007/BF01323519 (cited on p. 12).

[34] Neil E. Jenkins. “Expanding the Limits of Magnetic Resonance Force Microscopy”. PhD thesis. Cornell University, 2007. 241 pp. (cited on p. 16).

[35] Andrew N Cleland. *Foundations of Nanomechanics From Solid-State Theory to Device Applications*. Berlin, Heidelberg: Springer Berlin Heidelberg, 2003 (cited on p. 17).

[36] Clive L. Dym and Irving H. Shames. “Dynamics of Beams and Plates”. In: *Solid Mechanics: A Variational Approach, Augmented Edition*. Ed. by Clive L. Dym and Irving H. Shames. New York, NY: Springer, 2013, pp. 373–447. DOI: 10.1007/978-1-4614-6034-3_7 (cited on p. 19).

[37] Silvan Schmid, Luis Guillermo Villanueva, and Michael Lee Roukes. *Fundamentals of Nanomechanical Resonators*. Springer International Publishing, 2016 (cited on p. 23).

[38] Laure Mercier de Lépinay, Benjamin Pigeau, Benjamin Besga, and Olivier Arcizet. “Eigenmode orthogonality breaking and deviation from the fluctuation dissipation relation in rotationally dressed nanomechanical oscillators”. In: *arXiv:1612.03956 [cond-mat]* (Dec. 12, 2016) (cited on p. 30).

[39] William Fuller Brown. *Magnetostatic principles in ferromagnetism*. Interscience Publishers, 1962. 202 pp. (cited on p. 33).

[40] D. Rugar, H. J. Mamin, P. Guethner, S. E. Lambert, J. E. Stern, I. McFadyen, and T. Yogi. “Magnetic force microscopy: General principles and application to longitudinal recording media”. In: *Journal of Applied Physics* 68.3 (Aug. 1, 1990), pp. 1169–1183. DOI: 10.1063/1.346713 (cited on p. 33).

[41] A. Hubert, W. Rave, and S. L. Tomlinson. "Imaging Magnetic Charges with Magnetic Force Microscopy". In: *physica status solidi (b)* 204.2 (Dec. 1, 1997), pp. 817–828. DOI: 10.1002/1521-3951(199712)204:2<817::AID-PSSB817>3.0.CO;2-D (cited on p. 33).

[42] Alex Hubert and Rudolf Schäfer. *Magnetic domains: the analysis of magnetic microstructures*. Berlin ; New York: Springer, 1998. 696 pp. (cited on p. 33).

[43] Hans J. Hug, B. Stiefel, P. J. A. van Schendel, A. Moser, R. Hofer, S. Martin, H.-J. Güntherodt, Steffen Porthun, Leon Abelmann, J. C. Lodder, Gabriel Bochi, and R. C. O'Handley. "Quantitative magnetic force microscopy on perpendicularly magnetized samples". In: *Journal of Applied Physics* 83.11 (June 1, 1998), pp. 5609–5620. DOI: 10.1063/1.367412 (cited on p. 34).

[44] Y. Feng, A.-O. Mandru, O. Yıldırım, and H.J. Hug. "Quantitative Magnetic Force Microscopy: Transfer-Function Method Revisited". In: *Physical Review Applied* 18.2 (Aug. 5, 2022), p. 024016. DOI: 10.1103/PhysRevApplied.18.024016 (cited on p. 34).

[45] T. Göddenhenrich, H. Lemke, M. Mück, U. Hartmann, and C. Heiden. "Probe calibration in magnetic force microscopy". In: *Applied Physics Letters* 57.24 (Dec. 10, 1990), pp. 2612–2614. DOI: 10.1063/1.103827 (cited on pp. 39, 62).

[46] Alexey V. Nazarov, Martin L. Plumer, and Bharat B. Pant. "High-frequency magnetic-force microscopy characterization of magnetic recording writer poles". In: *Journal of Applied Physics* 97.10 (May 17, 2005), 10N902. DOI: 10.1063/1.1852436 (cited on p. 41).

[47] M. R. Koblischka, J. D. Wei, T. Sulzbach, and U. Hartmann. "High-frequency MFM characterization of magnetic recording writer poles". In: *Applied Physics A* 94.2 (Feb. 1, 2009), pp. 235–240. DOI: 10.1007/s00339-008-4805-7 (cited on p. 41).

[48] Marina V. Makarova, Kaichi Suzuki, Hirofumi Kon, Paritosh Dubey, Hiroshi Sonobe, Toru Matsumura, and Hitoshi Saito. "High-Frequency Magnetic Field Energy Imaging of Magnetic Recording Head by Alternating Magnetic Force Microscopy (A-MFM) with Superparamagnetic Tip". In: *Applied Sciences* 13.8 (Jan. 2023), p. 4843. DOI: 10.3390/app13084843 (cited on p. 41).

[49] Casey Israel, Weida Wu, and Alex De Lozanne. "High-field magnetic force microscopy as susceptibility imaging". In: *Applied Physics Letters* 89.3 (July 17, 2006), p. 032502. DOI: 10.1063/1.2221916 (cited on p. 41).

[50] Mariia Stepanova, Jan Masell, Erik Lysne, Peggy Schoenherr, Laura Köhler, Michael Paulsen, Alireza Qaiumzadeh, Naoya Kanazawa, Achim Rosch, Yoshinori Tokura, Arne Brataas, Markus Garst, and Dennis Meier. "Detection of Topological Spin Textures via Nonlinear Magnetic Responses". In: *Nano Letters* 22.1 (Jan. 12, 2022), pp. 14–21. DOI: 10.1021/acs.nanolett.1c02723 (cited on pp. 41, 44, 88, 92).

[51] D.A. Broadway, S.E. Lillie, S.C. Scholten, D. Rohner, N. Dontschuk, P. Maletinsky, J.-P. Tetienne, and L.C.L. Hollenberg. "Improved Current Density and Magnetization Reconstruction Through Vector Magnetic Field Measurements". In: *Physical Review Applied* 14.2 (Aug. 26, 2020), p. 024076. DOI: 10.1103/PhysRevApplied.14.024076 (cited on p. 43).

[52] Y. Dovzhenko, F. Casola, S. Schlotter, T. X. Zhou, F. Büttner, R. L. Walsworth, G. S. D. Beach, and A. Yacoby. "Magnetostatic twists in room-temperature skyrmions explored by nitrogen-vacancy center spin texture reconstruction". In: *Nature Communications* 9.1 (July 13, 2018). tex.ids= dovzhenko_magnetostatic_2018-1 number: 1 publisher: Nature Publishing Group, p. 2712. DOI: 10.1038/s41467-018-05158-9 (cited on p. 43).

[53] T. R. Albrecht, P. Grütter, D. Horne, and D. Rugar. "Frequency modulation detection using high-Q cantilevers for enhanced force microscope sensitivity". In: *Journal of Applied Physics* 69.2 (Jan. 15, 1991), pp. 668–673. DOI: 10.1063/1.347347 (cited on p. 45).

[54] John M. Nichol, Eric R. Hemesath, Lincoln J. Lauhon, and Raffi Budakian. "Displacement detection of silicon nanowires by polarization-enhanced fiber-optic interferometry". In: *Applied Physics Letters* 93.19 (Nov. 10, 2008), p. 193110. DOI: 10.1063/1.3025305 (cited on pp. 50, 52).

[55] Aleksander Labuda, Yoichi Miyahara, Lynda Cockins, and Peter H. Grütter. "Decoupling conservative and dissipative forces in frequency modulation atomic force microscopy". In: *Physical Review B* 84.12 (Sept. 15, 2011), p. 125433. DOI: 10.1103/PhysRevB.84.125433 (cited on p. 56).

[56] A. Labuda, K. Kobayashi, D. Kiracofe, K. Suzuki, P. H. Grütter, and H. Yamada. "Comparison of photothermal and piezoacoustic excitation methods for frequency and phase modulation atomic force microscopy in liquid environments". In: *AIP Advances* 1.2 (June 2011), p. 022136. DOI: 10.1063/1.3601872 (cited on p. 56).

[57] Pardis Sahafi, William Rose, Andrew Jordan, Ben Yager, Michèle Piscitelli, and Raffi Budakian. "Ultralow Dissipation Patterned Silicon Nanowire Arrays for Scanning Probe Microscopy". In: *Nano Letters* 20.1 (Jan. 8, 2020), pp. 218–223. DOI: 10.1021/acs.nanolett.9b03668 (cited on pp. 58, 91).

[58] Jinjin Zhang, Daniel M. Czajkowsky, Yi Shen, Jielin Sun, Chunhai Fan, Jun Hu, and Zhifeng Shao. "Bias controlled capacitive driven cantilever oscillation for high resolution dynamic force microscopy". In: *Applied Physics Letters* 102.7 (Feb. 18, 2013), p. 073110. DOI: 10.1063/1.4793205 (cited on p. 59).

[59] Miriam Jaafar, Oscar Iglesias-Freire, Luis Serrano-Ramón, Manuel Ricardo Ibarra, Jose Maria de Teresa, and Agustina Asenjo. "Distinguishing magnetic and electrostatic interactions by a Kelvin probe force microscopy–magnetic force microscopy combination". In:

Beilstein Journal of Nanotechnology 2.1 (Sept. 7, 2011), pp. 552–560. DOI: 10.3762/bjnano.2.59 (cited on p. 59).

[60] Andreas Rudolph, Marcello Soda, Matthias Kiessling, Tomasz Wojtowicz, Dieter Schuh, Werner Wegscheider, Josef Zweck, Christian Back, and Elisabeth Reiger. "Ferromagnetic GaAs/GaMnAs Core-Shell Nanowires Grown by Molecular Beam Epitaxy". In: *Nano Letters* 9.11 (Nov. 11, 2009), pp. 3860–3866. DOI: 10.1021/nl9020717 (cited on p. 59).

[61] N. Rossi, B. Gross, F. Dirnberger, D. Bougeard, and M. Poggio. "Magnetic Force Sensing Using a Self-Assembled Nanowire". In: *Nano Letters* 19.2 (Feb. 13, 2019), pp. 930–936. DOI: 10.1021/acs.nanolett.8b04174 (cited on pp. 59, 62, 69).

[62] Javier Pablo-Navarro, Dédalo Sanz-Hernández, César Magén, Amalio Fernández-Pacheco, and José María de Teresa. "Tuning shape, composition and magnetization of 3D cobalt nanowires grown by focused electron beam induced deposition (FEBID)". In: *Journal of Physics D: Applied Physics* 50.18 (2017). tex.ids: pablo-navarro_tuning_2017-1 publisher: IOP Publishing, 18LT01. DOI: 10.1088/1361-6463/aa63b4 (cited on p. 61).

[63] Ivo Utke, Patrik Hoffmann, and John Melngailis. "Gas-assisted focused electron beam and ion beam processing and fabrication". In: *Journal of Vacuum Science & Technology B: Microelectronics and Nanometer Structures Processing, Measurement, and Phenomena* 26.4 (July 1, 2008), pp. 1197–1276. DOI: 10.1116/1.2955728 (cited on p. 61).

[64] Amalio Fernández-Pacheco, Luis Serrano-Ramón, Jan M. Michalik, M. Ricardo Ibarra, José M. De Teresa, Liam O'Brien, Dorothée Petit, Jihyun Lee, and Russell P. Cowburn. "Three dimensional magnetic nanowires grown by focused electron-beam induced deposition". In: *Scientific Reports* 3 (Mar. 20, 2013), srep01492. DOI: 10.1038/srep01492 (cited on p. 61).

[65] Liza Žaper, Peter Rickhaus, Marcus Wyss, Boris Gross, Kai Wagner, Martino Poggio, and Floris Braakman. "Scanning Nitrogen-Vacancy Magnetometry of Focused-Electron-Beam-Deposited Cobalt Nanomagnets". In: *ACS Applied Nano Materials* 7.4 (Feb. 23, 2024), pp. 3854–3860. DOI: 10.1021/acsanm.3c05470 (cited on p. 61).

[66] Michael Huth, Fabrizio Porrati, and Sven Barth. "Living up to its potential—Direct-write nanofabrication with focused electron beams". In: *Journal of Applied Physics* 130.17 (Nov. 1, 2021), p. 170901. DOI: 10.1063/5.0064764 (cited on p. 61).

[67] Dédalo Sanz-Hernández, Aurelio Hierro-Rodriguez, Claire Donnelly, Javier Pablo-Navarro, Andrea Sorrentino, Eva Pereiro, César Magén, Stephen McVitie, José María de Teresa, Salvador Ferrer, Peter Fischer, and Amalio Fernández-Pacheco. "Artificial Double-Helix for Geometrical Control of Magnetic Chirality". In: *ACS Nano* 14.7 (July 28, 2020), pp. 8084–8092. DOI: 10.1021/acsnano.0c00720 (cited on p. 61).

[68] B. Gross, D. P. Weber, D. Rüffer, A. Buchter, F. Heimbach, A. Fontcuberta i Morral, D. Grundler, and M. Poggio. "Dynamic cantilever magnetometry of individual CoFeB nanotubes". In: *Physical Review B* 93.6 (Feb. 5, 2016), p. 064409. DOI: 10.1103/PhysRevB.93.064409 (cited on pp. 62, 63).

[69] J. M. De Teresa and A. Fernández-Pacheco. "Present and future applications of magnetic nanostructures grown by FEBID". In: *Applied Physics A* 117.4 (Dec. 2014), pp. 1645–1658. DOI: 10.1007/s00339-014-8617-7 (cited on p. 64).

[70] T. Adams, A. Chacon, M. Wagner, A. Bauer, G. Brandl, B. Pedersen, H. Berger, P. Lemmens, and C. Pfleiderer. "Long-Wavelength Helimagnetic Order and Skyrmion Lattice Phase in Cu_2OSeO_3". In: *Physical Review Letters* 108.23 (June 8, 2012), p. 237204. DOI: 10.1103/PhysRevLett.108.237204 (cited on pp. 69, 71).

[71] S. Mühlbauer, B. Binz, F. Jonietz, C. Pfleiderer, A. Rosch, A. Neubauer, R. Georgii, and P. Böni. "Skyrmion Lattice in a Chiral Magnet". In: *Science* 323.5916 (Feb. 13, 2009). tex.ids= muhlbauer_skyrmion_2009-1 publisher: American Association for the Advancement of Science, pp. 915–919. DOI: 10.1126/science.1166767 (cited on p. 69).

[72] J. C. Loudon, A. O. Leonov, A. N. Bogdanov, M. Ciomaga Hatnean, and G. Balakrishnan. "Direct observation of attractive skyrmions and skyrmion clusters in the cubic helimagnet Cu_2OSeO_3". In: *Physical Review B* 97.13 (Apr. 5, 2018), p. 134403. DOI: 10.1103/PhysRevB.97.134403 (cited on p. 69).

[73] S. Seki, X. Z. Yu, S. Ishiwata, and Y. Tokura. "Observation of Skyrmions in a Multiferroic Material". In: *Science* 336.6078 (Apr. 13, 2012), pp. 198–201. DOI: 10.1126/science.1214143 (cited on p. 69).

[74] S. Seki, J.-H. Kim, D. S. Inosov, R. Georgii, B. Keimer, S. Ishiwata, and Y. Tokura. "Formation and rotation of skyrmion crystal in the chiral-lattice insulator Cu2OSeO3". In: *Physical Review B* 85.22 (June 22, 2012). DOI: 10.1103/PhysRevB.85.220406 (cited on p. 70).

[75] J. S. White, I. Živković, A. J. Kruchkov, M. Bartkowiak, A. Magrez, and H. M. Rønnow. "Electric-Field-Driven Topological Phase Switching and Skyrmion-Lattice Metastability in Magnetoelectric Cu_2OSeO_3". In: *Physical Review Applied* 10.1 (July 23, 2018), p. 014021. DOI: 10.1103/PhysRevApplied.10.014021 (cited on p. 70).

[76] J.S. White, K. Prša, P. Huang, A.A. Omrani, I. Živković, M. Bartkowiak, H. Berger, A. Magrez, J.L. Gavilano, G. Nagy, J. Zang, and H.M. Rønnow. "Electric-Field-Induced Skyrmion Distortion and Giant Lattice Rotation in the Magnetoelectric Insulator Cu_2OSeO_3". In: *Physical Review Letters* 113.10 (Sept. 4, 2014), p. 107203. DOI: 10.1103/PhysRevLett.113.107203 (cited on p. 70).

[77] Y. Okamura, F. Kagawa, S. Seki, and Y. Tokura. "Transition to and from the skyrmion lattice phase by electric fields in a magnetoelectric compound". In: *Nature Communications* 7.1 (Sept. 1, 2016), p. 12669. DOI: 10.1038/ncomms12669 (cited on p. 70).

[78] Estefani Marchiori, Giulio Romagnoli, Lukas Schneider, Boris Gross, Pardis Sahafi, Andrew Jordan, Raffi Budakian, Priya R. Baral, Arnaud Magrez, Jonathan S. White, and Martino Poggio. "Imaging magnetic spiral phases, skyrmion clusters, and skyrmion displacements at the surface of bulk Cu_2OSeO_3". In: *Communications Materials* 5.1 (Sept. 28, 2024), p. 202. DOI: 10.1038/s43246-024-00647-5 (cited on pp. 70, 74, 93, 104, 105).

[79] A. Chacon, L. Heinen, M. Halder, A. Bauer, W. Simeth, S. Mühlbauer, H. Berger, M. Garst, A. Rosch, and C. Pfleiderer. "Observation of two independent skyrmion phases in a chiral magnetic material". In: *Nature Physics* 14.9 (Sept. 2018), pp. 936–941. DOI: 10.1038/s41567-018-0184-y (cited on p. 70).

[80] Andrey O. Leonov and Catherine Pappas. "Reorientation processes of tilted skyrmion and spiral states in a bulk cubic helimagnet Cu_2OSeO_3". In: *Frontiers in Physics* 11 (2023). DOI: 10.3389/fphy.2023.1105784 (cited on p. 74).

[81] Filipp N. Rybakov, Aleksandr B. Borisov, Stefan Blügel, and Nikolai S. Kiselev. "New spiral state and skyrmion lattice in 3D model of chiral magnets". In: *New Journal of Physics* 18.4 (2016), p. 045002. DOI: 10.1088/1367-2630/18/4/045002 (cited on p. 74).

[82] S. A. Osorio, V. Laliena, J. Campo, and S. Bustingorry. "Chiral helimagnetism and stability of magnetic textures in $MnNb_3S_6$". In: *Physical Review B* 108.5 (Aug. 9, 2023), p. 054414. DOI: 10.1103/PhysRevB.108.054414 (cited on p. 74).

[83] Chen Ye, Cong Wang, Qiong Wu, Sheng Liu, Jiayuan Zhou, Guopeng Wang, Aljoscha Söll, Zdenek Sofer, Ming Yue, Xue Liu, Mingliang Tian, Qihua Xiong, Wei Ji, and Xiao Renshaw Wang. "Layer-Dependent Interlayer Antiferromagnetic Spin Reorientation in Air-Stable Semiconductor CrSBr". In: *ACS Nano* 16.8 (Aug. 23, 2022), pp. 11876–11883. DOI: 10.1021/acsnano.2c01151 (cited on p. 75).

[84] Bingyu Zhang, Pengcheng Lu, Roozbeh Tabrizian, Philip X.-L. Feng, and Yingying Wu. "2D Magnetic heterostructures: spintronics and quantum future". In: *npj Spintronics* 2.1 (May 30, 2024), pp. 1–10. DOI: 10.1038/s44306-024-00011-w (cited on p. 75).

[85] V. Carteaux, D. Brunet, G. Ouvrard, and G. Andre. "Crystallographic, magnetic and electronic structures of a new layered ferromagnetic compound Cr2Ge2Te6". In: *Journal of Physics: Condensed Matter* 7.1 (Jan. 1995), pp. 69–87. DOI: 10.1088/0953-8984/7/1/008 (cited on p. 75).

[86] Xiao Zhang, Yuelei Zhao, Qi Song, Shuang Jia, Jing Shi, and Wei Han. "Magnetic anisotropy of the single-crystalline ferromagnetic insulator Cr2Ge2Te6". In: *Japanese Journal of Applied Physics* 55.3 (Feb. 1, 2016), p. 033001. DOI: 10.7567/JJAP.55.033001 (cited on p. 75).

[87] J. Zeisner. "Magnetic anisotropy and spin-polarized two-dimensional electron gas in the van der Waals ferromagnet Cr2Ge2Te6". In: *Physical Review B* 99.16 (2019). DOI: 10.1103/PhysRevB.99.165109 (cited on pp. 75, 82).

[88] Yu Liu. "Critical behavior of quasi-two-dimensional semiconducting ferromagnet Cr2Ge2Te6". In: *Physical Review B* 96.5 (2017). DOI: 10.1103/PhysRevB.96.054406 (cited on pp. 75, 82).

[89] Huiwen Ji, R. A. Stokes, L. D. Alegria, E. C. Blomberg, M. A. Tanatar, Anjan Reijnders, L. M. Schoop, Tian Liang, R. Prozorov, K. S. Burch, N. P. Ong, J. R. Petta, and R. J. Cava. "A ferromagnetic insulating substrate for the epitaxial growth of topological insulators". In: *Journal of Applied Physics* 114.11 (Sept. 21, 2013), p. 114907. DOI: 10.1063/1.4822092 (cited on pp. 75, 82).

[90] Cheng Gong, Lin Li, Zhenglu Li, Huiwen Ji, Alex Stern, Yang Xia, Ting Cao, Wei Bao, Chenzhe Wang, Yuan Wang, Z. Q. Qiu, R. J. Cava, Steven G. Louie, Jing Xia, and Xiang Zhang. "Discovery of intrinsic ferromagnetism in two-dimensional van der Waals crystals". In: *Nature* 546.7657 (June 2017), pp. 265–269. DOI: 10.1038/nature22060 (cited on pp. 75, 76, 82).

[91] Wei He, Lingling Kong, Weina Zhao, and Peng Yu. "Atomically Thin 2D van der Waals Magnetic Materials: Fabrications, Structure, Magnetic Properties and Applications". In: *Coatings* 12.2 (Jan. 21, 2022), p. 122. DOI: 10.3390/coatings12020122 (cited on p. 76).

[92] Andriani Vervelaki, Kousik Bagani, Daniel Jetter, Manh-Ha Doan, Tuan K. Chau, Boris Gross, Dennis V. Christensen, Peter Bøggild, and Martino Poggio. "Visualizing thickness-dependent magnetic textures in few-layer $Cr_2Ge_2Te_6$". In: *Communications Materials* 5.1 (Mar. 19, 2024), p. 40. DOI: 10.1038/s43246-024-00477-5 (cited on pp. 76–81).

[93] Joachim Dahl Thomsen, Myung-Geun Han, Aubrey N. Penn, Alexandre C. Foucher, Michael Geiwitz, Kenneth Stephen Burch, Lukas Dekanovsky, Zdeněk Sofer, Yu Liu, Cedomir Petrovic, Frances M. Ross, Yimei Zhu, and Prineha Narang. "Effect of Surface Oxidation and Crystal Thickness on the Magnetic Properties and Magnetic Domain Structures of Cr2Ge2Te6". In: *ACS Nano* 18.21 (May 28, 2024), pp. 13458–13467. DOI: 10.1021/acsnano.3c09858 (cited on p. 76).

[94] Myung-Geun Han, Joseph A. Garlow, Yu Liu, Huiqin Zhang, Jun Li, Donald DiMarzio, Mark W. Knight, Cedomir Petrovic, Deep Jariwala, and Yimei Zhu. "Topological Magnetic-Spin Textures in Two-Dimensional van der Waals Cr2Ge2Te6". In: *Nano Letters* 19.11 (Nov. 13, 2019), pp. 7859–7865. DOI: 10.1021/acs.nanolett.9b02849 (cited on p. 76).

[95] Joseph Alec Wilcox, Lukas Schneider, Estefani Marchiori, Vadim Plastovets, Alexandre Buzdin, Pardis Sahafi, Andrew Jordan, Raffi Budakian, Tong Ren, Ivan Veshchunov, Tsuyoshi Tamegai, Sven Friedemann, Martino Poggio, and Simon John Bending. "Magnetically controlled vortex dynamics in a ferromagnetic superconductor". In: *Communica-*

tions Materials 6.1 (May 31, 2025), pp. 1–11. DOI: 10.1038/s43246-025-00833-z (cited on pp. 77, 106–108).

[96] M. Bałanda. "AC Susceptibility Studies of Phase Transitions and Magnetic Relaxation: Conventional, Molecular and Low-Dimensional Magnets". In: *Acta Physica Polonica A* 124.6 (Dec. 2013), pp. 964–976. DOI: 10.12693/APhysPolA.124.964 (cited on p. 81).

[97] T. Sakurai, B. Rubrecht, L. T. Corredor, R. Takehara, M. Yasutani, J. Zeisner, A. Alfonsov, S. Selter, S. Aswartham, A. U. B. Wolter, B. Büchner, H. Ohta, and V. Kataev. "Pressure control of the magnetic anisotropy of the quasi-two-dimensional van der Waals ferromagnet Cr2Ge2Te6". In: *Physical Review B* 103.2 (Jan. 5, 2021), p. 024404. DOI: 10.1103/PhysRevB.103.024404 (cited on p. 82).

[98] Amilcar Bedoya-Pinto, Jing-Rong Ji, Avanindra K. Pandeya, Pierluigi Gargiani, Manuel Valvidares, Paolo Sessi, James M. Taylor, Florin Radu, Kai Chang, and Stuart S. P. Parkin. "Intrinsic 2D-XY ferromagnetism in a van der Waals monolayer". In: *Science* 374.6567 (Oct. 29, 2021), pp. 616–620. DOI: 10.1126/science.abd5146 (cited on p. 83).

[99] Evan J. Telford, Avalon H. Dismukes, Raymond L. Dudley, Ren A. Wiscons, Kihong Lee, Daniel G. Chica, Michael E. Ziebel, Myung-Geun Han, Jessica Yu, Sara Shabani, Allen Scheie, Kenji Watanabe, Takashi Taniguchi, Di Xiao, Yimei Zhu, Abhay N. Pasupathy, Colin Nuckolls, Xiaoyang Zhu, Cory R. Dean, and Xavier Roy. "Coupling between magnetic order and charge transport in a two-dimensional magnetic semiconductor". In: *Nature Materials* 21.7 (July 2022), pp. 754–760. DOI: 10.1038/s41563-022-01245-x (cited on p. 83).

[100] Andrey M. Tokmachev, Dmitry V. Averyanov, Alexander N. Taldenkov, Oleg E. Parfenov, Igor A. Karateev, Ivan S. Sokolov, and Vyacheslav G. Storchak. "Lanthanide f7 metalloxenes – a class of intrinsic 2D ferromagnets". In: *Materials Horizons* 6.7 (Aug. 12, 2019), pp. 1488–1496. DOI: 10.1039/C9MH00444K (cited on pp. 83, 84).

[101] J. M. Cadogan, D. H. Ryan, Rasa Rejali, and C. D. Boyer. "The magnetic structure of EuGe2". In: *Journal of Alloys and Compounds* 688 (Dec. 15, 2016), pp. 51–54. DOI: 10.1016/j.jallcom.2016.06.268 (cited on p. 83).

[102] O. Kazakova, R. Puttock, C. Barton, H. Corte-León, M. Jaafar, V. Neu, and A. Asenjo. "Frontiers of magnetic force microscopy". In: *Journal of Applied Physics* 125.6 (Feb. 14, 2019), p. 060901. DOI: 10.1063/1.5050712 (cited on p. 84).

[103] Hinrich Mattiat, Lukas Schneider, Patrick Reiser, Martino Poggio, Pardis Sahafi, Andrew Jordan, Raffi Budakian, Dmitry V. Averyanov, Ivan S. Sokolov, Alexander N. Taldenkov, Oleg E. Parfenov, Oleg A. Kondratev, Andrey M. Tokmachev, and Vyacheslav G. Storchak. "Mapping the phase-separated state in a 2D magnet". In: *Nanoscale* 16.10 (Mar. 7, 2024), pp. 5302–5312. DOI: 10.1039/D3NR06550B (cited on pp. 88, 89, 92, 93).

[104] Dmitry V. Averyanov, Ivan S. Sokolov, Alexander N. Taldenkov, Oleg E. Parfenov, Igor A. Karateev, Oleg A. Kondratev, Andrey M. Tokmachev, and Vyacheslav G. Storchak. "Intrinsic exchange bias state in silicene and germanene materials EuX2". In: *Nanoscale Horizons* (Mar. 23, 2023). DOI: 10.1039/D3NH00009E (cited on p. 89).

[105] Balram Singh, Rachappa Ravishankar, Jorge A. Otálora, Ivan Soldatov, Rudolf Schäfer, Daniil Karnaushenko, Volker Neu, and Oliver G. Schmidt. "Direct imaging of nanoscale field-driven domain wall oscillations in Landau structures". In: *Nanoscale* 14.37 (2022), pp. 13667–13678. DOI: 10.1039/D2NR03351H (cited on p. 91).

[106] J. R. Montague, K. A. Bertness, N. A. Sanford, V. M. Bright, and C. T. Rogers. "Temperature-dependent mechanical-resonance frequencies and damping in ensembles of gallium nitride nanowires". In: *Applied Physics Letters* 101.17 (Oct. 22, 2012), p. 173101. DOI: 10.1063/1.4761946 (cited on p. 92).

[107] Ryogo Kubo. "Statistical-Mechanical Theory of Irreversible Processes. I. General Theory and Simple Applications to Magnetic and Conduction Problems". In: *Journal of the Physical Society of Japan* 12.6 (June 15, 1957), pp. 570–586. DOI: 10.1143/JPSJ.12.570 (cited on p. 95).

[108] H. G. Dieter Forster. "Hydrodynamic Fluctuations, Broken Symmetry, and Correlation Functions". In: *Berichte der Bunsengesellschaft für physikalische Chemie* 80.9 (1976), pp. 931–931. DOI: 10.1002/bbpc.19760800922 (cited on p. 95).

[109] André-Marie Tremblay. *PHY-892 Quantum Material's Theory, from perturbation theory to dynamical-mean . . . eld theory (lecture notes).* 2024 (cited on p. 95).

[110] A. A. Clerk, M. H. Devoret, S. M. Girvin, Florian Marquardt, and R. J. Schoelkopf. "Introduction to quantum noise, measurement, and amplification". In: *Reviews of Modern Physics* 82.2 (Apr. 15, 2010), pp. 1155–1208. DOI: 10.1103/RevModPhys.82.1155 (cited on p. 99).

[111] M. Belesi, I. Rousochatzakis, M. Abid, U. K. Rößler, H. Berger, and J.-Ph. Ansermet. "Magnetoelectric effects in single crystals of the cubic ferrimagnetic helimagnet Cu2OSeO3". In: *Physical Review B* 85.22 (June 13, 2012), p. 224413. DOI: 10.1103/PhysRevB.85.224413 (cited on p. 111).